

2016

Advances in Design Procedures and Detailing of Structural Systems

Christina Cercone
Lehigh University

Follow this and additional works at: <http://preserve.lehigh.edu/etd>

 Part of the [Civil and Environmental Engineering Commons](#)

Recommended Citation

Cercone, Christina, "Advances in Design Procedures and Detailing of Structural Systems" (2016). *Theses and Dissertations*. 2543.
<http://preserve.lehigh.edu/etd/2543>

This Dissertation is brought to you for free and open access by Lehigh Preserve. It has been accepted for inclusion in Theses and Dissertations by an authorized administrator of Lehigh Preserve. For more information, please contact preserve@lehigh.edu.

Advances in Design Procedures and Detailing of Structural Systems

by

Christina Cercone

Presented to the Graduate and Research Committee
of Lehigh University
in Candidacy for the Degree of
Doctor of Philosophy

in

Structural Engineering

Lehigh University

May 2016

Copyright 2016
Christina Cercone

CERTIFICATE OF APPROVAL

Approved and recommended for acceptance as a dissertation in partial fulfillment of the requirements for the degree of Doctor of Philosophy.

Date

Clay Naito, Dissertation Director

Accepted Date

Committee Members:

Shamim Pakzad, Committee Chair

Richard Sause, Committee Member

Spencer Quiel, Committee Member

Thomas Schumacher, External Member

ACKNOWLEDGEMENTS

The author would like to thank her dissertation advisor, Professor Clay Naito, for his guidance, support and patience in her research, academic and professional endeavors over the past five years. The author would also like to thank all the members of her committee: Professor Shamim Pakzad, Professor Richard Sause, Professor Spencer Quiel, and Professor Thomas Schumacher for all of their time, guidance and feedback throughout her doctoral studies.

The author would like to thank the professors, research scientists and industry professionals whom she worked collaboratively with on the research presented in this dissertation particularly: Dr. Ronald Riggs, Dr. Yong Wei, Dr. Richard Sause and John Corven. The author is very grateful for the expertise, advice and input provided to her during her throughout the research projects.

The author would like to thank all the lab technicians and departmental staff for assisting in her experimental testing as well as the friendships they have provided throughout her time here at Lehigh especially: Darrick Fritchman, Chrissy Moyer, Peter Bryan, Roger Morris, Carl Bowman, Jake Horn, Gene Matlock, and Prisca Vidanage.

Finally, and perhaps most importantly the author would like to thank her family and friends for their support and encouragement throughout her Ph.D studies. In particular the author would like to thank her mother Angie Cercone, father Patrick Cercone and sisters Jenna and Nicole Cercone for their love and support not only during her doctoral studies but throughout her entire life. The author would also like to thank all her fellow graduate students here at Lehigh who have made the last five years a very memorable experience, especially: Vasileios Christou, Pat Trasborg, Aman Karamlou, Michele Tillotson, Matt Gombeda, and Matt Horner.

The material in this dissertation is based on work supported by the National Science Foundation, Federal Highway Administration and Pennsylvania Department of Transportation.

TABLE OF CONTENTS

Certificate of approval.....	iii
Acknowledgements	iv
Table of Contents	vi
List of Tables	xii
List of Figures	xv
Abstract	1
Author's Contributions	6
1. Introduction.....	8
2. Site Assessment Procedures for Structures Subjected to Tsunami Generated Debris Impacts	12
2.1. Introduction.....	12
2.2. Background	14
2.2.1. Tsunami Events and the Impact on Structures.....	14
2.2.2. Terminology and ASCE 7 Provided Data	15
2.2.3. Debris Impact Forces.....	17
2.2.4. Energy Grade Line Analysis	19
2.2.5. Digital Elevation Model Data	21

2.3. Site Assessment Procedures.....	22
2.3.1. Debris Categorization	22
2.3.2. Debris Transport	29
2.3.3. Debris Impact Hazard Region	39
2.3.4. Contour Mapping	49
2.4. Modified Energy Grade Line Analysis	52
2.4.1. Performance of the Energy Grade Line Analysis	53
2.4.2. Modifications to the Energy Grade Line Analysis Method	61
2.4.3. Sensitivity of EGL Analysis to Digital Elevation Models	68
2.5. Future Work.....	70
2.6. Conclusions and Contributions.....	72
3. Innovative shear connector for composite systems	74
3.1. Introduction.....	75
3.2. Background	77
3.2.1. Composite Systems.....	77
3.2.1.1. Shear Connectors.....	77
3.2.2. FlexBeam Flexural Design Prototype.....	82

3.3. Shear Strength Evaluation	85
3.3.1. Experimental Test Specimen Design	86
3.3.2. Experimental Testing Matrix	89
3.3.3. Experimental Setup and Procedure.....	92
3.3.4. Experimental Results.....	94
3.3.4.1. Cylinder Compressive Strength Testing and Reinforcement Yield Strength	94
3.3.4.2. FlexBeam Shear Test Data Summary.....	94
3.3.4.3. FlexBeam Specimen Damage.....	100
3.3.4.4. Post-Testing Specimen Destructive Evaluation	105
3.3.5. Comparison of Experimental Results to Analytical Approaches	111
3.3.5.1. Analytical Equations	111
3.3.5.2. Comparison of analytical equations and experimental results.....	115
3.3.5.3. Development of FlexBeam Shear Equation	118
3.3.5.4. Utilizing Experimental First Peak Load for Design Capacity	132
3.4. FlexBeam Final Prototype Design	135
3.4.1. Shear Transfer Design	135
3.5. Construction Methods.....	141

3.5.1. Steel Sections	141
3.5.2. Constructing the Concrete Deck	142
3.6. Construction Limit State Checks	148
3.6.1. Compression Flange Crushing and Tension Flange Yielding	148
3.6.2. Lateral Torsional Buckling	149
3.7. Future Work.....	152
3.8. Conclusions and Contributions.....	154
4. Nondestructive evaluation techniques for fully grouted post tensioned bridge systems	158
4.1. Introduction	158
4.2. Background	159
4.2.1. Damage Detection Needs for Grouted Post-Tensioned Tendons.....	160
4.2.1.1. Grout Voids	161
4.2.1.2. Strand Corrosion (Corrosion Protection Systems)	162
4.2.1.3. Strand Location	163
4.3. Nondestructive Testing Techniques and Applications	163
4.3.1. Summary of Nondestructive Testing Methods	164
4.3.2. Electrically Isolated Tendons	171

4.3.2.1. Methodology and Application	171
4.3.2.2. Method Limitations	174
4.3.3. Ground Penetrating Radar	175
4.3.3.1. Methodology and Applications	175
4.3.3.2. Limitations	177
4.3.4. Half Cell Potential	179
4.3.4.1. Methodology and Applications	179
4.3.4.2. Limitations	182
4.3.5. Magnetic Flux Leakage	183
4.3.5.1. Methodology and Applications	183
4.3.5.1. Limitations	185
4.3.6. Time Domain Reflectometry	186
4.3.6.1. Methodology and Applications	186
4.3.6.2. Limitations	189
4.4. Experimental Testing Program for Promising Non-Destructive Testing Techniques	192
4.4.1. NDE Testing Recommendations	192
4.4.1.1. Electrically Isolated Tendons	193

4.4.1.2. Internal Half-Cell Potential	194
4.4.2. Testing Methods	196
4.4.2.1. Phase 1 – Half-Cell Potential Testing.....	196
4.4.2.2. Phase 1 Test Procedures	199
4.4.2.3. Phase 2 - Combined Assessment	200
4.4.2.4. Phase 2 Test Procedures	204
4.5. Future Work.....	206
4.6. Conclusions and Contributions.....	207
5. Conclusions	209
References	213
Vita	227

LIST OF TABLES

Table 1: Debris characteristic limits	26
Table 2: Comparison of EGL and Site-Specific Analyses.....	54
Table 3: Comparison of EGL, extended EGL and site specific analyses.....	68
Table 4: Composite Connectors.....	80
Table 5: Comparison of FlexBeam prototype and test specimen	87
Table 6: FlexBeam connector details.....	90
Table 7: FlexBeam Connector Test Matrix.....	91
Table 8: Concrete cylinder strength	94
Table 9: Reinforcement yield strength	94
Table 10: Summary of max capacity and corresponding shear slip	96
Table 11: Shear strength per hole	100
Table 12: Post Testing Specimen Damage	100
Table 13: Test Specimen Connector Plates Post Testing a) Type 2 b) Type 3 c) Type 7 d) Type 8	105
Table 14: Test Specimen Connector Bars Post Testing	106
Table 15: Shear Capacity Equations.....	115
Table 16: Comparison of experimental and analytical shear capacity	116

Table 17: Ratio of predicted strength to experimental capacity	116
Table 18: Mean ratio of predicted strength to experimental capacity.....	116
Table 19: Steel Dowel Shear Force Capacity Factor at First Peak Load	122
Table 20: Steel Dowel Shear Strength Parameter Mean, Standard Deviation and Coefficient of Variation.....	122
Table 21: Shear Force Capacity Factor Steel Dowel	123
Table 22: Shear force capacity factor for Flex Beam concrete dowel at peak	125
Table 23: Shear Force Capacity Factor for FlexBeam Concrete Dowel.....	125
Table 24: FlexBeam Test Specimen Capacity Summary	127
Table 25: Nominal Strength Estimate.....	130
Table 26: FlexBeam Connector Details	137
Table 27: Camber Summary	146
Table 28: Case A Stress Summary	147
Table 29: Case B Stress Summary	147
Table 30: Compression Flange Cracking and Tension Flange Yielding of Composite Section	148
Table 31: Lateral Torsional Buckling of WT Section	149
Table 32: Lateral Torsional Buckling of Composite Section.....	151

Table 33: Summary of NDT Methods 165

LIST OF FIGURES

Figure 1: Small and large debris items (images by Clay Naito and Dan Cox)	27
Figure 2: Moderate debris (image by Clay Naito and Dan Cox)	28
Figure 3: Dispersal regions investigated	30
Figure 4: Sendai large container facility before and after	31
Figure 5: Sendai small container facility before and after	32
Figure 6: Sendai container facility dispersal	33
Figure 7: Ofunato container facility	36
Figure 8: Ofunato container facility dispersal	37
Figure 9: Natori vessel dispersion	38
Figure 10: Kessennuma vessel dispersion	38
Figure 11: Inflow and outflow debris transport	41
Figure 12: Inflow region development	42
Figure 13: Outflow region development	43
Figure 14: Debris impact hazard region applied to shipping vessel dispersion	44
Figure 15: Debris impact hazard region	45
Figure 16: Tsunami design zone for Hilo, Hawaii	46

Figure 17: Debris source Hilo, Hawaii.....	47
Figure 18: Debris impact hazard zone Hilo, Hawaii	48
Figure 19: Inundation depth mapping	50
Figure 20: Flow velocity mapping	50
Figure 21: Impact force mapping	51
Figure 22: Site and Transect Locations.....	53
Figure 23: Digital elevation model using IfSAR topography	56
Figure 24: Digital elevation model using USGS NED topography	57
Figure 25: Elevation difference in feet NGA IfSAR and USGS NED DEM	58
Figure 26: Discrepancy between DEM data and runup model	60
Figure 27: Adjusted inundation Site A normal transect EGL inundation depth comparison	62
Figure 28: Adjusted inundation Site A normal transect EGL velocity comparison.	62
Figure 29: Extended energy grade line transects.....	64
Figure 30: Extended EGL Site A normal transect inundation depth comparison...	64
Figure 31: Extended EGL Site A normal transect velocity comparison.....	65
Figure 32: Comparison of transect inundation results.....	66
Figure 33: Comparison of Site A normal transect velocity results.....	66

Figure 34: Comparison of digital elevation models	69
Figure 35: Mechanical behavior of a Perfobond-rib shear connector (Ahn et al. 2010)	81
Figure 36: FlexBeam connector	81
Figure 37: FlexBeam bridge system cross section	84
Figure 38: Beam section and side elevations (Aghl, Naito & Sause, 2014)	85
Figure 39: End diaphragm details (Aghl, Naito & Sause, 2014)	85
Figure 40: FlexBeam and push-off specimen concepts (longitudinal bars not shown)	86
Figure 41: FlexBeam Test Specimen Schematic.....	88
Figure 42: a) Test specimen fabrication b) Test specimen removed from form work	89
Figure 43: Schematic of a Type 3b test specimen	92
Figure 44: Test Specimen Set Up in Satec Machine.....	93
Figure 45: Experimental testing force-displacement curves	95
Figure 46: Effect of hole size	97
Figure 47: Effect of the concrete dowel	98
Figure 48: Effect of reinforcement size and hole spacing	99

Figure 49: Comparison of Test Specimen Connector Bar Damage	110
Figure 50: Dowel Progression Subjected to Double Shear	110
Figure 50: Shear Force Capacity Factor for Concrete Dowels.....	120
Figure 51: Shear Force Capacity Factor for Steel Dowels	121
Figure 52: Steel Dowel Shear Strength Parameter Thresholds.....	124
Figure 53: Shear Forcer Capacity Factor for Concrete Dowel	125
Figure 54: FlexBeam Shear Demands	136
Figure 55: Discrete Interface Shear Capacity	139
Figure 56: Average Interface Shear Capacity and Demands.....	139
Figure 57: Proposed shear transfer detail for PA FlexBeam	140
Figure 58: WT fabrication	142
Figure 59: Construction case A	143
Figure 60: Construction case B	144
Figure 61: Stages of beam deformation	145
Figure 62: Section stress locations	146
Figure 63: Electrically Isolated Tendon Measuring Principles Schematic.....	172
Figure 64: Schematic of GPR Process in PT Systems	176

Figure 65: Half-cell potential map (Naito, Jones and Hodgson, 2010).....	180
Figure 66: External Half-Cell Electrode Application	181
Figure 67: Magnetic flux leakage due to defect of the strand	184
Figure 68: Block diagram for TDR application it PT systems (modified from Lui et al. 2002).....	187
Figure 69: Time domain reflectometry application for grout void detection	188
Figure 70: Half-cell testing layout.....	200
Figure 71: EIT test layout.....	204

ABSTRACT

The design of structural systems is a complex process which encompasses many different aspects of structural engineering. The design process includes understanding the load demands placed on the system, designing and detailing the structural components to withstand the demands and the fabrication/construction of the final system design. The work presented in this dissertation covers a breadth of topics within the field of structural engineering including: site assessment procedures for structures subjected to tsunami generated debris, the development of an innovative composite bridge system and shear connection and non-destructive evaluation of fully grouted post-tensioned bridge systems. Collectively, the original research contributions in each of three topics resulted in improvements to the overall design process of structural systems. The advancements to the design process presented in this dissertation include: assessment of demands on structural systems, developing new detailing of structural components, overall design changes to allow for improved inspection techniques and the development construction and fabrication methods for a prototype system.

Currently, the United States has no codified guidelines in place for designing against the effects of tsunami events despite having a number of tsunami prone areas including: Alaska, California, Hawaii, Oregon and Washington. The lack of design guidance has left many coastal communities in the U.S. at risk. Recent tsunami events including Japan 2011, Chile 2010 and Indian Ocean 2004, motivated the engineering community to understand the effects of these events and to develop methods to design structural systems to withstand tsunami generated loads. This research effort was focused on developing site assessment procedures for structures subjected to tsunami generated debris impacts. A debris classification system was developed to group debris by the potential impact demand each item can generate. Four characteristics that contribute to the impact force demand for

debris items were identified including debris: mass, stiffness, buoyancy and cumulative length. Based on these characteristics debris items are grouped into three categories, small, moderate or large debris. Small debris items will generate low level demands on the systems typically an impact force of 6000 lbs. or less large debris items will generate extreme levels of demand, typically an impact force of 1000 kips or greater and moderate debris is any debris item that generates an impact force that falls in-between.

Large debris items such as shipping containers and shipping vessels can place extreme loads on structural systems resulting in collapse of the system if not properly designed. An impact hazard region was developed which provides design engineers with a probable region over which large debris items will disperse in a tsunami event. Knowing the location of the debris origin and the assumed flow direction of the event the impact hazard region can be constructed for any tsunami prone location. The development of the debris impact hazard region allows design engineers to determine, based on the location of a structure, if design against impact of large debris is necessary. The impact hazard region has been adopted by ASCE 7-16.

The energy grade line (EGL) method, used to approximate water velocity and inundation height at a building site within an inundation region, has not yet been widely validated within the archival literature. Analytical results utilizing the EGL method were generated for a region of Hawaii and compared with results from a two-dimensional tsunami inundation simulation. Based on this comparison it was found that the EGL was under estimating the water velocity and inundation compared to the site-specific analysis. This under estimation was attributed to the discrepancy in runup elevation at the inundation limit provided by ASCE runup data and the corresponding elevation obtained for the same location using the available

digital elevation model data. A modification to the EGL method to account for this discrepancy in elevation was proposed to improve the estimates of the EGL method, which extends the EGL transect past the inundation limit to an elevation on the DEM equal to the runup elevation provided by ASCE. Applying the modification to the energy grade line method results in more conservative approximations of water velocity and inundation height than the traditional energy grade line method as compared with the results of the site-specific analysis.

Composite bridge systems have gained interest in the structural engineering community due to the ability for these sections to be cost effective alternatives to traditional steel or concrete systems. When properly designed, these systems take advantage of the ability for concrete to perform well under compressive stress and the ability of steel to resist the tensile stress. Composite systems can also allow for a more rapid construction time as a result of the ability for these sections to be prefabricated. The result of this research project is the development of a precast steel/concrete composite highway bridge system whose beam components are light-weight and easy to erect and fabricate. This research effort examines the shear transfer mechanism between the concrete slab and WT web and developed construction methods for the prototype system.

A series of potential shear connector details were experimentally examined with push-off tests for the shear connection developed for the prototype system. A number of shear connector detailing parameters including the effect of: hole size, hole spacing, bar size and bar geometry were investigated. It was found that increasing the hole size and bar size increased the shear capacity of the connection. Increasing the hole spacing resulted in a decrease in capacity and bending the rebar as opposed to using straight bars increased the capacity. Based on the experimental testing the connector details utilized in the prototype system design was 1.5 inch

holes with #6 bars through every hole, where the spacing of the holes is dependent on the shear demand along the length of the beam.

Based on the experimental test data and destructive evaluation of the test specimens the failure mechanism for the connectors was determined attributed to two mechanisms. In the case where no reinforcement was placed through the connector the ultimate strength is attributed to shearing of the concrete dowels and in the case where rebar was placed through every connector hole the ultimate strength is attributed to initial yielding of the reinforcing bar. A design equation to approximate the capacity of the shear connection was developed based on the observed failure mechanisms and experimental test data.

The prototype system shear details were designed based on the developed equation to approximate the shear capacity of the connection. The final design for the WT 20 x 74.5 system required 50 1.5 inch holes, with #6 bars in every hole in the half-span. Three different hole spacing was utilized in the half-span to meet the shear demands: 4 in., 6 in. and 11.25 in. spacing. Fabrication and construction methods were established for the newly developed prototype system, which were aimed at reducing fabrication cost and assuring critical dimensions of the system, such as embedment of the WT into the deck, are maintained for all precast components. Due to the fact that the WT section as well as the individually precast composite segments can be unstable at long lengths, a laterally torsional buckling analysis of the sections was performed. AISC design equations can directly be applied to the WT section; however, for the composite section design equations are not available so as part of this effort the available AISC equations were modified based on concrete limit states for construction loading and applied to the individual precast components.

Post-tensioned concrete bridges represent a major component of the American bridge inventory and due to the benefits provided by this construction technique it is likely that many new post-tensioned concrete bridges will be built in the future to meet our infrastructure needs. However, recent cases in which corroded post-tensioning tendons were identified have caused industry wide concern and lead to a moratorium on post-tensioned constructions in some states. Post-tensioning systems are comprised of unique structural details including prestressing strand, ducts, anchorages, grout, and corrosion protection equipment. Current details for the construction of post-tensioning tendons do not facilitate the long term inspection of the various tendon components. As part of this research effort a state of the art review of available NDE techniques that can be applied to fully grouted post-tensioned systems was conducted. Currently available NDE methods were grouped into four different categories by monitoring capabilities: grout voids identification, strand corrosion detection, identification of tendon location and determining loss of prestress. Based on the state of the art reviews it was concluded that methods that can be directly integrated into future construction show the most promise for long term monitoring of post-tensioned tendons. A testing plan for two promising non-destructive testing methods, the electrically isolated tendon system and internal half-cell potential method, was developed. This testing plan has not yet been implemented, but outlines the design of a test specimen and testing procedures that can be utilized to verify the long term monitoring capabilities of the system as well as perform a sensitivity study on the level of damage which can be detected.

AUTHOR'S CONTRIBUTIONS

The original research contributions presented in this dissertation cover a breath of topics with in the field of structural engineering. Although the contributions come from different areas within the field, collectively, the original research contributions result in improvements to the overall design process of structural systems. This includes advances in the overall system design, to the design of structural details, as well as the demands that are utilized in the design process. Summarized below are the original contributions in the field of structural engineering based on the research projects described within:

1. A debris classification system for tsunami generated debris items was developed which categorizes debris as small, moderate or large based on the potential impact force the debris item can generate.
2. A debris impact hazard region was established which is used to quantify a probable dispersion region for which structures must be designed to withstand impacts from large debris items such as shipping vessels and shipping containers. The debris impact hazard region has been adopted by ASCE 7-16.
3. A modification to the energy grade line method was developed to account for potential nonzero inundation depths at the inundation limit caused by modeling discrepancies between the average elevation assumed by the large grid size used in the site-specific model and the elevation determined using the digital elevation model data for the same point.
4. Experimental data was generated for the FlexBeam shear connection that includes the investigation of different detailing parameters such as hole size, reinforcement size, reinforcement geometry and hole spacing on the overall shear capacity of the connection.

5. A design equation to approximate the shear capacity of a FlexBeam connection based on varying connection details was established.
6. Design of a prototype FlexBeam component to meet all PennDOT design standards for flexure and shear.
7. Fabrication and construction methods were established specifically for the FlexBeam system. As part of this effort modifications to AISC equations for lateral torsional buckling of steel sections were made to perform a lateral torsional buckling analysis of a single precast composite FlexBeam section under construction loading.
8. A state of the art review of currently available nondestructive evaluation techniques that can be applied for long term monitoring of fully grouted post-tensioned system was conducted.
9. Promising nondestructive evaluation techniques that can be integrated in to future post-tensioned construction were identified. A proposed testing plan that can be used to validate damage detection capabilities and perform sensitivities studies for damage assessment was developed for the electrically isolated tendon system and the internally embedded half-cell probe.

1. INTRODUCTION

The work presented in this dissertation covers a breath of topics within the field of structural engineering including: site assessment procedures for structures subjected to tsunami generated debris, the development of an innovative composite bridge system and shear connection and non-destructive evaluation of fully grouted post-tensioned bridge systems. These research projects were funded by three different funding agencies, respectively: the National Science Foundation (NSF), the Pennsylvania Department of Transportation (PennDOT) and the Federal Highway Administration (FHWA). Although the areas of research and funding agencies are quite diverse the overall goal of each research effort is to improve the current design procedures and structural component and system details in the field of structural engineering.

The design of structural systems is a complex process which encompasses many different aspects of structural engineering. In a very general sense the design process includes understanding the demands placed on the system, designing and detailing the structural components to withstand the demands and the fabrication/construction of the final system design. Collectively, the original research contributions in each of three topics result in improvements to this overall design process. The advancements to the design process include: assessment of demands on structural systems, developing new detailing of structural components, overall design changes to allow for improved inspection techniques and the development construction and fabrication methods for a prototype system. This section provides a general overview of the main objectives of each research topic.

Currently, the United States has no codified guidelines in place for designing against the effects of tsunami events despite having a number of tsunami prone areas including: Alaska, California, Hawaii, Oregon and Washington. The lack of design

guidance has left many coastal communities in the U.S. at risk. Recent tsunami events including Japan 2011, Chile 2010 and Indian Ocean 2004, motivated the engineering community to understand the effects of these events and to develop methods to design structural systems to withstand tsunami generated loads. The goal of this research effort is to investigate the potential for debris impacts to structural systems that can be generated during tsunami events. Large debris items such as shipping containers and shipping vessels can place extreme loads on structural systems resulting in collapse of the system if not properly designed. A procedure to quantify a probable debris dispersal region was developed as part of this effort and adopted by ASCE 7-16, Chapter 6: Tsunami Loads and Effects. Common tsunami debris types were identified from field observations and a categorization system for tsunami generated debris is established. In addition to developing site assessment procedures for structures subjected to tsunami generated debris, a simple method (energy grade line method) for approximating flow characteristics outlined in ASCE 7-16 is evaluated. The energy grade line (EGL) method has not yet been widely validated within the archival literature, therefore analytical results utilizing the method were generated for a region of Hawaii and compared with results from a two-dimensional tsunami inundation simulation. Based on this comparison a modification is proposed to improve the estimates of the EGL method. The overall focus of this research effort is to improve design guidance on the structural demands imparted on structures within inundated regions due to tsunami borne debris impacts.

Composite bridge systems have gained interest in the structural engineering community due to the ability for these sections to be cost effective alternatives to traditional steel or concrete systems. When properly designed, these systems take advantage of the ability for concrete to perform well under compressive stress and the ability of steel to resist the tensile stress. Composite systems can also allow for

a more rapid construction time as a result of the ability for these sections to be prefabricated. The goal of this research project is to develop precast steel/concrete composite highway bridge system whose beam components are light-weight and easy to erect and fabricate. This research effort examines the shear transfer mechanism between the concrete slab and WT web and develops construction methods for the prototype system. A series of potential FlexBeam connector details were experimentally examined with push-off tests. Utilizing the experimental data generated from the push-off tests a design equation to predict the shear capacity of the FlexBeam connector was developed. Utilizing the flexural design of the selected prototype WT20x74.5 FlexBeam system, shear connection details were designed. Construction methods for fabrication and erection of the FlexBeam components are also developed.

Post-tensioned concrete bridges represent a major component of the American bridge inventory and due to the benefits provided by this construction technique it is likely that many new post-tensioned concrete bridges will be built in the future to meet our infrastructure needs. However, recent cases in which corroded post-tensioning tendons were identified have caused industry wide concern and lead to a moratorium on post-tensioned constructions in some states. Post-tensioning systems are comprised of unique structural details including prestressing strand, ducts, anchorages, grout, and corrosion protection equipment. Current details for the construction of post-tensioning tendons do not facilitate the long term inspection of the various tendon components. The goal of this research project is to identify nondestructive testing (NDT) techniques that can be applied to post-tensioning systems for long term monitoring of tendon condition. Due to the fact that many of these nondestructive testing techniques are not currently used in the United States to monitor PT systems an experimental testing program is developed

to investigate promising NDT methods monitoring capabilities in fully grouted PT systems.

Overall the research conducted on these three topics in structural engineering resulted in the advancement of the current state of design practice. The contributions to the field of structural engineering include improvements in assessing structural demands in tsunami prone regions, shear connection detailing and fabrication/erection for composite systems, and post-tensioning component detailing and overall system design to accommodate inspection techniques.

2. SITE ASSESSMENT PROCEDURES FOR STRUCTURES SUBJECTED TO TSUNAMI GENERATED DEBRIS IMPACTS

This research project is part of a much larger effort funded by the National Science Foundation to develop design guidance for structures subjected to tsunami loads. The work presented in this chapter was done in collaboration with researchers at a number of different Universities and has been presented in the following publications: Naito, Riggs, Wei and Cercone (Accepted 2016); Riggs, Naito, Cercone and Wei (2015); Naito, Cercone, Riggs, and Cox (2014).

2.1. Introduction

Currently the United States has no codified guidelines in place for designing against the effects of a tsunami event despite having a number of tsunami prone areas including: Alaska, California, Hawaii, Oregon and Washington. The lack of design guidance has left many coastal communities in the U.S. at risk. In an effort to alleviate the potential risk to coastal communities ASCE 7 has developed a new chapter entitled Tsunami Loads and Effects that will be incorporated in the 2016 edition of ASCE 7 Standard, Minimum Design Loads for Buildings and other Structures. This research effort is focused on the potential for debris impacts to structural systems that can be generated during tsunami events. Large debris items such as shipping containers and shipping vessels can place extreme loads on the structures they impact resulting in collapse of the system if not properly designed. A procedure to quantify a probable debris dispersal region has been developed by this research effort and adopted by the new ASCE 7 chapter on tsunami loads and effects. In addition a common tsunami debris types have been identified and a categorization system for tsunami generate debris is proposed.

The 2016 publication of the ASCE 7 design standard provides a new, relatively simple 'energy grade line' (EGL) method that can be used to obtain estimates for

the design flow velocity and depth at a location in the inundation zone. The flow velocity is used to determine the design impact force on a structure and the depth is utilized to define the height up to which that impact must be considered. The energy grade line method has not yet been widely validated within the archival literature, therefore the results of this method are compared with results from a two-dimensional tsunami inundation simulation. Based on this comparison a modification is proposed to improve the estimates of the EGL method.

2.2. Background

2.2.1. Tsunami Events and the Impact on Structures

Recent Tsunami events such as Japan 2011, Chile 2010 and Indonesia 2004 have illustrated that the consequences on tsunamis can be catastrophic. In the Japan 2011 event alone the losses are estimated at \$100 to \$500 billion in property damage with a death toll of 15,534 and 7,092 reported missing (EERI, 2011). The hydrostatic and hydrodynamic forces generated by the tsunami event were responsible for the vast majority of the losses in Japan. Significant research has been carried out on quantifying these forces; for example (Cross 1967, Ramsden and Raichlen 1990, Ramsden 1996, Asakura et al. 2000, Asakura et al. 2002, Arnason et al. 2009, Fujima et al. 2009 and Robertson et al. 2013). Design guidelines for such events include (Yeh 2006, Yeh 2007, OCADI 2009 and FEMA 2012). It is not economically practical or necessary to design all structures in tsunami prone locations to resist these forces. However, all structures whose failure would result in unacceptable losses, including designated evacuation shelters and critical facilities, should be designed to survive tsunami loads. Tsunami generated loads not only include the hydraulic and inundation force but also potential impact force from tsunami-borne debris. Although much attention has been devoted to assessing the risk of a tsunami event, there has been much less focus on the assessment of the potential for tsunami debris strikes on structures.

Tsunami debris impacts can place large levels of demand on the structures they strike. To design structures in a tsunami prone site, an assessment of the likelihood of tsunami debris impact should be carried out, including an understanding of the type and distribution of potential debris, and the forces generated by impact. Currently, no standardized site assessment procedures for tsunami generated impact force exist. A site assessment procedure is developed and outlined herein to

assess the site-specific potential for debris impact and its significance to structures. The procedure provides a debris classification system and establishes a debris hazard zone based on the potential for debris transport.

2.2.2. Terminology and ASCE 7 Provided Data

The intent of this section is to provide the ASCE 7-16 definitions of the terminology utilized throughout this chapter that may be unfamiliar to structural engineers. In addition this section will provide clarity on what specific datasets will be available for download by ASCE.

In order to perform impact analysis for tsunami generated debris design engineers will need to obtain a number of different datasets. ASCE will be making available the Tsunami Design Geodatabase which contains runup elevation and inundation geocoded reference points as well as tsunami design zone maps which will provided as keyhole markup language zipped (KMZ) files. Design engineers will also need to obtain the a digital elevation model (DEM) dataset for the tsunami prone region under investigation. A digital elevation model with a resolution of at least 1/3 arc sec ((approximately 33 ft. (10 m)) will be required. The metadata associated with the dataset will specify the resolution. For most areas DEM data with the required level of resolution can be obtained from the NOAA National Centers for Environmental Information (NCEI) (NOAA, 2015).

The following terminology is defined as applied to ASCE 7-16 Chapter 6 Tsunami Loads and Effects (ASCE 7 2016):

ASCE Tsunami Design Geodatabase: The ASCE database (version 2016-1.0) of geocoded reference points of Offshore 328 ft. (100m depth) Tsunami Amplitude, H_T , and Predominant Period, T_{SU} , of the Maximum Considered Tsunami, disaggregated hazard source contribution figures, probabilistic subsidence, Runup

Elevation and Inundation geocoded reference points, and Tsunami Design Zone maps.

Hydrodynamic Loads: Loads imposed on an object by water flowing against and around it.

Hydrostatic Loads: Loads imposed on an object by a standing mass of water.

Impact Loads: Loads that results from debris or other object transported by the design tsunami striking a structure or portion thereof.

Inundation Depth: The depth of design tsunami water level, including relative sea level change, with respect to the grade plane at the structure.

Inundation Elevation: The elevation of the design tsunami water surface, including relative sea level change, with respect to vertical datum North American Vertical Datum (NAVD-88).

Inundation Limit: The maximum horizontal inland extend of flooding for the Maximum Considered Tsunami, where the inundation depth above grade becomes zero; the horizontal distance that is flooded, relative to the shoreline defined where the North American Vertical Datum (NAVD-88) elevation is zero.

Momentum Flux: The quantity $\rho_s h u^2$ for a unit width based on the depth-averaged flow speed u , over the inundation depth h , for equivalent fluid density ρ_s having the units of force per unit width.

Runup Elevation: Ground elevation at the maximum tsunami inundation limit, including relative sea level change, with respect to North American Vertical Datum (NAVD-88) reference datum.

Topographic Transect: Profile of vertical elevation data versus horizontal distance along a cross-section of the terrain, in which the orientation of the cross-section is perpendicular or at some specified orientation angle to the shoreline.

Tsunami: A series of waves with variable long periods, typically resulting from earthquake induced uplift or subsidence of the sea floor.

Tsunami Design Zone: An area identified on the Tsunami Design Zone Map between the shoreline and the inundation limit, within which structures are analyzed and designed for inundation by the Maximum Considered Tsunami.

Tsunami Design Zone Map: The map given ASCE 7-16 Figure 6.1-1 designating the potential horizontal inundation limit of the Maximum Considered Tsunami, or a state or local jurisdiction's probabilistic map produced in accordance with ASCE 7-16 Section 6.7.

Tsunami Prone Region: The coast region in the U.S. addressed by ASCE 7-16 Chapter 6 with quantified probability in the Recognized Literature of tsunami inundation hazard with Runup greater than 3 ft. (0.914 m) due to tsunamigenic earthquakes in accordance with the Probabilistic Tsunami Hazard Analysis method given in Chapter 6.

Tsunami Risk Category: The Risk Category from ASCE 7-16 Section 1.5, as modified for specific use related to Chapter 6 per Section 6.4.

2.2.3. Debris Impact Forces

The goal of the site assessment procedures developed during this research effort is to determine if a structure needs to be designed to withstand a debris impact from a particular type of debris. The next step is to then quantify the possible impact

force that can be generated on the structure. This section summarizes the available guidance to quantify tsunami generated impact forces on structural systems.

FEMA P646 §6.5.6 (2012) specifies that debris impact forces be estimated by Equation 1.

$$F = 1.3 \cdot U_{max} \sqrt{k \cdot m_d (1 + c)} \quad \text{Equation 1}$$

in which 1.3 is the importance coefficient for risk category IV (i.e., essential facilities), U_{max} is the max flow velocity carrying the debris, m_d is the mass of the debris, k is an effective stiffness of the debris, and c is the hydrodynamic mass coefficient. Applying this equation requires the knowledge of the mass and stiffness properties of the debris. P646 also provides mass and stiffness values for wood poles and shipping containers, however for other common tsunami debris types such as shipping vessels and passenger vehicles these properties must be estimated.

Equation 1 was provided in FEMA P646 as a guideline, but the equation has not yet been validated. Until further understanding has been reached, Equation 2 can be applied to quantify the impact forces, which takes on a similar form but drops the 1.3 safety factor and assumes the added mass coefficient is zero.

$$F = v \sqrt{k m_d} \quad \text{Equation 2}$$

in which v is the impact velocity, k is the relevant debris stiffness, and m_d is the debris mass.

The maximum flow velocity of water carrying the debris needs to be determined to apply these impact force equations. ASCE 7 provides two methods that can be applied to determine the water velocity and inundation depth at any location within the inundated region. Determining realistic estimates for the water velocity is

important as this flow characteristic is used to determine the impact force is applied to the structure. For this reason these two methods, energy grade line and site-specific analysis, for approximating flow velocity and inundation depth are explored further in this research study.

2.2.4. Energy Grade Line Analysis

The 2016 publication of the ASCE 7 design standard "Minimum Design Loads for Buildings and Other Structures" will provide two methods for calculating the design velocity and inundation depth at a site within the inundation zone: (1) The Energy Grade Line Method and (2) A Site-Specific Inundation Analysis. The standard defines which method should be applied to a given building site based on the tsunami risk building category of the structure.

The site-specific inundation analysis will only be required for the highest tsunami risk category buildings (category IV) due to the fact that the analysis is complex and in general requires expertise in tsunami inundation modeling. A site-specific inundation analysis requires at least a depth-integrated two-dimensional model for fluid flow. There are currently several software packages available to perform such an analysis, such as MOST/ComMIT (Titov et al. 2011).

The energy grade line method is a new simplified approach that has been developed to estimate the water velocity and inundation depth at a site in lieu of performing a site specific analysis. The energy grade line analysis will be required of all structures subjected to the tsunami design procedures due to the fact that velocities from a site specific analysis cannot be used to reduce the design values below a specified percent of those from an EGL analysis. The advantage of the EGL method is that it is computationally straightforward calculation procedure that can be performed using a spreadsheet program. This makes this method advantageous for

use in a typical structural design office. The EGL equation is presented in Equation 3 (ASCE 7 2016), where this equation is applied in maximum increments of 100 ft. (30.5 m) along a topographic transect that runs from the inundation limit to the shoreline. Applying Equation 4 (ASCE 7 2016) the water velocity can also be determined at each increment along the transect.

$$E_{gi+1} = h_i(1 + 0.5F_{ri}^2) + (\varphi_i + s_i)\Delta x_i \quad \text{Equation 3}$$

$$u_i = F_{ri}\sqrt{gh_i} \quad \text{Equation 4}$$

where E is the energy head, h is the inundation depth, Fr is the Froude number, s is the friction slope, φ is the ground slope, Δx is the segment increment, u is the water velocity and i is the increment index.

The energy grade line analysis was developed to produce statically conservative results, at least for the maximum momentum flux that is used for the hydraulic loading. The energy grade line method is a linear transect analysis which means that it is incrementally applied over a topographic line, which in this application runs from the inundation limit to the coast line. As a linear transect analysis it cannot capture the two-dimensional flow and directionality effect that site-specific inundation modeling can. As a means to establish the appropriate statistical analysis and conservative bias in the EGL method, 36,000 trial numerical code simulations were performed versus the EGL analysis method (ASCE 7 2016).

Although the energy grade line method offers many advantages, in terms of its computational simplicity and claims to produce conservative flow parameters, it has not yet been widely validated within the archival literature. Therefore as part of this research effort an investigation is conducted in which the results of this method are compared with results from a two-dimensional tsunami inundation simulation. Based on this comparison a modification to the current EGL method is proposed to

improve the estimates of the water velocity and inundation depth at a given site within the tsunami design zone. In addition a sensitivity study to the digital elevation model utilized when conducting the energy grade line method was performed.

2.2.5. Digital Elevation Model Data

In order to perform both the energy grade line analysis and the site-specific analysis the digital elevation data for the region under investigation is required. Ground elevations can be obtained from a number of sources but the datasets many not all be of the same resolution or level of vertical accuracy. When applying the EGL and site-specific methods a digital elevation model (DEM) with a resolution of at least 1/3 arc sec ((approximately 33 ft. (10 m)) will be required. The metadata associated with the dataset will specify the resolution. For most areas DEM data with the required level of resolution can be obtained from the NOAA National Centers for Environmental Information (NCEI) (NOAA, 2015).

The digital elevation modal data is provided in the format of a 'matrix' of elevation values referenced to a vertical datum of Mean High Water (MHW), North America Vertical Datum of 1988 (NAVD88), or Mean Sea Level (MSL). The metadata specify the datum as well as the latitude and longitude at the bottom left of each cell. The cell size is dependent on the DEM resolution. The DEM data can be viewed using a variety of software tools, including ArcGIS (ESRI, 2015) and Matlab (MathWorks, 2015). For this research project Matlab was utilized.

2.3. Site Assessment Procedures

The overall goal of the developed site assessment procedures is to determine a structures susceptibility to debris impact during a tsunami event. These procedures require an assessment of the type of debris likely to be present at a given site and the potential for that debris to generate significant impact forces, a debris classification system to determine potential impact demands levels, and an assessment of the potential for debris to be transported to a given building site.

2.3.1. Debris Categorization

Videos and photos from the Tohoku event were studied to identify common debris types generated during the event in Japan. Many different inundated locations were studied and a list of common debris types was compiled. Some commonly identified debris items include; wood poles, trees, wood structures, vehicles, shipping containers and shipping vessels. ASCE 7 will provide mass and stiffness properties of some of the commonly identified debris types for impact force calculation purposes.

Developing a debris categorization system is important as ASCE 7 cannot provide the mass and stiffness properties for all possible debris types. Without these properties it can be difficult to calculate impact force demands generated by a particular debris item. The goal of the developed debris classification system is to categorize debris by the level of impact force it can generate. This would allow engineers to approximate the impact force demands of any debris type based on impact demands of common debris types in the same category for which guidance is provided in ASCE 7.

Based on the goal of the categorization system to group debris based on impact demands the debris objects are divided into three categories: small debris,

moderate debris, and large debris. Small, dispersed debris are defined as suspended objects that are not large enough to impart significant force on impact. Moderate debris objects can result in localized impact damage as well as damming on structures and would represent a typical force demand. Large debris objects can impart excessive force on impact and produce significant damage to an engineered structure.

In order to determine if a debris item is considered small, moderate or large debris, four quantitative debris characteristics are identified: (1) mass, m_d , (2) stiffness, k , (3) size, L , and (4) buoyancy, B . Each characteristic directly influences the potential for the debris to cause significant impact forces. For example, as the mass and stiffness of a debris item increase so does the potential the impact force (Paczkowski et al. 2012). Also, as the size of the debris increases the likelihood of structural impact increases. Lastly, the velocity of buoyant debris will be higher than that of non-buoyant debris, and the transport of non-buoyant debris is much more difficult.

These four quantitative debris characteristics are used to categorize a debris item as small, moderate or large debris. Each of the four characteristics are divided into groups I, II, and III, as follows. An object is in mass group I if its mass is less than the mass of a 30 ft (9 m), 1000 lb (450 kg) wood utility pole, which is the weight of a nominal debris log as specified by a design guide for floods (ASCE 2010). It is in mass group III if its effective mass is greater than the mass of a loaded 20 ft (6.1 m) shipping container, i.e., 66,000 lb (30,000 kg). Effective mass is the mass that is rigidly attached to the debris 'structure'. For example, loosely-loaded shipping container contents do not contribute to the effective mass. Objects with mass between these two limits are assigned to mass group II.

For stiffness, an object is in group I if its impact stiffness is less than 0.57 k/in. (0.10 kN/mm). This value is chosen based on limiting the impact force produced by

a small debris item to 6000 lb (26.7 kN), which is the impact force design requirement for vehicle barrier systems of parking structures (ASCE 2010). It is envisioned that many steel and concrete structures that would be constructed as evacuation shelters or used as unofficial evacuation shelters would be able to withstand this impact force with very little additional design considerations. (Paczkowski et al. 2012) proposed that the peak impact force can be estimated from Equation 2.

The impact velocity can be assumed to be 9 mph (4 m/s) when site-specific flow velocities are not available. This assumption is based on previous field observations of flow velocity, where measured flows from the 2004 Indian Ocean Tsunami were measured within the range of 4.5 to 11 mph (2 to 5 m/s) (Fritz et al. 2006). Based on the suggested maximum impact force value of 6000 lb, the assumed velocity of 9 mph and a group I debris mass of 1000 lb, the maximum stiffness for stiffness group I is established as 0.57 kip/in. In the same way, a limiting impact force value can be established for an object that would have a mass and stiffness in group III. An object that is in both mass and stiffness groups III will have an impact force in excess of 1000 kips (4500 kN). Therefore, any object with a stiffness of a 20 ft. ISO shipping container (estimated at 245 k/in or 43 kN/mm (Riggs et al. 2013) for a bottom corner impact) or greater is in stiffness group III. It is expected that this demand will be beyond the design of typical structures, but could be considered when designing evacuation shelters. Objects with a stiffness in the intermediate range are assigned to stiffness group II.

Length groups are established based on the cumulative length of the debris object. Due to the fact that many of the debris items can be irregularly shaped the cumulative length is defined as the sum of the length, width, and height of a bounding box around the object. Cumulative length is related to the likelihood of a

debris object striking a critical structural component. It is reasonable to assume the as the cumulative length of the object increases so does the likelihood of impact by that object. This assumption is based on fact that the debris volume rather than the length alone influences the ability to impact a column or beam. The length groupings are established based on the following. Objects with a cumulative length less than 14 ft. (4.27 m) are in length group I. Objects in length group III are larger than 40 ft. (12.2 m). These limits are based on having anything smaller than a passenger vehicle classified as group I and anything bigger than a 20 ft. (6.1 m) shipping container be classified as group III. Objects with intermediate lengths are assigned to length group II. Only buoyancy groups I and III are defined. Buoyancy group III includes all debris that is able to float given that the flow depth is high enough. Buoyancy group I is assigned to debris that does not float.

The established characteristic groupings for mass, stiffness, length and buoyancy are used to assign a specific debris item to one of the three debris categories (small, moderate and large). Objects that have been assigned to group I for at least three characteristics are categorized as small. To qualify as large debris, a debris item must have been assigned to group III for at least three of the four characteristics. Any debris item falling between the requirement of small debris and large debris is placed in the moderate category. The limiting values for each category of mass, stiffness, buoyancy and length are summarized in Table 1.

Table 1: Debris characteristic limits			
Category	I	II	III
Mass, m	< 1 kip	1 to 66 kip	> 66 kip
Stiffness, k	< 0.57 kip/in	0.57 to 245 kip/in	> 245 kip/in
Buoyancy	Not Buoyant	Not Applicable	Buoyant
Size	< 14 ft.	14 to 40 ft.	> 40 ft.

To demonstrate how this debris classification system is applied to tsunami generated debris items the outlined procedure was applied to common debris items observed in Japan. The common debris items were identified through video, satellite images and found during a post event site survey of debris generation in inundated regions of Natori, Sendai, Ofunato, Minami-sanriku, Kesenuma, Rikuzentakata, Onagawa, and Ishinomaki Japan (Naito et al. 2012). The characterization of these debris items, which are also present in many coastal communities, is presented in Figure 1 and Figure 2.



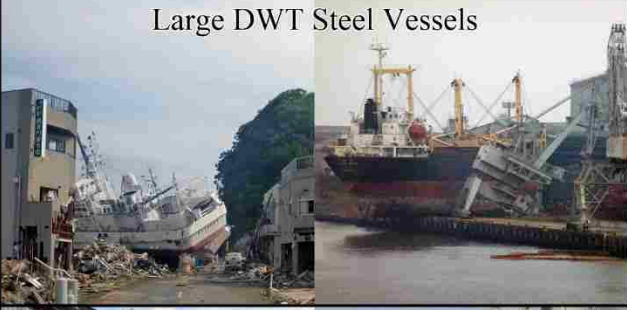

Category	Sample Cases	Characteristics			
		M	K	L	B
Small Debris	<p>Natural and Manufactured Materials</p> 	I	I	I	III
Large Debris	<p>Wood Structures</p> 	III	I	III	III
Large Debris	<p>Large DWT Steel Vessels</p> 	III	II	III	III
Large Debris	<p>Loaded Containers and Trailers</p> 	III	III	II	III

Figure 1: Small and large debris items (images by Clay Naito and Dan Cox)

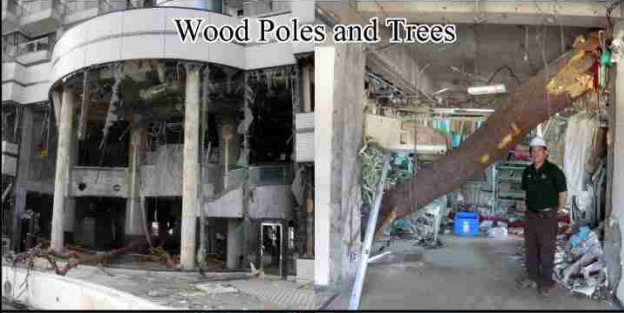




Moderate Debris - Sample Cases	Characteristics			
	M	K	L	B
<p>Wood Poles and Trees</p> 	I	II	II	III
<p>Empty Containers and Trailers</p> 	III	II	III	II
<p>Concrete and Stone Objects</p> 	III	III	I	I
<p>Vehicles</p> 	II	II	II	III
<p>Fiberglass Low DWT Vessels</p> 	II	II	II	III

Figure 2: Moderate debris (image by Clay Naito and Dan Cox)

2.3.2. Debris Transport

During a tsunami buoyant debris can easily be transported across an inundated regions by the inflow and outflow events. As part of this research effort factors effecting the transport of tsunami borne debris were investigated. The major conditions controlling the transport of debris were identified as: debris size, gradient of the land, flow depth, flow velocity and the surrounding building layout. The conditions governing debris transport must be considered in a site-specific assessment to determine if off-site debris can be transported to a given site.

Debris dispersal caused by a tsunami event can be difficult to quantify because the origin of the debris is not always known. In the case of small and moderate debris types such as: vehicles, wood debris, building components, and trailers the origin of the debris prior to the tsunami event cannot be easily identified as these debris types are very common to all locations within the inundated region. Larger, less common debris types such as shipping containers that are generally stored at container ports and shipping vessels docked at ports and marinas provide a well-defined debris origin. In order to assess the debris dispersal caused by a tsunami event a number of sites in Japan affected by the 2011 event were studied. The inundated regions were investigated for inland dispersion of shipping containers and shipping vessels using post event images obtained from Google Earth. Based on the final location of the identified debris items distances and orientations with respect their origins were calculated.

Due to the fact that the dispersion is assessed using post event images the actual path of the debris cannot be explicitly defined but rather the final position of the debris is used to define an assumed transport path. It is possible that debris was carried further inland during the inflow event and then carried to its final resting position during the outflow event. Four inundated regions (Sendai, Natori,

Kessennuma and Ofunato) of Japan investigated to assess debris transport using post event images from the 2011 tsunami event are identified in Figure 3.

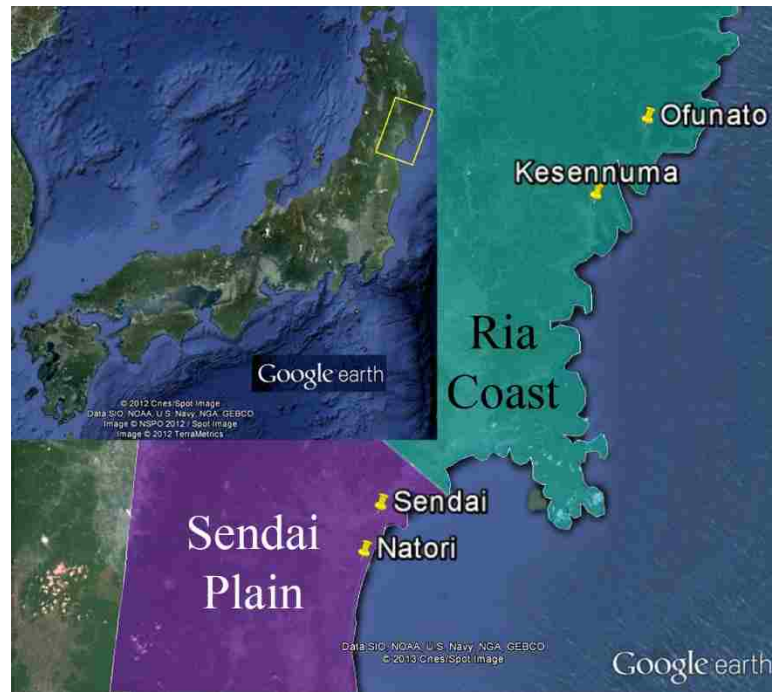


Figure 3: Dispersal regions investigated

Two different topographical regions, Ofunato (ria coast) and Sendai (coastal plain), were investigated for container dispersal. In Sendai two container facilities were investigated. The first (Large Container Facility) was a coastal port that stored 20 ft and 40 ft ISO containers, and the second (Small Container Facility) was an inland site that stored 4 ft ISO containers. The condition of the large and small container facility origins before and after the tsunami event are presented in Figure 4 and Figure 5 respectively. The container facilities location within the image is marked in the purple shaded regions. In order to determine the dispersal for each debris origin Google Earth images taken after the 2011 were used to identify the final location of the debris. Debris identified to have been transported outside of the original debris origin were marked using colored icons. The dispersion of the debris for the small container facility can be seen in Figure 5 where the containers identified from the post event images are indicated with red

icons and the container origin is indicted by a yellow icon. The dispersion of debris for the large container facility can be seen in Figure 6, where the large containers are identified with green icons.



Figure 4: Sendai large container facility before and after



Figure 5: Sendai small container facility before and after



Figure 6: Sendai container facility dispersal

In the case of the small container facility it was found that there was that the average distance of dispersal from the debris origin was 490 ft. (149 m). Other contributing factors to debris dispersion including average inundation height and average building at the debris origin were identified as 22 ft. (6.7 m) and 21 ft. (6.4 m) respectively. For this study all inundation depths used were based on the findings of Takahashi (2011), and the average inundation depth was calculated using the three measured inundation depths closest to the area of interest. The buildings surrounding the small container facility were observed to be steel frame building construction. At the large container facility it was found that the average distance of dispersal from the debris origin was 13661 ft. (4164 m) and the average inundation height and average building at the debris origin were identified as 18.7 ft. (5.7 m) and 21 ft. (6.4 m) respectively. The buildings surrounding the large container facility were steel framed industrial buildings.

At the large container facility the dispersal patterns illustrate that containers from the coastal container origin did not travel inland past the steel framed industrial buildings on the outskirts of the container facility (see Figure 6). At this location the steel frame buildings acted as a barrier preventing the containers from traveling inland due to the fact that these structures were able to withstand the hydraulic forces and were on average higher than the inundation depth at the debris origin. The large average dispersal distance of containers from this site can be attributed to the fact that the surrounding building prevented the majority of the container from traveling inland allowing many of the debris items to be washed out to sea during the outflow. The fact that the containers were washed out to sea produces a much larger dispersion since the containers can move with minimal obstruction in the water along the coast and can be subjected to other forces such as wind and tide. The containers washed out to sea generally produce less of a threat in terms of structural impact as they traveled unobstructed through the sea and eventually ended up beached near the coast.

At the small container facility the dispersal patterns also illustrate (Figure 5) that the majority of the containers did not travel past the steel frame construction. The dispersal pattern shows the containers were able to travel through the undeveloped land in between the debris origin and the steel frame structures but were largely contained by this surrounding buildings at that point. At this location the average inundation depth was just slightly greater than the average building height; however, debris items float with a draft height and in order for a debris item to travel over a structure the draft height must clear the building height which did not occur at this location.

The dispersion of a container facility in Ofunato, an area located in the ria coast region, was also investigated. The condition of the container facility (indicated by

purple shading) before and after the tsunami event is depicted in Figure 7. At the Ofunato container facility the average container dispersion was found to be 1706 ft. (520 m). Other contributing factors to debris dispersion including average inundation height and average building at the debris origin were identified as 30 ft. (9.2 m) and 21 ft. (6.4 m) respectively. The buildings surrounding the small container facility were observed to be mostly wood frames structures. The dispersal patterns (see Figure 8) illustrate that containers were found to travel over a greater region than those in the Sendai region. The greater dispersal of containers at the Ofunato container facility can be attributed to a number of factors including the surrounding building layout and inundation depth at the debris origin. The type of construction surrounding the debris origin was mainly frangible wood-framed construction which collapsed due to the hydraulic loads and the inundation height in this region allowed containers to float over any remaining structures.



Figure 7: Ofunato container facility



Figure 8: Ofunato container facility dispersal

Shipping vessel dispersion was also investigated in the same topographical regions as the container dispersion. For this investigation ports located in Natori (coastal plain) and Kessunnuma (ria coast) were selected as the debris origins under consideration. Both of these areas typically support a large number of shipping vessels. In Natori the average vessel dispersion was found to be 5400 ft. (1646 m). Other contributing factors to debris dispersion including average inundation height and average building at the debris origin were identified as 28 ft. (8.6 m) and 21 ft. (6.4 m) respectively. In Kesennuma the average vessel dispersion was found to be 860 ft. (262 m). Other contributing factors to debris dispersion including average inundation height and average building at the debris origin were identified as 31 ft. (9.6 m) and 21 ft. (6.4 m) respectively. The vessel dispersion for both location are presented in Figure 9 and Figure 10 where the vessels identified inland are indicated using the colored icons.

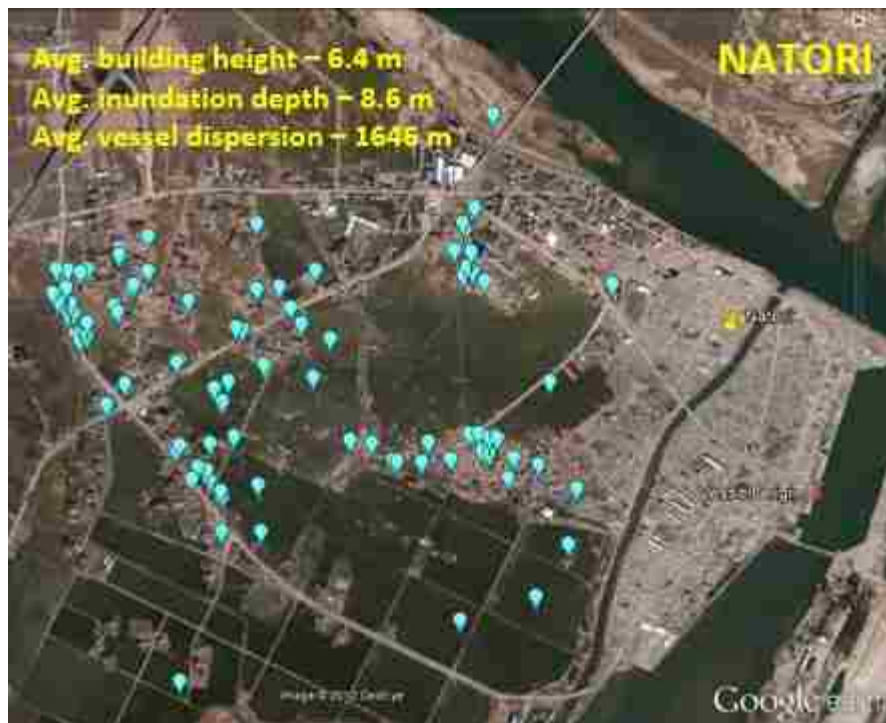


Figure 9: Natori vessel dispersion



Figure 10: Kesennuma vessel dispersion

The inundation depth was greater than the building height in both Natori and Kesennuma. This allowed the vessels to move inland with obstruction from the built

surroundings. In Natori, vessels were found at a greater distance inland compared to Kessennuma. This can be attributed to the planar topography which made it easier for the boats to travel inland. In addition, because of the mildly sloping topography the rundown velocities were likely low, which made it easier for vessels to remain inland. In Kessennuma, the increased slope of the land helped prevent the boats from continuing inland, or perhaps they were subjected to larger rundown velocities, so they remained closer to the coast.

Post event dispersal of debris in inundated regions of Japan verified that the gradient of the land and surrounding building layout effects the transport of debris. In general it was determined that building construction and spacing play an important role in debris transport. Generally, in areas where residential light framed construction is common and the inundation height is a story or more it can be assumed that the buildings will collapse (FEMA 2012). In industrial areas where steel and concrete construction is typical, the buildings are generally able to withstand the hydrodynamic forces generated by the tsunami and can therefore act as barriers to debris transport, especially if the flow depth is lower than the height of the building. The fact that these buildings can act as a barrier to stop debris transport also means they are subject to debris impact damage, which may potentially cause the building to collapse and release additional debris. Also the effect of the topography was apparent in terms of mild sloping topography allowing debris to travel inland and also remaining there more easily during rundown. The effect of debris size, flow depth, flow velocity as well as flow direction will be evaluated in the subsequent section.

2.3.3. Debris Impact Hazard Region

For the purpose of site assessment it is helpful to create a quantitative measure of the debris concentration and delivery potential for a building site. The debris impact

hazard region presented in this section was developed based on the dispersion of debris during the Tohoku event and adopted by ASCE 7-16. The impact hazard region defines a probable dispersion region for large debris items such as shipping containers, barges, and shipping vessels. If a building site lies within the debris impact hazard region the structure must be designed to withstand impact loads from these large debris items.

Using the Google Earth satellite images for locations in Japan for which the debris transport of the shipping container and shipping vessels was identified a probable dispersion region common to all locations was investigated. Based on the observations from the investigated regions it was found that debris items were transported during the inflow and outflow events, which is evident from debris identified further inland from the debris site and closer to the coast. This is illustrated in Figure 11, for an inland small shipping container storage site in Sendai, Japan. Based on the final location of the containers it is assumed that a large majority of the containers were transported during the inflow event however some containers appear to have been carried towards the shore line during the outflow event.



Figure 11: Inflow and outflow debris transport

Another assumption used to establish the debris impact hazard region is that the debris items will travel along the same path as the flow. Flow directionality at a debris site can be determined using a site-specific analysis or approximated based on guidance for tsunami flow provided by ASCE 7-16. In cases where site-specific data is not available the assumed flow direction for a given debris site can be approximated by establishing the coast normal line. The coast normal line is determined by averaging the shore line over 500 ft. (150 m) to each side of the debris source center. Flow directionality is then determined by drawing a line that is perpendicular to the normalized coast line and passes through the debris source center. Due to variations in the onshore flow conditions the flow can be assumed to vary ± 22.5 degrees from the assumed flow direction. Based on this variation in flow the debris is also assumed to disperse ± 22.5 degrees from coast normal. This assumption on flow direction is used to establish the vertex angle of the inflow and outflow cone for the debris hazard zone.

To capture the spread of debris during the inflow event an inflow cone is created where the vertex is located at the debris source center. The 45 degree vertex angle of this cone is based on the variation in assumed flow direction of +/- 22.5 degrees. The cone is oriented with the assumed flow direction running along the center for the cone. The next step was to determine at what distance the inflow cone should be curtailed. To do this different threshold values for debris concentrations (i.e., 100%, 50%, 25%, 10%, 1%, etc.) within the inflow cone were investigated. A debris concentration is determined by dividing the total surface area of debris (number of debris items multiplied by the planar area of the debris type) by an area of inundated land. Four different debris concentrations investigated for inflow region of the small container site in Sendai, Japan are indicted in Figure 12. Based on the observations from all the regions examined, it was determined that a 2% debris concentration within the inflow region captured the spread of debris inland. This 2% concentration can also simply be computed by multiplying the total surface area of debris by 50. The inflow region established using the 45 degree cone curtailed by the 2% debris concentration is indicted by the white shaded region in Figure 12.



Figure 12: Inflow region development

As previously discussed debris can be transported both during the inflow and outflow event. To account for drawdown after inundation a return dispersal spread of +/- 22.5-degrees is proposed from the edge of the dispersal region. Essentially the outflow cone created to capture the debris dispersion during drawdown is the inverse of the inflow cone centered at the intersection of the coast normal line and the 2% debris concentration boundary. The outflow cone is extended to the shoreline as opposed to curtailing the area based on a debris concentration. The application of the outflow cone for the small container site in Sendai, Japan is depicted in Figure 13 as the yellow shaded region.

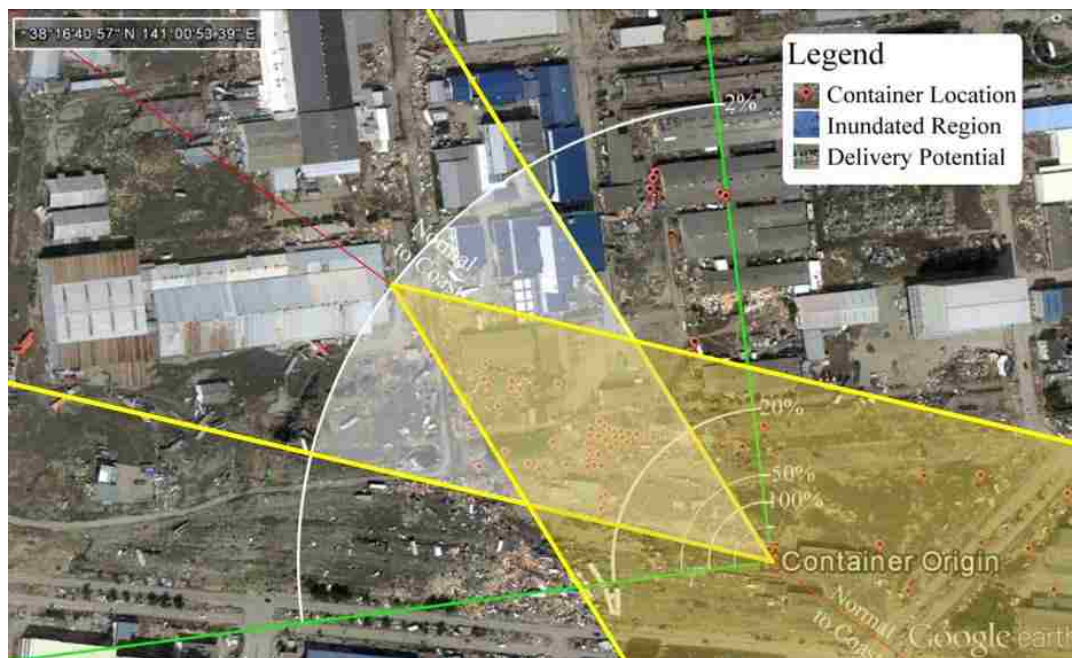


Figure 13: Outflow region development

A building site within the shaded regions, indicated by the inflow and outflow cones, must be designed for impact of the particular large debris item stored debris origin, in this case shipping containers. For this particular location it was found that 90% of the debris was captured by the debris hazard zone. To capture 100% of the debris the vertex of the inflow cone must be increased to 90 degrees (indicted by the green lines in Figure 13), which would result in a large increase in number of

buildings that must be designed to withstand the extreme levels of demand that can be generated by large debris impacts. For this reason the 45 degree cone for both inflow and outflow is utilized to define the impact hazard region.

The debris hazard region was applied to other locations in Japan where large debris dispersion was observed. Figure 14 illustrates the application of the debris hazard region to capture shipping vessel dispersion in Natori, Japan. The blue shaded region indicates the inundated area of land for this region (Haraguchi, 2012). Shipping vessels identified inland using post event satellite images are indicated using light blue markers. The boundaries for the inflow and outflow cones used to establish the debris hazard region are also indicated and labeled. Again, at this location 90% of the dispersed debris was found to lay within the debris impact hazard region.

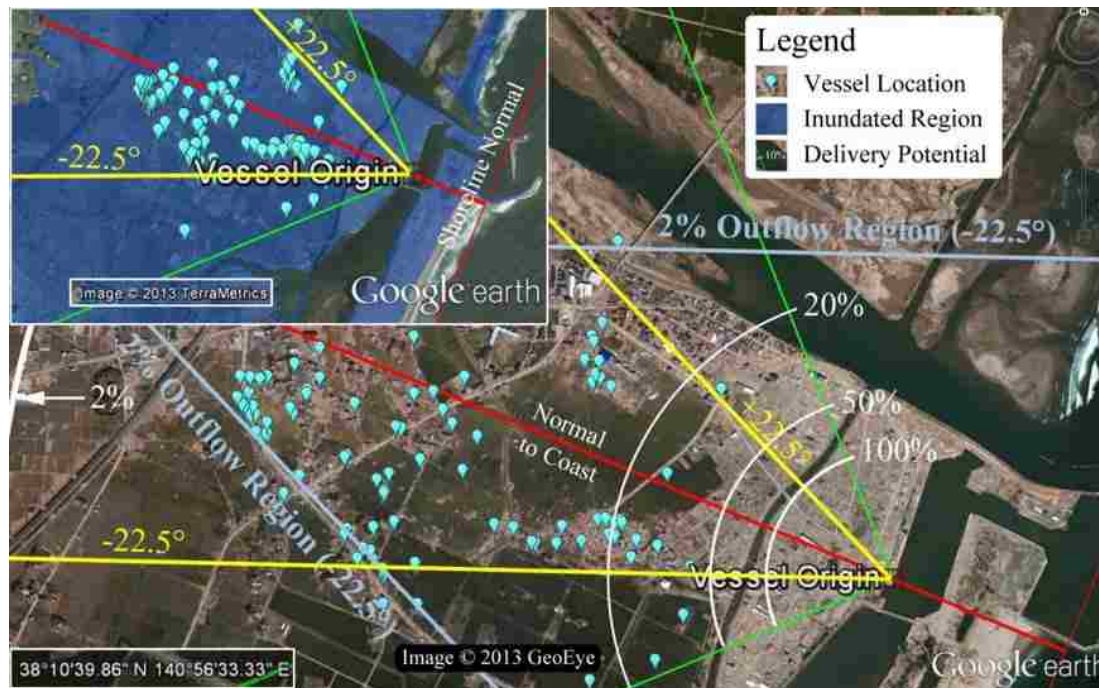


Figure 14: Debris impact hazard region applied to shipping vessel dispersion

Based on the study of debris transport generated by the Tohoku event the impact hazard region was established and adopted by ASCE 7. Figure 15 illustrates the

concept of the impact hazard region. Any structure within the impact hazard region, indicated by the hatching, will be designed to withstand large debris impact caused by that particular debris item. The procedure established to construct the debris hazard region for tsunami prone regions is outlined and applied to a container storage facility in Hilo, Hawaii.

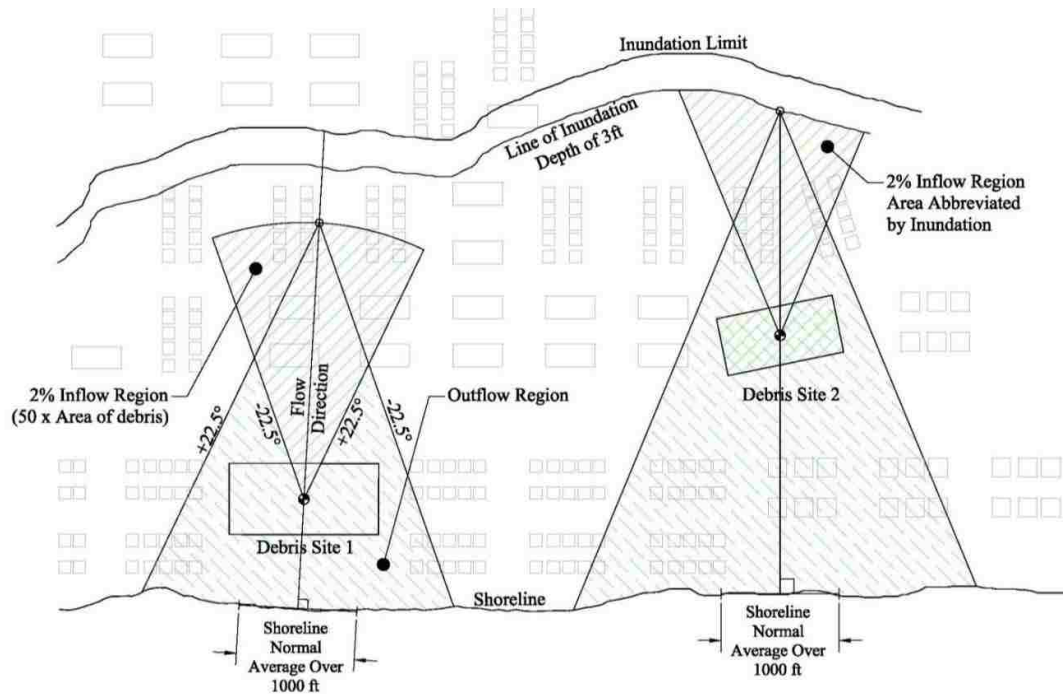


Figure 15: Debris impact hazard region

The first step in defining the impact hazard region is to determine the expected inundation zone. Only large debris sources located within the inundation region will be considered as a potential debris source. The inundation zone for a particular geographical region can be determined from the tsunami design zone data that can be downloaded from ASCE. The tsunami design zone obtained from the downloadable KMZ (keyhole markup language zipped) data is shown for the region of Hilo, Hawaii in Figure 16. The yellow line in this figure indicates the inundation limit and the purple shaded area of land indicated the inundation zone.



Figure 16: Tsunami design zone for Hilo, Hawaii

The next step is to identify potential large debris sites within the inundated region and to determine the number of debris items that are typically stored at each site. This can be done using satellite images of the region or a field investigation of the area. The results can be used to calculate a debris concentration for the debris type (i.e., containers, shipping vessels, etc...). In tsunami prone areas, debris origins with higher debris concentration will have a higher chance of dispersing debris and therefore a higher delivery potential across the inundated region. For the location of Hilo, Hawaii a shipping container storage facility was located within the inundated region and is marked with a red outline in Figure 17.



Figure 17: Debris source Hilo, Hawaii

Satellite images were used to approximate the number of shipping containers that can be stored at this facility. It was approximated that this facility can store 500 20 ft. (6 m) containers and 1,400 40 ft. (12 m) containers. The debris estimates are then used to establish the inflow cone for the debris hazard zone. The inflow cone is constructed as 45 degree cone with an area equal to 50 times the surface area of debris, where the vertex of the cone is located at the debris source center. Next, the outflow cone is established by inverting the inflow cone and extending the cone until the shore line is reached. The debris hazard zone constructed for the region of Hilo, Hawaii is illustrated in Figure 18.

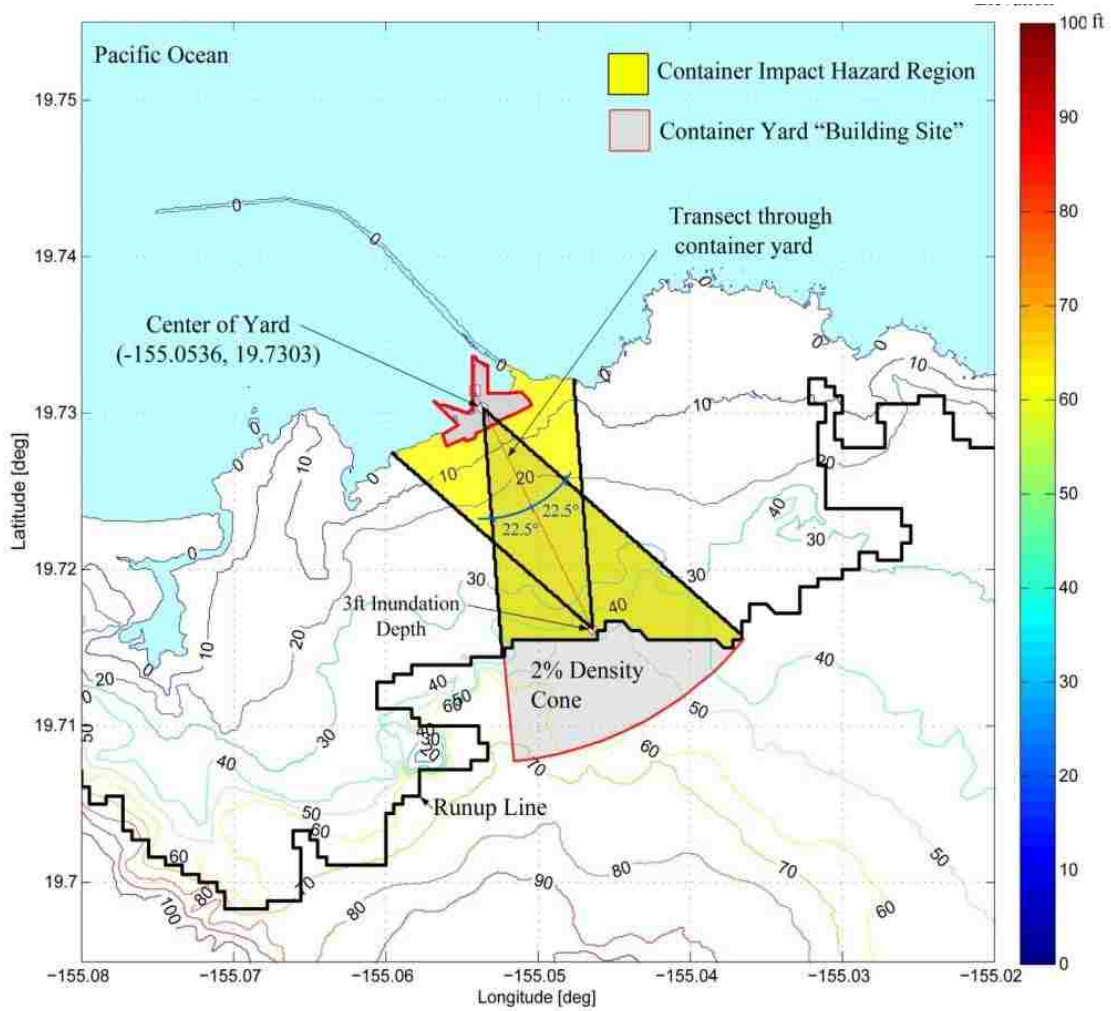


Figure 18: Debris impact hazard zone Hilo, Hawaii

The inflow cone for the container facility in this example extends past the inundation limit. In cases like this the inflow zone will be curtailed by the location of inundation limit as debris cannot be transported outside of the inundated zone. Figure 18 shows the portion of the inflow zone extending past the inundation limit as the grey shaded region. The yellow shaded region which is now curtailed by the inundation limit represents the debris impact hazard region for location. All structures within this region must be designed to withstand impact loads from shipping containers. It should also be noted that debris items are assumed to be unable to float in inundation depths of 3 ft. (1 m) or less, which is due to the interaction that will occur between the ground and the debris item. The design engineering can apply

this concept and curtail the inflow zone along at a 3 ft. (1 m) inundation depth as opposed to inundation limit where the inundation depth is assumed to be 0 ft.

2.3.4. Contour Mapping

Contour maps can be generated for tsunami prone regions which illustrate how the inundation depth, water velocity and impact force for a given debris item can vary across the inundated region. The motivation behind the development of the contour mapping is to provide engineers with design tools for tsunami prone regions. Contour maps for inundation height, water velocity and impact force due to an empty shipping container were generated for the tsunami prone region of Hilo, Hawaii and are illustrated in Figure 19, Figure 20 and Figure 21. The contour maps also show the boundaries of the impact hazard zone for this location.

The inundation height and water velocity used in the contour mapping were calculated using the energy grade line method. The impact force contour map does not include any force effects from the hydrodynamic loads. The contour maps are particularly useful in urban planning as design engineers can approximate the demands on the system based on the proposed location of a building site. Even with the contour mapping, once the building site is selected the structure must still be designed according to the tsunami design guidelines outlined in ASCE 7.

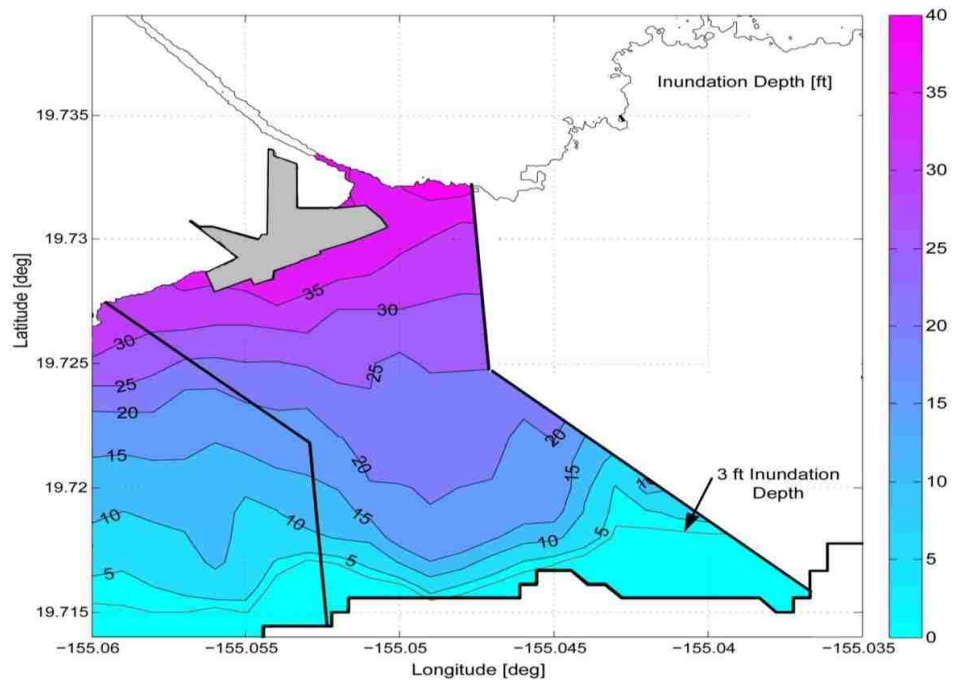


Figure 19: Inundation depth mapping

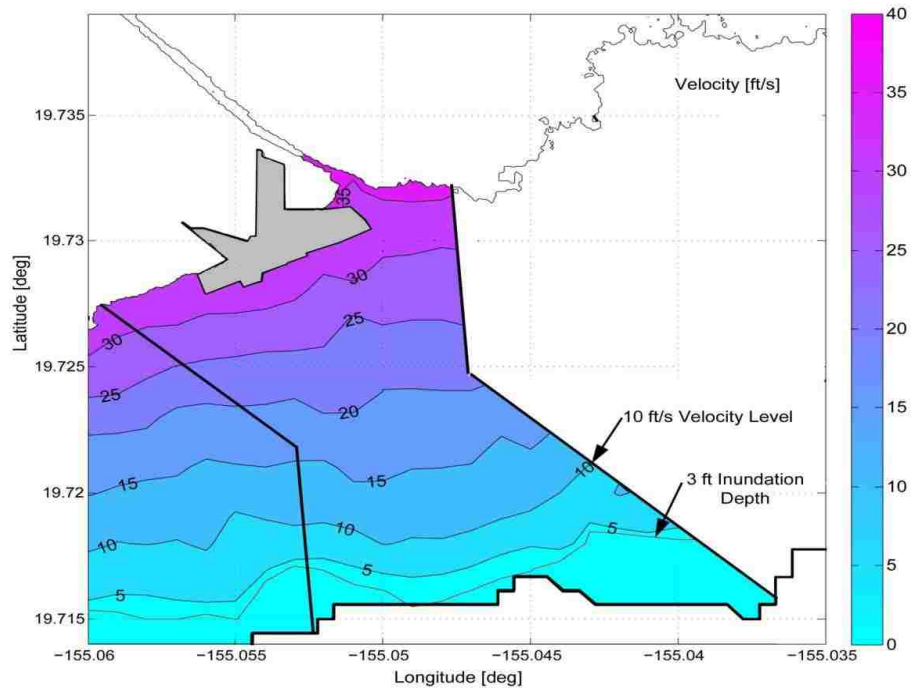


Figure 20: Flow velocity mapping

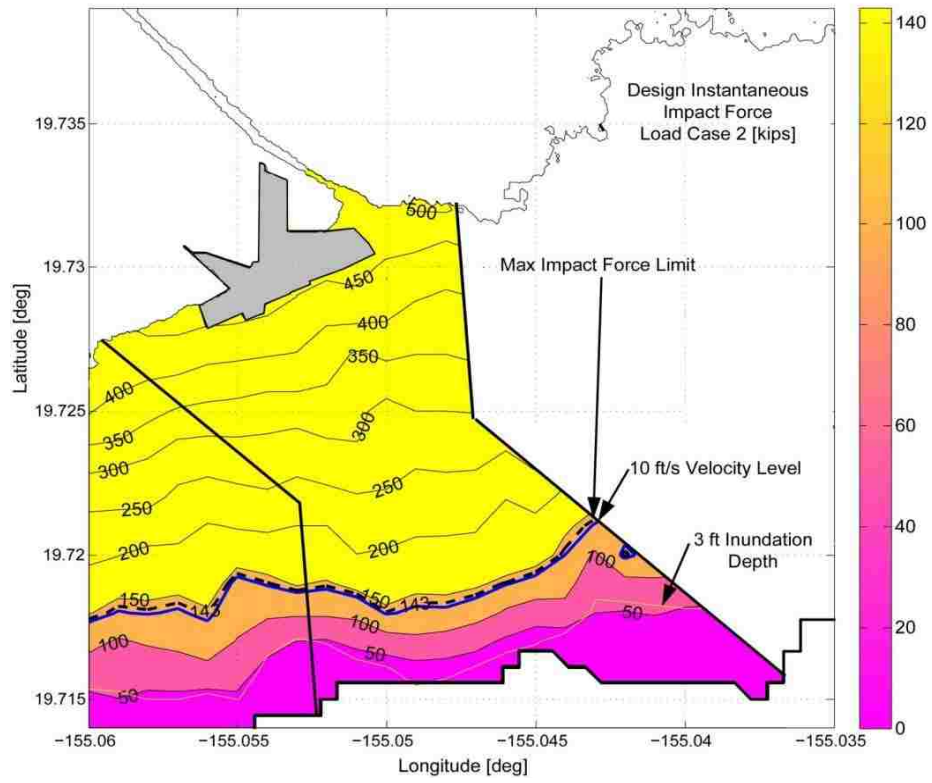


Figure 21: Impact force mapping

2.4. Modified Energy Grade Line Analysis

The energy grade line method is a linear transect analysis developed and validated by Kriebel et al. (2016) and presented in ASCE 7-16, to produce conservative design flow parameters. The analysis method provides a simplified approach to estimate the water velocity and inundation depth at a site. The energy grade line analysis method will be required to determine the maximum flow depth and flow velocity for all building sites that lie within the tsunami design zone. In addition to the energy grade line analysis a site-specific inundation analysis will also be required for buildings in Tsunami building risk category IV.

The energy grade line analysis provides a simplified method to compute fluid flow properties that would otherwise require sophisticated numerical modeling. The method was developed with the intention to produce statically conservative results, at least for the maximum momentum flux that is used for the hydraulic loading (ASCE 7-16). Initial tuning of the method was carried out by Wiebe (2013) using FUNWAVE-TVD (Shi et al. 2011). The EGL analysis was also applied to geographical regions of Japan and comparisons with field measurements during the Tohoku tsunami indicated that the method provided conservative values for the sites considered (Carden et al., 2015).

Given that the velocity and inundation height are used for structural design purposes and the EGL has not yet been widely validated within the archival literature, a detailed comparison between results of the EGL and site-specific analysis are made to contribute to the continuing evolution of the EGL method. The two methods are compared for multiple sites in Hilo, Hawaii, a tsunami prone location in the United States. The performance of the EGL analysis as compared to the site-specific analysis results are investigated as well as the EGL methods sensitivity to digital elevation model data.

2.4.1. Performance of the Energy Grade Line Analysis

To establish the performance of the energy grade line analysis, results produced utilizing this method are compared to a site-specific analysis for three site locations in Hilo, Hawaii. Three different site locations (site A, site B and site C) in the inundated region, identified in Figure 22, are analyzed. The site-specific inundation analysis was carried out with the tsunami model MOST (Method of Splitting Tsunamis) (Titov and Gonzalez 1997; Titov and Synolakis 1998). The results of the site-specific analysis for the Hilo, Hawaii location were provided a collaborative researcher (Wei, 2015). The energy grade line analysis was performed following the procedures outline in ASCE 7-16.

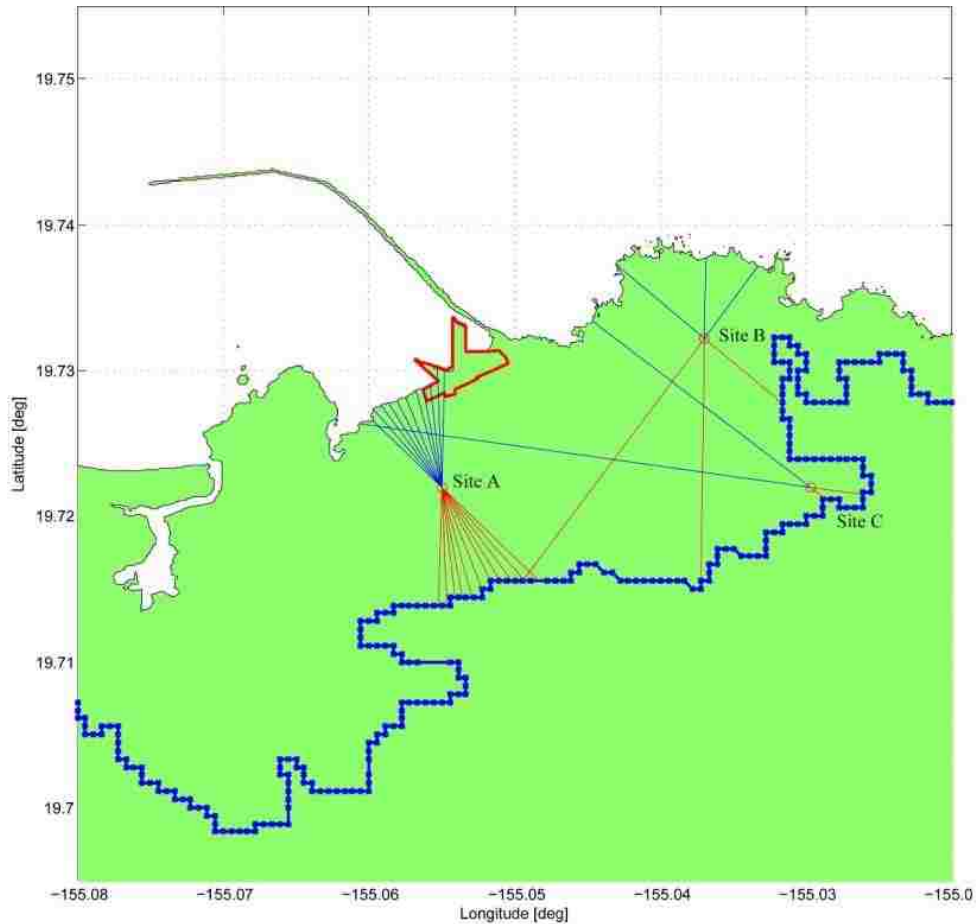


Figure 22: Site and Transect Locations

For each site a number of different transects are analyzed using the energy grade line method. The reason for this is that for each site transect the flow directionality can be assumed to vary +/- 22.5 degrees. To account for the potential variation in flow directionality, the transect within the +/- 22.5 degree cone that produces the maximum value for velocity and inundation depth at the site is selected. Results for three transects at each site are presented to show the potential variability in flow characteristics for a given location. The velocity and inundation height determined using the EGL method for each transect are shown in Table 2. The maximum velocity and inundation depth for each site (highlighted in yellow) is compared with the velocity and inundation depth determined using the site-specific analysis (see Table 2).

Site	Transect	Inundation Depth [ft]		Velocity [ft/s]	
		EGL	Site Specific	EGL	Site Specific
A	(-) 22.5	20.31	25.27	19.61	24.89
A	Center	18.88		17.97	
A	(+) 22.5	11.83		13.86	
B	1	2.03	8.61	2.45	9.60
B	2	1.36		1.93	
B	3	2.66		3.38	
C	1	4.12	25.19	7.97	37.12
C	2	22.07		23.14	
C	3	26.63		25.74	

The results of the EGL method show that a difference in transect path and topography can result in considerable variation in the inundation depth and velocity at a site. The comparison of the two methods also show that the EGL method under predicted the velocity for every site transect and the inundation depth for every transect except for one (C3). After examining the discrepancies between the EGL and site-specific methods part of the underestimation may be attributed to the

difference in vertical accuracy between the digital elevation models used in the EGL analysis and site-specific method. Another potential reason for the underestimation may be attributed to the fact that the velocity and inundation height at the run up is assumed to be zero in the EGL analysis. However, the runup elevation (which is determined based on site-specific modeling) provided by ASCE 7 does not always correspond to the same topographical elevation at the inundation limit using the digital elevation model data provided for the energy grade line analysis. This can result in a non-zero inundation height at the inundation limit when applying the EGL method based on the discrepancy between the runup elevation provided by the site-specific model and the corresponding topographical elevation based on the digital elevation model. This height of water at the inundation limit is not representative of actual field conditions and it is still assumed that in an actual event the height of water at this location would be equal to zero.

In many cases the DEM data obtained for the EGL analysis may differ from the DEM data that was used for runup modeling. For example, at the site in Hilo the topographic DEM dataset used for the ASCE inundation simulations was obtained from the National Geospatial-Intelligence Agency (NGA) Hawaii Interferometric Synthetic Aperture Radar (IfSAR). The IfSAR dataset used for the site-specific analysis has an increased vertical accuracy compared to the USGS 1/3-arc-sec National Elevation Dataset (NED) available to the general public (through the NCEI) for use with the EGL method. Love et al. (2011) reported that the IfSAR data has a vertical accuracy of 6.6 ft. (2 m) or better in areas of unobstructed ground which is much greater than then USGS NED 1/3-arc-sec data which may have as poor as 30 ft. to 49 ft. (7 to 15 m) vertical accuracy.

The digital elevation model for Hilo, Hawaii created using the IfSAR and USGS NED topography are presented in Figure 23 and Figure 24 respectively. Comparison of

Figure 23 and Figure 24 shows that the DEM generated using the IfSAR topography provides a greater level of vertical accuracy than the DEM generated using the USGS NED topography. The elevation discrepancy (in feet) between the two DEMs are presented in Figure 24. As illustrated the majority of the elevation discrepancies for this particular location occur outside of the tsunami design zone. Therefore, although there is a difference in vertical accuracy between the two datasets the effect on the EGL method results will be minimal.

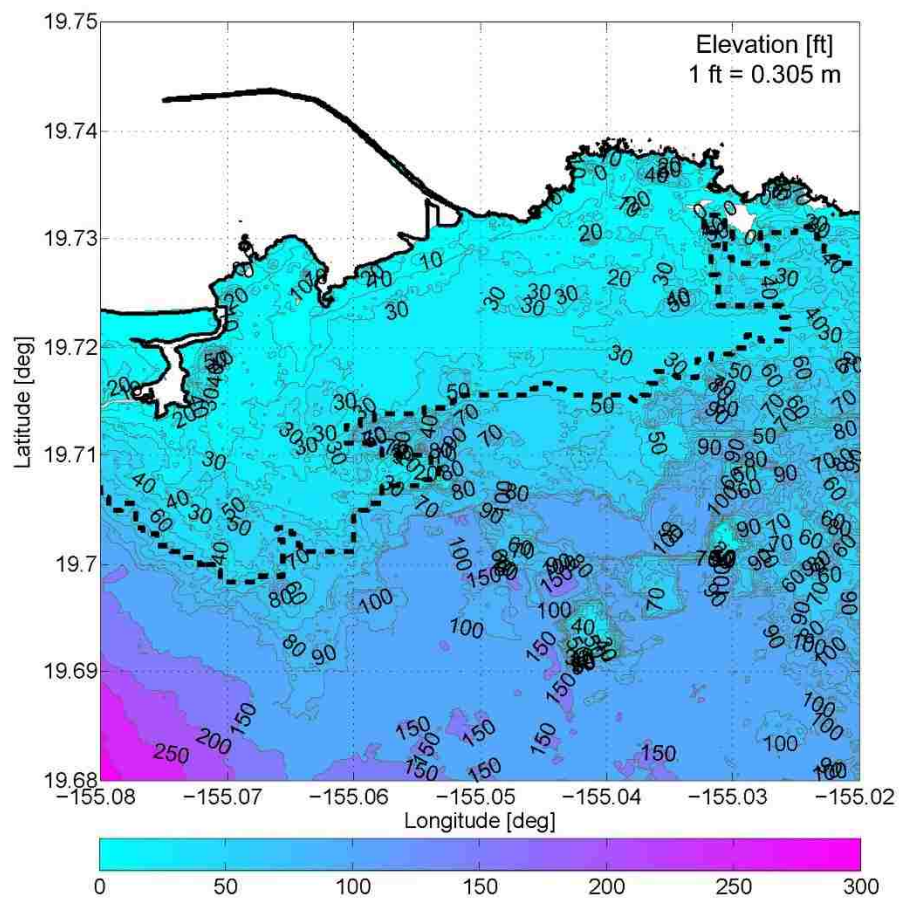


Figure 23: Digital elevation model using IfSAR topography

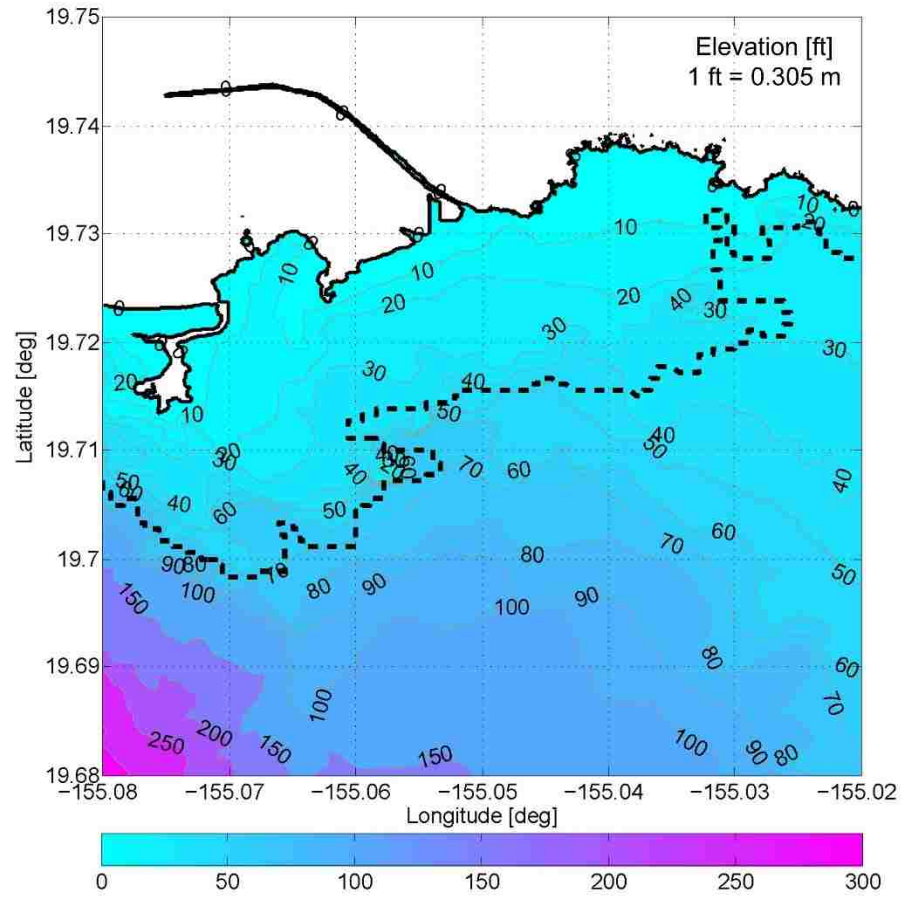


Figure 24: Digital elevation model using USGS NED topography

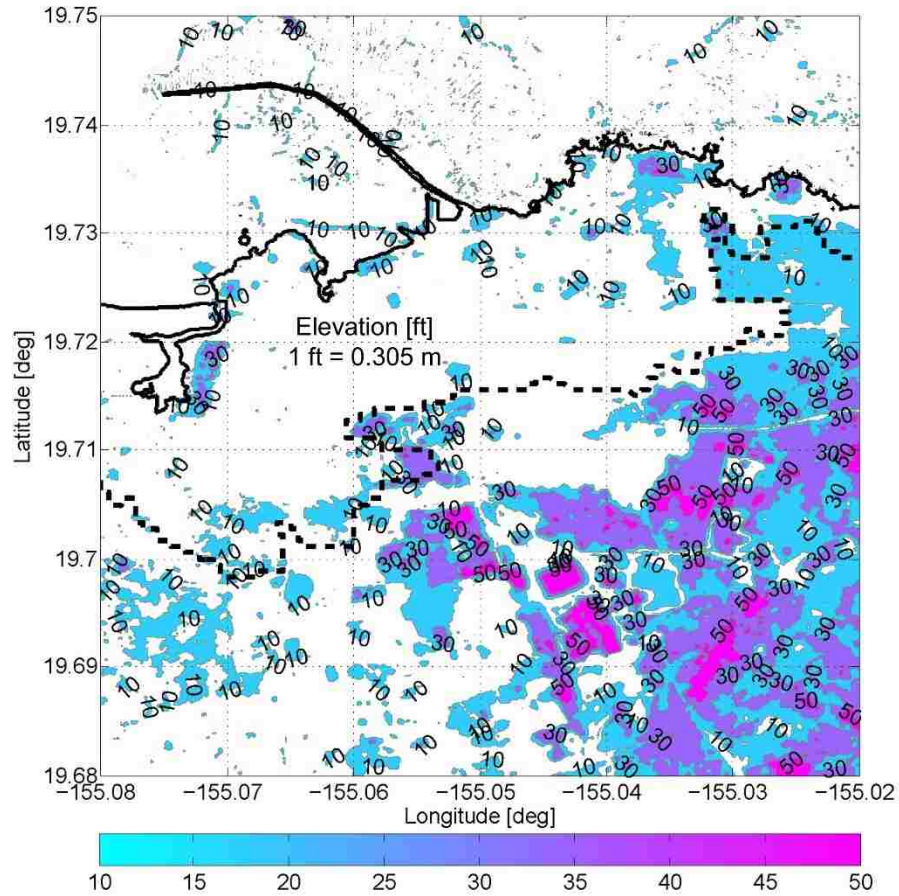


Figure 25: Elevation difference in feet NGA IfSAR and USGS NED DEM

Another potential reason for the underestimation of the EGL analysis method compared to the site-specific analysis can be attributed to potential mismatches between the DEM elevation at the inundation limit and the ASCE runup elevation. The elevation for a given latitude and longitude for a particular DEM data set may not match the runup elevation provided by ASCE-7 for that same point. The mismatch between the DEM and runup elevation can be attributed to the way in which the runup data is obtained. Essentially the two-dimensional runup modeling uses grids in the horizontal x-y plane for which each cell (element) is given a constant elevation, which is the average elevation over the cell. In the case of the ASCE runup simulations a grid size of 2 arc sec (approximately 197 ft. (60 m.)) was used. If the DEM data are at 1/3 arc sec (approximately 33 ft. (10 m)), as is the

case for the USGS NED data, then there are 36 DEM cells per runup element. Therefore, it is possible for the runup elevation (sum of the element elevation and the calculated water depth) to be either larger or smaller than the DEM elevation for a given point.

This concept is illustrated in Figure 26, where a hypothetical approximate ground profile based on the DEM data is compared to the approximate ground profile from a site-specific runup model. The DEM ground profile is indicated in black where the circular markers indicate the DEM data points and the line connecting the markers represents the interpolated ground profile. The approximate ground profile based on the average elevation over each grid cell used in the site-specific model is indicated in blue. The difference in ground profile for a x,y data point as approximated by the site-specific runup model and the DEM data can clearly be seen in Figure 26.

The DEM ground elevation of a point corresponding to the last 'wet' element can be either below the calculated water elevation or above it. This mismatch can still occur even if the same data and same grid spacing were to be used. The site-specific modeling software can only calculate a finite water depth, therefore it will never calculate a water elevation that will equal the elevation of the element. In the case of ASCE runup, the site-specific model used considers the cell "dry" when the depth of water in that cell is less than 0.33 ft. (0.1 m).

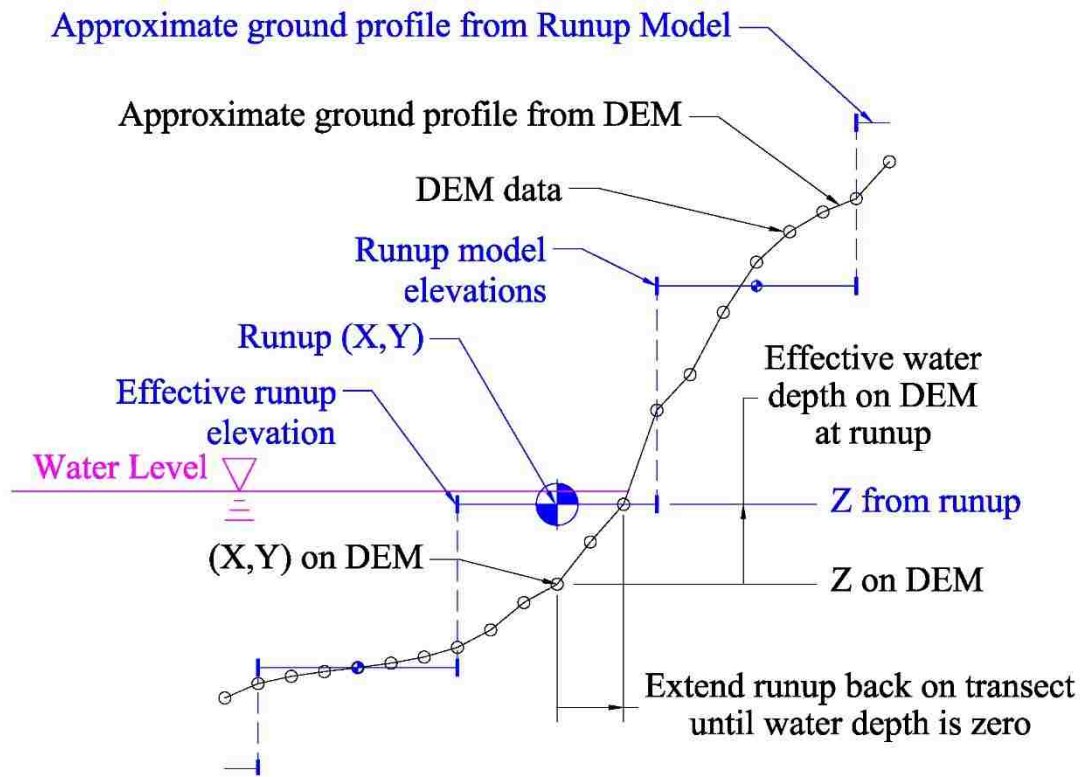


Figure 26: Discrepancy between DEM data and runup model

In general, when the DEM elevation is found to be below the runup elevation at the inundation limit the energy grade line method will under predict the velocity and inundation depth at a building site compared to the site-specific results. As mentioned previously the EGL method was developed on the assumption that the velocity and inundation depth are essentially zero at the inundation limit. However, due to the potential mismatch between the DEM and ASCE runup elevation it is possible to have a nonzero inundation height at the inundation limit when performing the energy grade line analysis. When applying the energy grade line method the inundation depth at the inundation limit should be obtained by subtracting the ASCE runup elevation from the DEM ground elevation as opposed to assuming this value to be zero at the ASCE defined inundation limit.

2.4.2. Modifications to the Energy Grade Line Analysis Method

Modifications to the energy grade line analysis method were investigated based on the potential for the inundation depth at the inundation limit to be a nonzero value. The goal of the modification to the EGL method is to produce results that are closer to the inundation depths and velocities approximated by the site-specific analysis. The energy grade line method, modified energy grade line method and site-specific analysis was performed for Hilo, Hawaii, a tsunami prone region of the United States. The inundation depth at the inundation limit to be utilized in the modification of the EGL method was obtained by subtracting the ASCE runup elevation from the DEM ground elevation at the inundation limit. Two different approaches to account for the nonzero inundation depth at the inundation limit were investigated.

The first approach investigated involves modifying the EGL assumption that the inundation depth is zero at the inundation limit. Instead of setting the inundation depth at the inundation limit to zero during the initial EGL step, the inundation depth will be set as the value obtained by subtracting the ASCE runup elevation from the DEM ground elevation. The EGL analysis is then performed following the same procedure outlined in ASCE 7-16 from the inundation limit to the site. This modified approach will be referred to as the adjusted inundation height (adjusted h) EGL approach. The initial velocity at the inundation limit cannot be adjusted velocity information will not be provided by the ASCE runup data and is therefore is assumed to be zero.

The adjusted inundation EGL approach was applied to a number of transects identified in Figure 22. The results of the adjusted inundation EGL approach were then compared to the traditional energy grade line method and the site-specific analysis. The results for the site A normal transect are depicted in Figure 27 and Figure 28. The results show how the inundation depth and velocity vary along the

length of the coast normal transect for all three methods used. It can be seen that the adjusted EGL approach provides a better approximation than the EGL method compared to the site-specific results for both velocity and inundation depth at the site (indicated by location $x=0$ ft); however, the velocity is still under predicted and the adjusted EGL method is now over predicting the inundation depth.

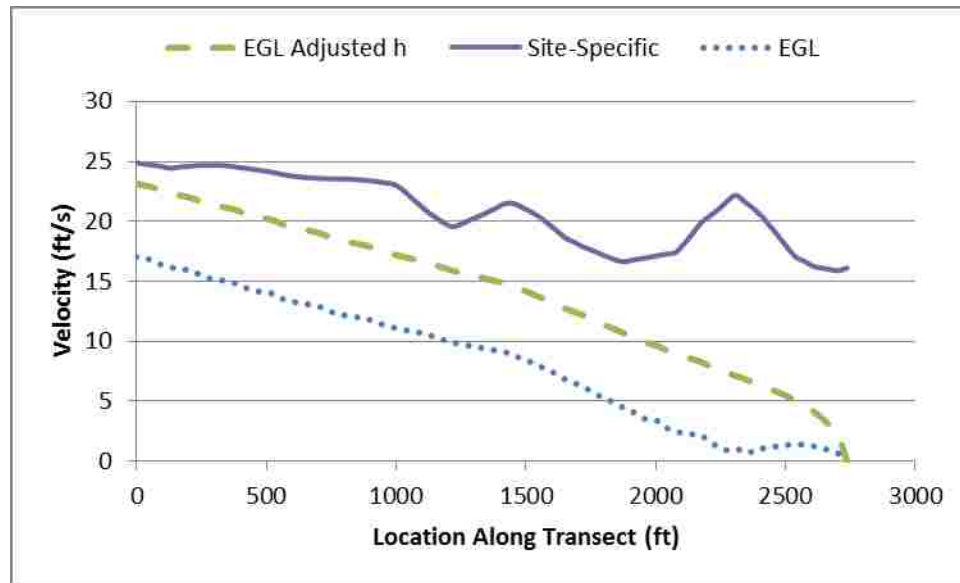


Figure 27: Adjusted inundation Site A normal transect EGL inundation depth comparison

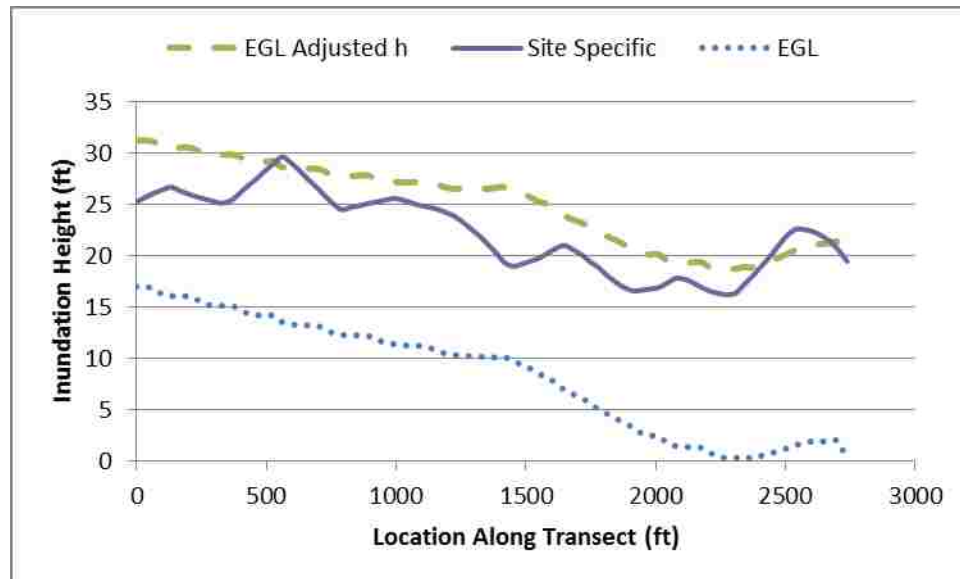


Figure 28: Adjusted inundation Site A normal transect EGL velocity comparison

The second modification to the energy grade line method investigated involves extending the length of the EGL transect past the runup to a point where the DEM ground elevation is equal to the ASCE runup elevation at the inundation limit. The extension of the transect past the inundation line for each flow transect analyzed is depicted in Figure 29. At this new end point along the extended transect the velocity and inundation depth are assumed to be zero. The EGL analysis is then performed following the same procedure, outlined in ASCE 7-16, from the extended EGL end point to the site. This modified approach will be referred to as the extended EGL approach.

The extended EGL approach was applied to the transects identified in Figure 29. The results of the extended EGL approach were then compared to the traditional energy grade line method and the site-specific analysis. The results for the site A normal transect are shown in Figure 30 and Figure 31, where the variation of the inundation depth and velocity along the site transect can be seen. Comparing these three approaches it was found that the extended EGL provides better approximations to the site-specific method for both the velocity and inundation depth at the site (indicated by location $x=0$ ft) than the traditional EGL approach. For this particular transect the extended energy grade line method provides nearly the same site velocity as the site-specific analysis and over predicts the inundation depth.

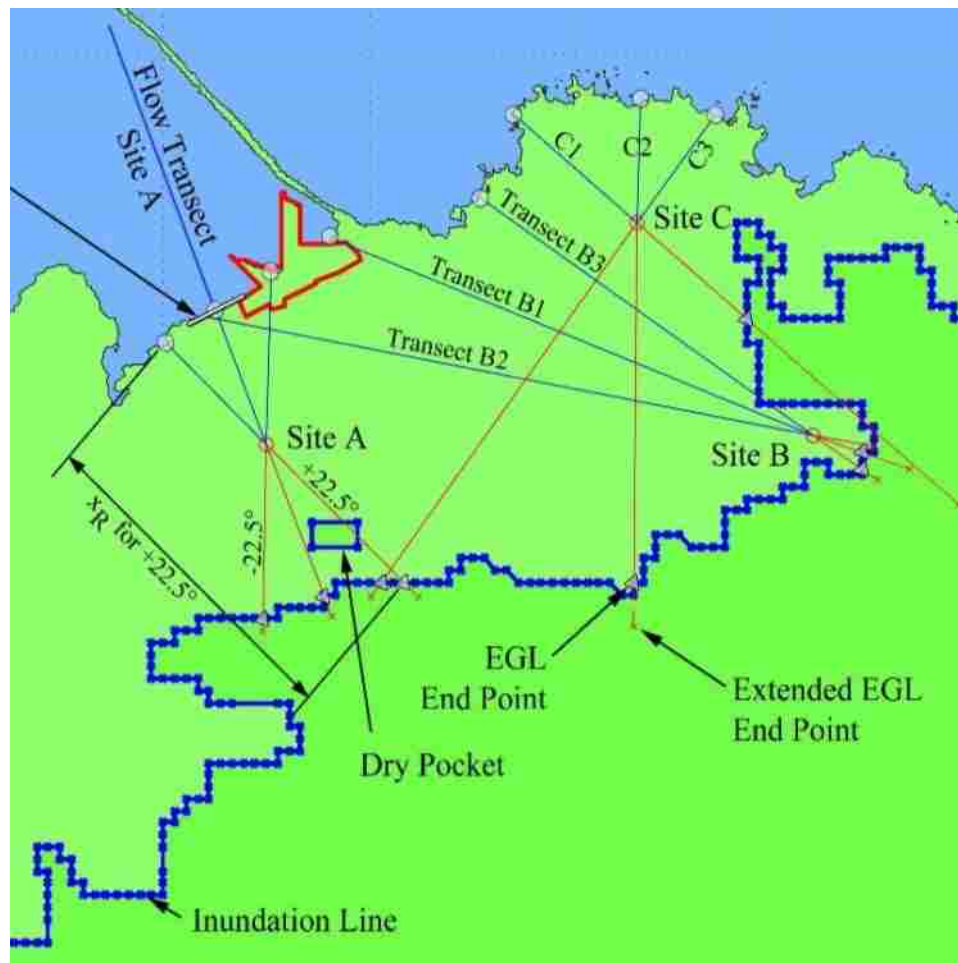


Figure 29: Extended energy grade line transects

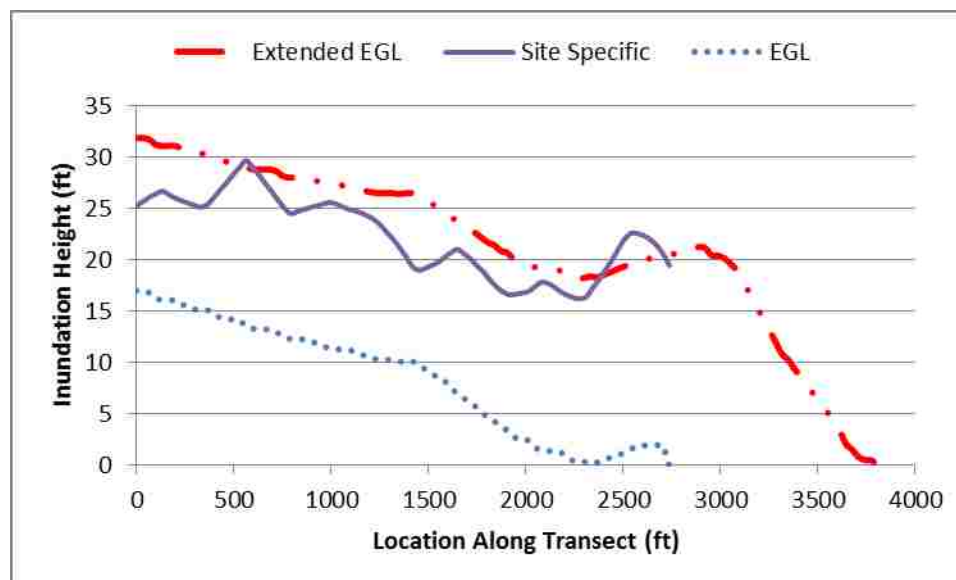


Figure 30: Extended EGL Site A normal transect inundation depth comparison

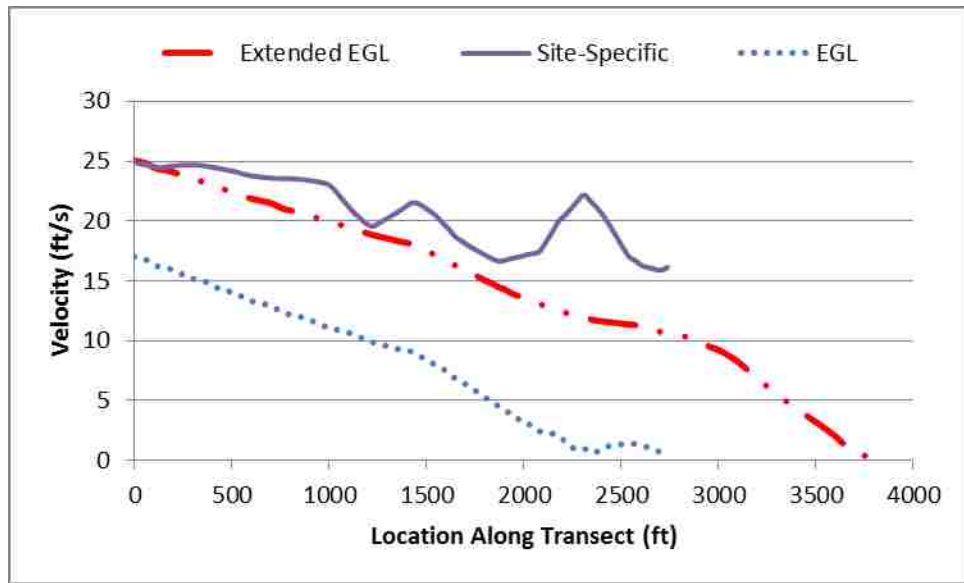


Figure 31: Extended EGL Site A normal transect velocity comparison

The adjusted inundation EGL and extended EGL approach for the site A normal transect are compared to the site-specific analysis in Figure 32 and Figure 33. It should be noted that the EGL method in all approaches was calculated using a different DEM than the site-specific analysis and therefore will introduce some error that cannot be accounted for by modifying the way in which the energy grade line method is applied. The results from site A normal transect example show that both modified approaches perform better than the traditional energy grade line method for approximating inundation depth and velocity at the site compared to the site-specific results. Even though the two modified EGL methods produce almost identical values for the inundation depth at the site, the extended EGL method provides closer approximations to the site-specific velocity at the building site compared to the adjusted inundation approach.

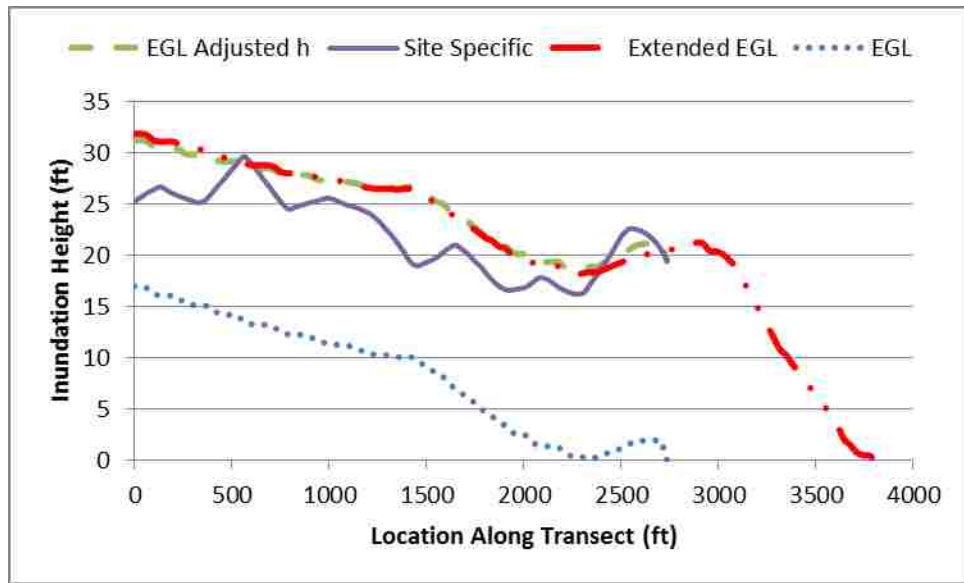


Figure 32: Comparison of transect inundation results

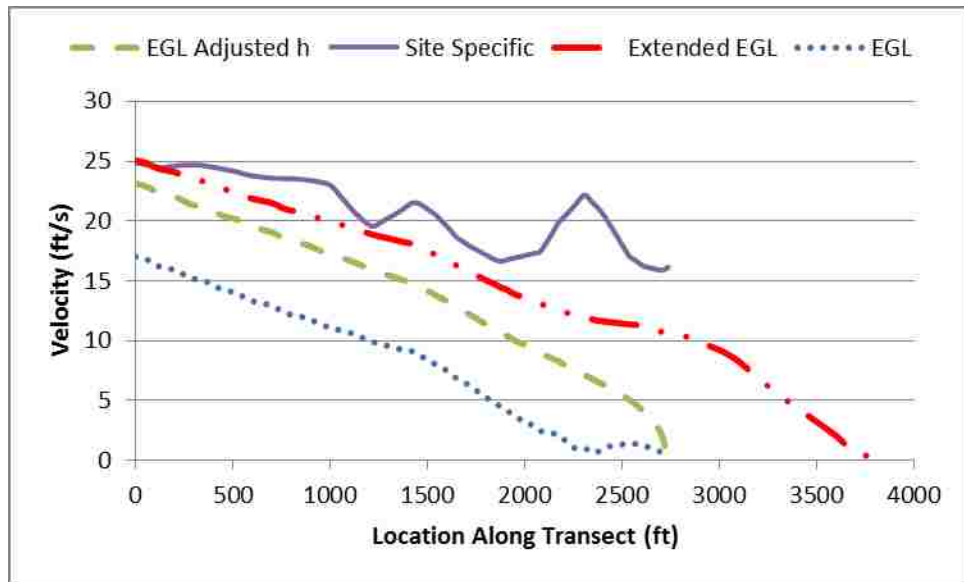


Figure 33: Comparison of Site A normal transect velocity results

Based on the success of the investigation of the extended energy grade line at site A the energy grade line and the extended energy grade line method were applied to the three site locations illustrated in Figure 22. Due to the ground topography and calculated water depth at the runup the extension of the EGL transect can in some cases be very long (see transect C1) or very short (see transect B2). By extending the length of the transects the initial ground elevation used in the

extended EGL method is higher than elevation at the inundation limit, resulting in the observed increase in the velocity and inundation depth at the site.

The results of the EGL and extended EGL approaches are compared for the transects at site A, B and C in Table 3. The highlighted cells in Table 3 represent the maximum calculated velocity and inundation depth using the EGL and extended EGL approach for each site. The maximum values are compared directly with the site-specific values. The extended EGL method resulted in an increased velocity and inundation depth at the site compared to the traditional EGL analysis. As can be seen in Table 3, the extended EGL results in a conservative estimate of the inundation depth at all three sites compared to the site-specific results. While the corresponding extended EGL velocities also increased significantly at the site compared to the EGL results, they are still under predicting the site-specific results, in this case by an average of 16%. Based on the results of this investigation the extended EGL method is recommended over the traditional and adjusted EGL method in order to produce inundation depths and velocities at the building site that are closer approximations to the site-specific analysis results.

Site	Transect	Inundation Depth [ft]			Velocity [ft/s]		
		EGL	Extended EGL	Site Specific	EGL	Extended EGL	Site Specific
A	(-) 22.5	20.31	23.08	25.27	19.61	21.26	24.89
A	Center	18.88	33.57		17.97	24.67	
A	(+) 22.5	11.83	29.68		13.86	22.33	
B	1	2.03	10.00	8.61	2.45	7.42	9.60
B	2	1.36	5.44		1.93	3.97	
B	3	2.66	10.67		3.38	7.38	
C	1	4.12	33.43	25.19	7.97	28.04	37.12
C	2	22.07	28.74		23.14	26.80	
C	3	26.63	30.70		25.74	27.76	

2.4.3. Sensitivity of EGL Analysis to Digital Elevation Models

As discussed previously the digital elevation models used for the site-specific analysis may not be of the same accuracy as those available for public use with the energy grade line analysis. The sensitivity of the EGL results to variations in the DEM data is examined using the IfSAR and USGS DEM ground elevation data for the location of Hilo, Hawaii. The extended energy grade line method is performed for three transects at site A using the IfSAR and USGS DEM ground elevation data. These results are compared to the site-specific analysis which was conducted using the IfSAR DEM (Figure 34). It should be noted that slight variations observed in the ground elevation along the transect for the site-specific and IfSAR extended EGL because the site-specific data is based on the IfSAR data, but at a reduced sampling resolution.

A comparison between the extended EGL analyses performed using the two different DEMs shows that there can be a slight discrepancy in the velocity and inundation depth results based on the accuracy of the DEM. For example, this can

be seen in the results of the +22.5 transect (Figure 34) where the USGS DEM is providing a higher approximation of the velocity and inundation depth compared to the IfSAR DEM. However, the discrepancy in results between the two DEMs is more notable for the transects beyond the inundation limit, as can be seen in the +22.5 and center transect plots. Although the discrepancy in the DEM data does introduce some error into the EGL method, based on this comparison the difference in DEMs do not result in considerable differences in estimated demands. That is, the method appears to be relatively stable with respect to small differences in elevation models. Therefore the major reason for the difference in inundation height and water velocity at the building site between the EGL and site-specific method can be attributed to the discrepancy in DEM elevation and runoff elevation at the inundation limit.

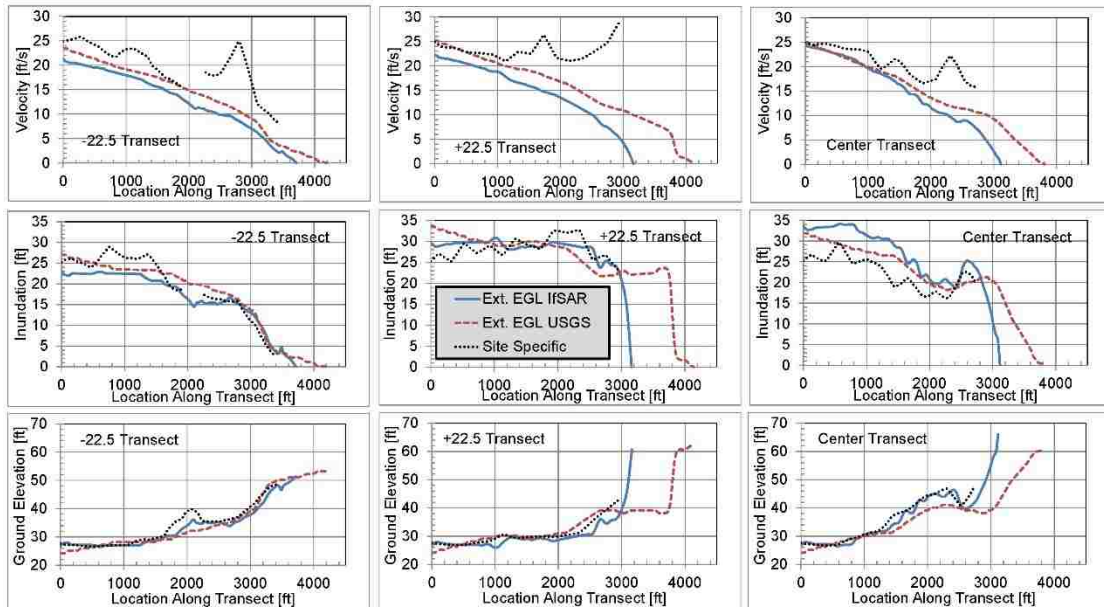


Figure 34: Comparison of digital elevation models

2.5. Future Work

The site assessment procedures developed for structures subjected to tsunami generated debris represent the first major effort to provide design guidance in this area. Much of the guidance developed to assess for potential debris impact is based on the investigation of the 2011 Tohoku event. One concept which can be further refined with continued research is the debris impact hazard region. This region is developed based on the assumption that the debris will travel along the same path as the flow. Applying this assumption the debris impact hazard region captures 90% of the debris spread of a particular large debris item in the areas of Japan studied for this research effort. Experimental investigation of debris transport in tsunami flow can be performed to investigate the debris dispersal and quantify the percentage of debris that remains in the debris impact hazard region. The experimental study can also be used to investigate if it is typical for debris to travel further inland than predicted by the impact hazard region and then be transported back within the region during the outflow event. This parameter could not be studied during the development of the impact hazard region as only the final location of the debris could be determined from the satellite images.

In addition to performing an experimental study, a probabilistic approach to quantifying the debris spread can also be applied. As the debris does not spread evenly throughout the debris hazard zone it would be useful to assess this spread in a probabilistic manner. Being able to quantify the probability of debris impact within the currently established debris impact hazard region may allow the established region to be modified based on the results. If there are locations within the debris impact hazard region that have extremely low probabilities of impact than from an economic perspective reducing the debris impact hazard region would be appropriate. However, if there are locations that have high probability of impact outside of the impact hazard region, which may be due to unique topographical

characteristics of the site, then it is important that design engineers extend the region and design against the threat of debris impact. Overall, further research and advancements to the established site assessment procedures will provide design engineers with useful tools to protect human life and reduce economic loss in tsunami prone regions.

2.6. Conclusions and Contributions

This section summarizes the conclusions of this research effort and contributions made to the field of structural engineering. The result of this overall research effort is the development of site assessment procedures for structures subjected to tsunami generated debris impact. As part of these procedures a classification system was developed to group debris items by potential impact demand levels, an impact hazard region was developed to quantify a probable dispersion region for which structures will be designed to withstand impacts from large debris items and modifications to the energy grade line method were proposed to produce more conservative values of water velocity and inundation depth compared to site-specific analysis results. The site assessment procedures developed during this research effort provide engineers with improved guidance to design structures to withstand the effects of impacts from tsunami generated debris and with design tools to use for urban planning in tsunami prone regions.

Summarized below are the major contributions of this research effort:

- A classification system was developed for tsunami generated debris based on four characteristics that influence the potential impact force a debris item can generate. These four debris characteristics are: mass, stiffness, buoyancy and cumulative length. Utilizing the characteristic limits a debris item can be classified as small, moderate or large debris. The classifications are directly related to the impact demands the debris item can generate. A large debris type can generate extreme impact demands typically greater than 1000 kips and small debris will generate low impact demands typically less than 6 kips. Moderate debris is any debris falling in-between. The developed debris classification system allows design engineers to approximate impact force demands of potential debris types that may not

have mass and stiffness characteristics provided by ASCE 7-16. The debris classification system is also presented in Naito et al. 2014.

- A debris impact hazard region was established based on debris dispersal patterns observed during the 2011 Tohoku tsunami in Japan. The impact hazard region is used to quantify a probable dispersion region for which structures will be designed to withstand impacts from large debris items such as shipping vessels and shipping containers. The debris impact hazard region and related procedures for applying this region to tsunami prone locations were adopted by ASCE 7-16 and also published in Naito et al. 2014.
- A modification to the energy grade line method was developed to account for potential nonzero inundation depths at the inundation limit. The potential for the nonzero inundation depth is due to modeling discrepancies between the elevation assumed by the large grid size used in the site-specific model and the elevation determined using the digital elevation model data for the same point. Due to the fact that the runup elevation provided by ASCE 7 is based on the results of site-specific modeling there is a potential for this elevation to be greater or less than the corresponding DEM elevation at that point. The developed extended energy grade line approach allows for this difference in elevation to be accounted for by extending the energy grade line to an elevation on the DEM that is equal to the ASCE run up elevation. The result is the extended energy grade line method produces closer approximations to the site-specific method for velocity and inundation depth at a building site compared to the traditional energy grade line analysis. The extended energy grade line approach has also been published in Naito et al. 2016.

3. INNOVATIVE SHEAR CONNECTOR FOR COMPOSITE SYSTEMS

The goal of this research project, funded by the Pennsylvania Department of Transportation, is to develop an economical, precast steel/concrete composite highway bridge system, comprised of a steel WT section cast into a concrete deck that will be used as a replacement system for the states aging infrastructure. The precast sections are design to be light-weight and utilize the stem of the WT to create the shear connection between the steel and concrete. In order to reduce cost the precast beam sections are designed so that they be easily fabricated and erected on site using cast in place closure joints. The research effort is divided into three phases: (1) FlexBeam system prototype design for flexural requirements; (2) experimental evaluation of shear connection details, FlexBeam prototype system shear detail design, development of construction methods; (3) full scale experimental validation of proposed FlexBeam system design. The original work presented in this document is based on phase two of this research effort.

3.1. Introduction

A feasibility study was conducted on a potentially economical steel/concrete composite highway bridge system for the Pennsylvania Department of Transportation. The system is comprised of a series of split standard steel wide-flange shapes (steel WT sections) precast into a doubly reinforced concrete deck slab section. It is the intention that each composite WT concrete-slab beam will be precast independently, delivered to the bridge site, erected on simply supported boundary conditions, and the concrete slabs of the adjacent WT-concrete-slab beams will be joined with a high strength concrete longitudinal closure joint. The beam system is envisioned to be utilized for spans of approximately 50ft with each precast WT-concrete-slab beam weighing less than 18,000 lbs. The composite system is referred to in this document as the PA FlexBeam. In a previous phase of the research effort, a prototype FlexBeam system was designed that meets the Strength I flexure requirements, the Service II stress requirements, and the Service I deflection requirements for a bridge with no pedestrian traffic (Aghl, Naito & Sause, 2014).

The focus of the research effort presented in this chapter examines the shear transfer mechanism between the concrete slab and steel WT web as well as develops construction methods for the system. A series of potential FlexBeam connector details are experimentally examined with push-off tests. The proposed connections consisting of drilled holes with or without reinforcing bars are tested to failure. Utilizing the results from the push-off tests an analytical method to predict the shear capacity of the FlexBeam connector is developed. Based on the flexural design of the selected prototype WT20x74.5 FlexBeam system, shear connection details are designed. To achieve adequate shear transfer while maintaining constructability a shear connector detail consisting of 1.5 in. diameter holes spaced between 4 and 12 in. on center with #6 bars through bars are used. Construction

methods for the precast segment fabrication and system erection are developed and presented. The potential for the system to form a lateral torsional buckling mode during fabrication and erection is found to be unlikely. To achieve a recommended camber of 0.5 in. over the 50 ft span a recommendation on initial WT camber and deck forming process is developed and summarized.

3.2. Background

3.2.1. Composite Systems

Composite bridge systems have gained interest in the engineering community due to the ability for these sections to be cost effective alternatives to traditional steel or concrete systems. When properly designed, these systems take advantage of the concrete's ability to perform well under compressive stress and the steel's ability to resist the tensile stress. Composite systems can also allow for a more rapid construction time as a result of the ability for these sections to be prefabricated.

Due to the fact that these systems are comprised of two distinct components, steel and concrete, a structural connection between the two materials is required. Shear connectors are utilized to join the two materials and achieve the required composite action. The connectors provide a mechanism for shear transfer between the steel and concrete components and are essential components in resisting slip. Many different shear connectors have been developed and evaluated for use in composite beams including: shear studs, channel connectors, Perfobond, T-Perfond, Crestbond, and perforated shear connectors among many others.

3.2.1.1. Shear Connectors

Shear studs are one of the most widely used shear connectors in composite systems, particularly building systems, because these connectors offer an advantage in that they can be automatically welded to the flange of the steel beam. The behavior of shear studs as a connector in composite systems has been heavily researched and shear strength calculation methods have been established by AASTHO guidelines. The main issue with using shear studs in composite bridge systems is that the capacity of a single shear stud is relatively low and therefore a large quantity of shear studs are required to attain the overall required shear capacity of the system.

In response to the need for a shear connector more suitable to bridge beam applications the Perfobond connector and other similar perforated connectors have been developed and studied (Leonhardt et al. 1987; Oguejofor and Hosain 1993, Roberts and Heywood 1995; Oguejofor and Hosain 1997; Ushijima et al. 2001; Vianna et al. 2008; Martins, Costa-Neves & Vellasco 2010; Ahn et al. 2010). The advantage of these types of connectors is that they can provide an increased shear capacity per connector compared to traditional shear studs. The Perfobond type connector is a steel rib with a series of holes in a set pattern that is welded to the top flange of an I-beam before casting of the concrete deck. The holes in the steel rib provide the required composite shear connection through concrete dowel action. In the context of composite system strip connectors the term concrete dowel is used to refer to the shear resistance of the connector provided by the concrete passing through the connector holes. The formation of the concrete dowels is explained in Oguejofor and Hosain (1993), where the concrete that flows through the rib holes forms dowels that provide resistance to shear in the horizontal direction and prevent vertical separation. In addition, reinforcing bars can be placed through the rib holes to provide a steel dowel action mechanism, which results in increased capacity and ductility of the system.

Although the Perfobond type connector can increase the shear capacity of the beam in comparison to traditional shear studs, these connectors still need to be welded onto the top flange of the I-beams which increases the required material and labor needed to construct the beam. One innovative way to reduce the labor and material cost is to utilize WT-beams with holes cut through the web instead of I-beams with rib connectors welded on the flange. In this application the web of the WT-Beam becomes the connector, saving both material and labor costs. Based on this concept the FlexBeam connector system was designed utilizing WT sections with holes in the web to provide the shear connection for the concrete deck and to resist the

tensile forces induced in the composite girder under service loading. This newly developed connection detail will be referred to as the FlexBeam connector.

As previously mentioned the FlexBeam, Perfobond and other similar connector types are utilized as a means to provide composite action between a concrete deck slab and steel girder. They serve as a replacement to the more commonly used headed studs. The function of the connector is to resist horizontal shear and vertical uplift force at the interface between the steel and concrete components. Since its development in the late 80's, many variations of the Perfobond system have been examined. This includes the use of indented cuts to support reinforcement and a T-shape to increase the bearing area of the connector. A brief overview of the different composite connector types that have been developed can be seen in Table 4.

Table 4: Composite Connectors	
<p>Studs</p> <p>(Image from Vianna et al. 2008)</p>	
<p>Perfobond</p> <p>(Image from Vianna et al. 2008)</p>	
<p>Crestbond</p> <p>(Image from Vianna et al. 2008)</p>	
<p>T-Perfobond</p> <p>(Image from Vianna et al. 2008)</p>	

Although there are many similarities between the proposed FlexBeam connector and Perfobond connector, the main shear resistance mechanisms are different. The Perfobond, Crestbond and T-Perfobond connectors shown in Table 4 utilize three main contributions to the overall resistance when reinforcement is placed through the holes. The three main contributions include: (1) end bearing resistance, (2) shear resistance of the concrete dowel and (3) shear resistance of the transverse rebars passing through the connector holes. These contributions to horizontal loading are illustrated in Figure 35. It should be noted that there is some bond effect

between the concrete and the steel plate, but it does not account for much of the overall resistance and can therefore be neglected (Ahn et al. 2010).

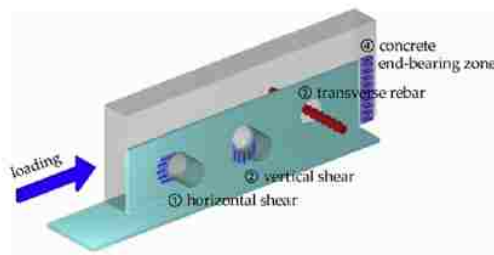


Figure 35: Mechanical behavior of a Perforated shear connector (Ahn et al. 2010)

In the case of the FlexBeam connector (Figure 36) the web of the WT runs continuously along the deck span. Under this scenario there is no end bearing zone. Based on this fact the contribution to the overall strength for the FlexBeam connector is primarily due to the shear resistance of the concrete dowel and the shear resistance of the transverse rebars passing through the connector holes. It is predicted that formulas developed for the Perforated connector will therefore overestimate the capacity and not be reliable for strength prediction of the FlexBeam connectors. Therefore a new equation unique to the FlexBeam connector will need to be developed to accurately approximate the shear capacity.

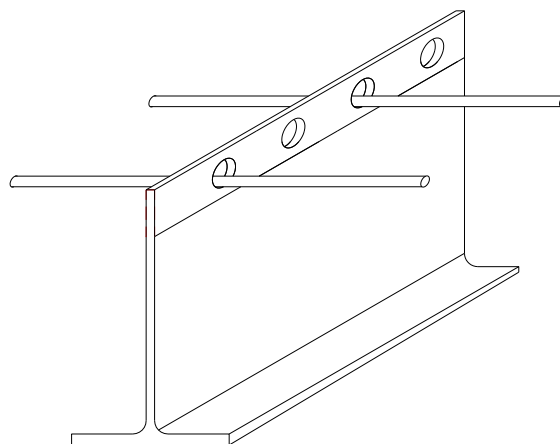


Figure 36: FlexBeam connector

3.2.2. FlexBeam Flexural Design Prototype

In a previous phase of this research effort (Aghl, Naito & Naito, 2014) a prototype FlexBeam system was designed based on the following criteria. The prototype concrete deck section is assumed to be 8 in. thick and 30.75 in. wide. It is the intention that each composite WT-concrete-slab beam section will be precast independently, delivered to the bridge site, erected on simply supported boundary conditions, and the concrete slabs of the adjacent WT-concrete-slab beams will be joined with a high strength concrete longitudinal closure joint. The beam system is envisioned to be utilized for spans of approximately 50ft with each precast WT-concrete-slab beam weighing less than 18,000 lbs.

As part of the phase one research effort four different FlexBeam cross sections, WT 15 x 163, WT16.5x59, WT20x83.5 and WT20x74.5, were examined based on their behavior and ability to satisfy design requirements. An analytical study of the composite members was conducted to assess the flexural behavior of the PA FlexBeam over the range of loading from service to ultimate conditions. The location of the neutral axis over the range of loading and ultimate failure modes was also examined.

The following material properties and constitutive relationships were assumed for the flexural section analysis. The material utilized in the FlexBeam section are: concrete, structural steel and reinforcing steel. The concrete is assumed to meet the requirements of PennDOT class AAAP Concrete, which has a design compressive strength of 4000 psi at 28-days. At the bridge site, the precast WT-concrete-slab beams will be joined with an Ultra High Performance Concrete (UHPC) longitudinal closure joint. The UHPC is assumed to meet the PennDOT B-14-005 28-day strength requirement of 21.7 ksi based on cube tests. The deck reinforcement is assumed to be grade 60 material meeting the requirements of ASTM A706. The structural steel

is assumed be grade 50 material meeting the requirements of ASTM A992. The concrete stress-strain behavior is modeled using the Popovics Model [1973]. The tensile stress-strain behavior of the concrete is included up to the modulus of rupture of $7.5\sqrt{f'_c}$. A concrete elastic modulus of 3644 ksi is assumed. For the purposes of the section analysis, at a compressive strain of 0.003 the concrete is assumed to be effectively "crushed". The flexural capacity of the composite sections from the fiber analyses is established when the compressive strain capacity of 0.003 is reached. The minimum specified yield strengths and facture strains (60 ksi & 0.14 and 50 ksi and 0.21 for ASTM A706 Gr.B and A992, respectively) were used for the steel. The steel materials are assumed to be elastic-perfectly plastic with an elastic modulus of 29,000 ksi.

The demands and capacities of the FlexBeam section were examined based on the following design assumptions. The bridge (see Figure 37) is assumed to have a 27' and $\frac{3}{4}$ " wide deck, with 9 beams spaced at 36.75 in. UHPC joints are assumed to be 6 in wide based on prototype design provided by PennDOT. The bridge is assumed to carry two standard 12 ft design lanes. The flexural capacities of the FlexBeam sections are computed in accordance with PennDOT Design Manual Part 4 (DM4). The demands are computed in accordance with PennDOT Design Manual Part 4 (DM4). The FlexBeam is analyzed under dead loads plus the PennDOT PHL-93 vehicular live load. The live load consists of the design truck or design tandem in addition to the lane load. As noted in DM4 Article 3.6.1.2.3 the weight of each axle for the tandem is increased from 25 kips to 31.25 kips.

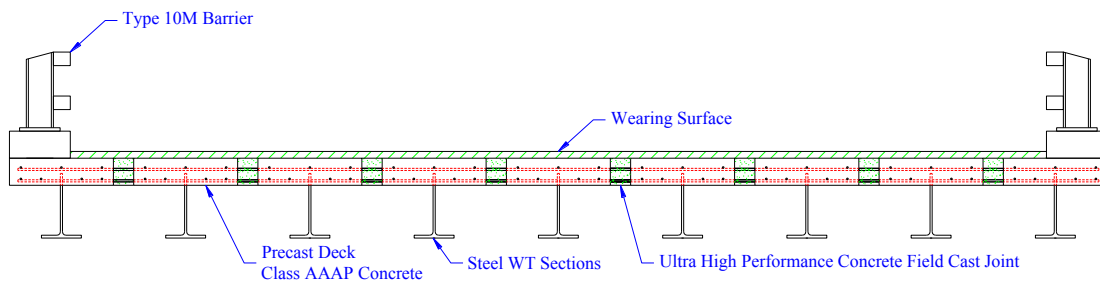


Figure 37: FlexBeam bridge system cross section

The analysis of the four FlexBeam sections resulted in the following conclusions made by Aghl, Naito & Naito (2014). The heavy WT15x163 FlexBeam section does not meet the weight limit requirement of 18 kips and is controlled by concrete failure, therefore the section does not have a stable yield plateau, making it an undesirable selection. The WT16.5x59 FlexBeam section does not meet the deflection limit requirements under the Service I load combination. The WT 20x74.5 and the WT 20x83.5 FlexBeam sections both meet the flexural design criteria for the Strength I limit state, and provide ductile flexural behavior controlled by yielding of the WT steel section. Both the WT 20x74.5 and the WT 20x83.5 sections also meet the flexural design criteria for the Service II limit state, and the Service I deflection criteria for bridges without pedestrian loads. Therefore the WT 20x74.5 and the WT 20x83.5 FlexBeam sections were recommended for further investigation in phase two of the research effort. Details of the final section and end diaphragm based on the flexural analysis are illustrated in Figure 38 and Figure 39. Additional information on the design assumptions and flexural analysis can be found in Aghl, Naito & Naito (2014).

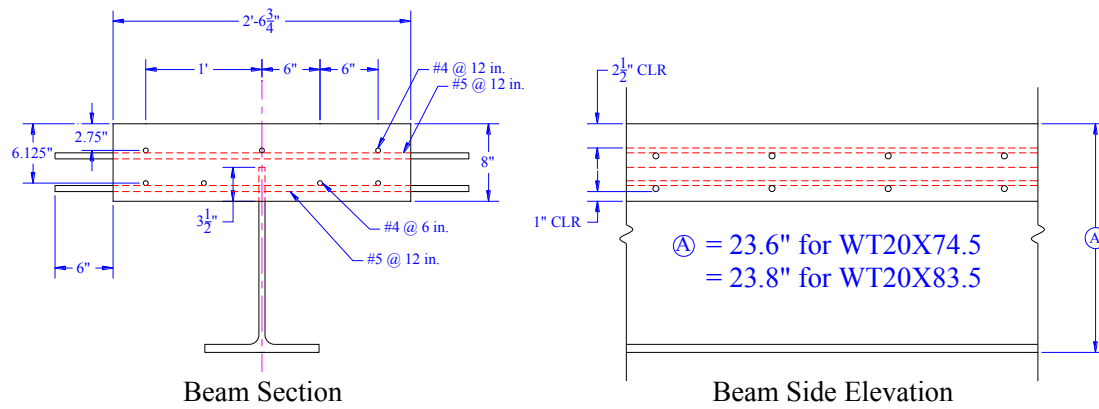


Figure 38: Beam section and side elevations (Aghi, Naito & Sause, 2014)

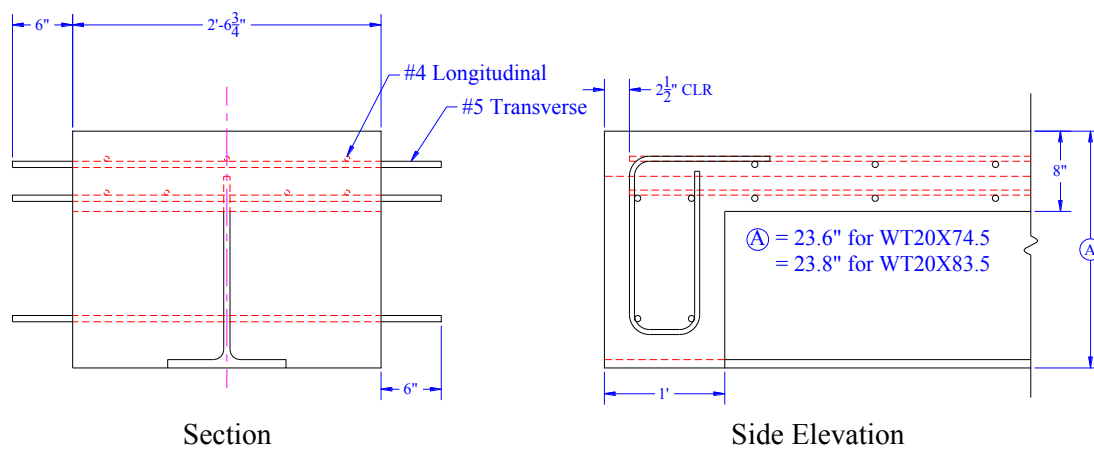


Figure 39: End diaphragm details (Aghi, Naito & Sause, 2014)

3.3. Shear Strength Evaluation

An experimental testing program was devised and implemented to determine the shear capacity of the FlexBeam shear connection. The experimental test program aimed to study the effects of using a WT shape with the web continuously embedded in a concrete deck. The hole diameter, hole spacing, reinforcement bar size and reinforcement shape are varied. The goal of the experimental testing is not only to determine an experimental capacity of the tested connector configurations but to also develop design guidance to calculate estimated shear capacity of other connector configurations.

3.3.1. Experimental Test Specimen Design

The test specimens were designed to replicate the FlexBeam prototype design dimensions and details. The test specimen consists of a concrete slab which mirrors the FlexBeam deck thickness and width as well as the reinforcement layout and a steel plate that has the same thickness, embedment length and material properties as the anticipated WT section. To facilitate loading without the generation of significant eccentricities a symmetric push-off specimen with two concrete flanges was developed. The push-off detail relative to the FlexBeam configuration is illustrated in Figure 40. A comparison between the key properties of the FlexBeam prototype specimen and the experimental test specimen can be found in Table 5.

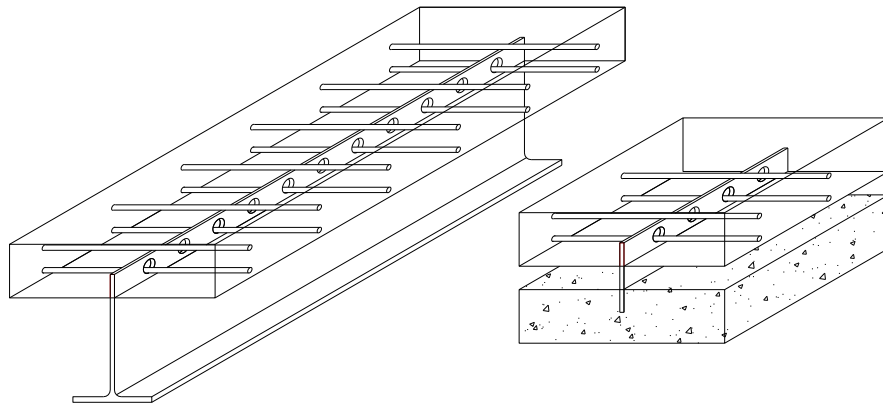


Figure 40: FlexBeam and push-off specimen concepts (longitudinal bars not shown)

Table 5: Comparison of FlexBeam prototype and test specimen		
	FlexBeam Prototype	Push-off Test Specimen
Beam Length	50 ft.	2 ft.
Deck Slab Thickness	8 in.	8 in.
Deck Slab Effective Width	36.75 in.	37.5 in
Reinforcement	ASTM A 615 Grade 60	ASTM A 615 Grade 60
Number of Longitudinal Reinforcement Layers	2	2
Longitudinal Reinforcement Bar Size	#4	#4
Longitudinal Reinforcement Top Layer Spacing	12 in. maximum	6 in.
Longitudinal Reinforcement Bottom Layer Spacing	6 in.	6 in.
Number of Transverse Reinforcement Layers	2	2
Transverse Reinforcement Bar Size	#5	#5 or #6
Transverse Reinforcement Top Layer Spacing	12 in. maximum	12 in.
Transverse Reinforcement Bottom Layer Spacing	12 in. maximum	Varies
Slab Top Cover	2.5 in.	2.5 in.
Slab Bottom Cover	1 in.	1 in.
Depth of WT/ Plate Embedment	3.5 in	3.5 in
WT/ Plate Section	ASTM A 709 Grade 50	ASTM A 709 Grade 50
WT/ Plate Thickness	0.55 -0.65 in.	0.625 in.

To reduce effects caused by unsymmetrical loading during testing and to place the connections under shear loading, the specimen was designed to be symmetric. This resulted in having the steel plate embedded into a concrete slab on each side. Additionally, at the point of bottom bearing of the test specimen a 4 in. by 4 in. portion of the concrete slab was removed to allow the applied force to pass through the centroid of the connection holes during testing, again reducing any loading eccentricities. A schematic of the test specimen can be seen in Figure 41.

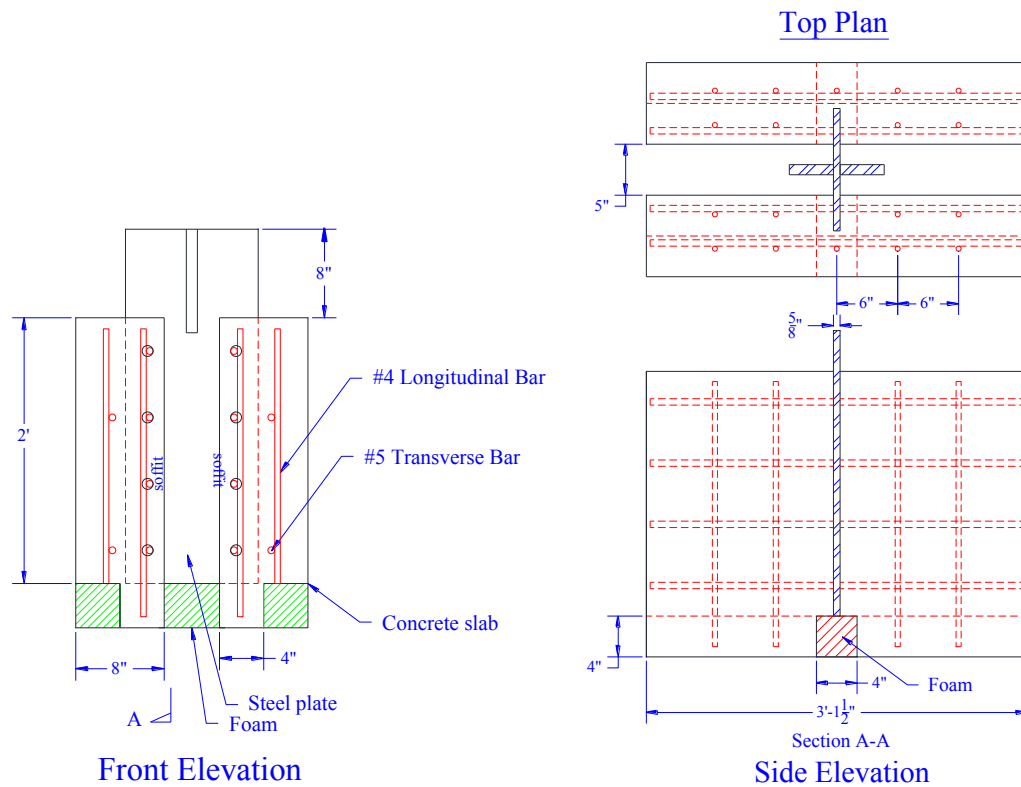


Figure 41: FlexBeam Test Specimen Schematic

All test specimens were fabricated at the ATLSS Center of Lehigh University. Wood formwork and foam material was used to create the desired concrete dimensions. All foam was removed from the specimens prior to testing. The reinforcement bars used were all epoxy coated to meet PennDOT standards. The concrete used met the requirements of PennDOT Class AA. Class AA was selected for use over the Class AAAP in order to achieve a strength closest to 4000 psi on the date of testing, which is the lowest strength of concrete allowed in the field for this bridge deck. The steel plates were primed to meet PennDOT specifications by an outside vendor after all required holes had been drilled. This was done in an attempt to create a friction coefficient, similar to field conditions, between the steel and concrete surfaces. Additionally, steel pieces were welded perpendicularly to the steel plate to provide bracing and a stable contact area for the machine head during push down

testing. Figure 42 shows the test specimen during fabrication and the finished specimen after the formwork was removed.

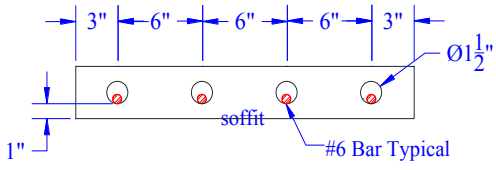
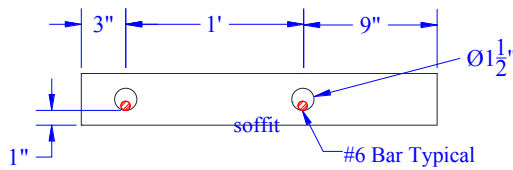


Figure 42: a) Test specimen fabrication b) Test specimen removed from form work

3.3.2. Experimental Testing Matrix

Experimental testing was conducted to evaluate how the shear capacity of the FlexBeam connector was influenced by a number of parameters including: hole diameter, hole spacing, reinforcing bar size and spacing, as well as the shape of reinforcement passing through the hole. Nine connector details were designed and tested. A description and schematic of each connector type is presented in Table 6.

Table 6: FlexBeam connector details		
Connector Type	Description	Connector Schematic
Type 1	Hole Size 1.5" diameter Hole Spacing: 6" Hole Reinforcement: None	
Type 2	Hole Size: 1.5" diameter Hole Spacing: 6" Hole Reinforcement: #5 bar at 12" spacing	
Type 3	Hole Size: 1.5" diameter Hole Spacing: 6" Hole Reinforcement: #5 bar at 6" spacing	
Type 3b	Hole Size: 1.5" diameter Hole Spacing: 6" Hole Reinforcement: #5 straight bar at 12" spacing #5 bent bar at 12" spacing	
Type 4	Hole Size 1" diameter Hole Spacing: 6" Hole Reinforcement: None	
Type 6	Hole Size: 1" diameter Hole Spacing: 6" Hole Reinforcement: #5 bar at 6" spacing	
Type 7	Hole Size: 1.5" diameter Hole Spacing: 12" Hole Reinforcement: #5 bar at 12" spacing	

Connector Type	Description	Connector Schematic
Type 8	Hole Size: 1.5" diameter Hole Spacing: 6" Hole Reinforcement: #6 bar at 6" spacing	
Type 9	Hole Size: 1.5" diameter Hole Spacing: 12" Hole Reinforcement: #6 bar at 12" spacing	

The experimental testing was divided into four test series. For each test series three connector types were tested. Based on the experimental results the connector types to be used in the next test series was selected. The test matrix used for the FlexBeam shear testing is presented in Table 7.

Test Series 1	Test Series 2	Test Series 3	Test Series 4
Type 1	Type 2	Type 3 (2)	Type 7
Type 4	Type 3 (1)	Type 3b (2)	Type 8 (2)
Type 6	Type 3b (1)	Type 8 (1)	Type 9

As a means to increase the shear capacity of the connector without using a larger size rebar the Type 3b connector was developed. The Type 3b connector detail required a modification to the rebar layout of the original specimen design. The Type 3b specimen utilized alternating bent and straight rebar through the plate holes. The bent bars were extended across the thickness of the specimen and placed on the top layer of transverse reinforcing bars. Figure 43 shows a schematic of the Type 3b specimen design. For all other connector types any reinforcing bars placed through the holes were kept straight.

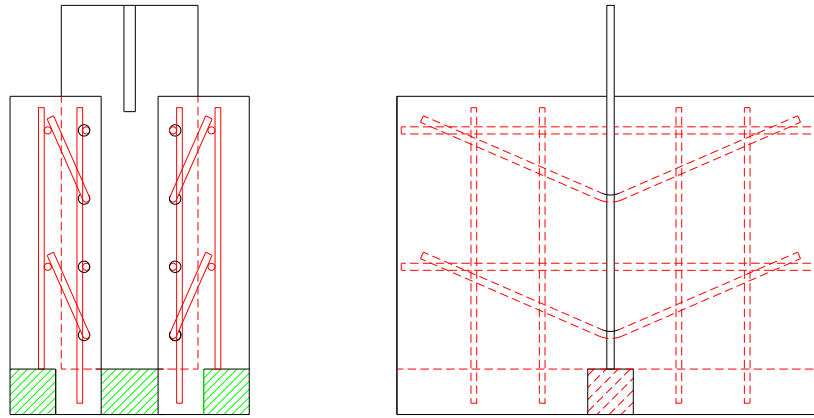


Figure 43: Schematic of a Type 3b test specimen

3.3.3. Experimental Setup and Procedure

Specimens were fabricated in four groups according to the test series matrix. For each test series three specimens were constructed in the ATLSS Center at Lehigh University. A minimum of 15, 4 in. x 8 in. cylinders were made during the casting of each set of specimens. Compression testing was conducted at minimum for 1, 3 and 7 days strengths. The goal was to test cylinders until the strength reached 4000 psi, which is the minimum required strength specified by PennDot for the bridge deck. Once the cylinders reached the desired strength of 4000 psi FlexBeam specimens were removed from the formwork.

After the removal of the formwork, the foam pieces used to create the required cavities in the test specimens were also removed. The specimens were then placed in a Universal Testing Machine (Satec). Homasote (fiber board) was placed under the specimens. The top plate was then checked for any skewness, if the plate was not plumb with head of the testing machine shims were used to level the specimen. This process assured that loading of the plate did not produce any unwanted eccentricities. Next, four LVDT sensors used to measure the shear slip of the plate were installed on the specimen. The LVDTs were attached to the plate using steel connector pieces and placed away from the inner face and plate to allow for

measurements to be taken even after potential crushing and spalling of the concrete has occurred. Once installed, the LVDTs were leveled to ensure accurate slip measurements. The test specimen set up in the Satec machine and location of the LVDT sensors can be seen in Figure 44.

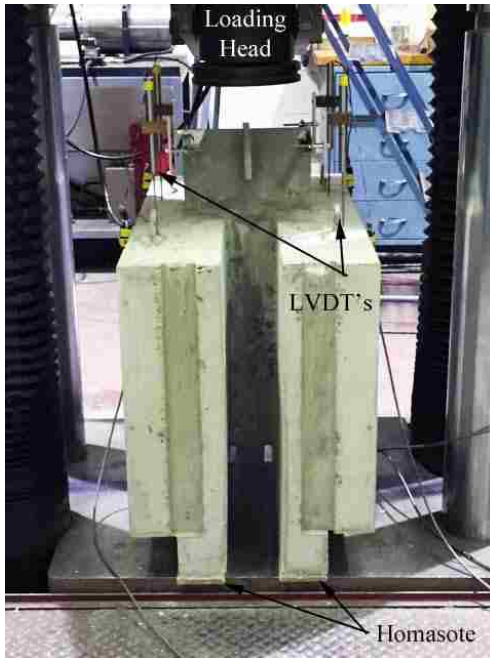


Figure 44: Test Specimen Set Up in Satec Machine

The specimen was then loaded initially using a load controlled rate as a soft-start mechanism and after reaching 20,000 pounds was switched to a displacement controlled rate of 0.02 in./sec. This displacement rate was used through the first peak load. At larger displacements, after the peak load was achieved, the rate was manually switched to 0.05 in./sec. and then 0.1 in./sec toward the end of the loading history. The time at which load increments were switched was dependent on the particular test and was recorded. During loading a data acquisition system was used to record the displacement of the LVDTs as well as the machine load and head travel. The machine was programmed to stop loading when the force dropped below 30% of the measured peak load. For majority of the test specimens this

criteria was reached but a few tests were manually stopped mostly due to limitations of the displacement gages.

3.3.4. Experimental Results

3.3.4.1. Cylinder Compressive Strength Testing and Reinforcement Yield Strength

The experimental test program was conducted in four test series. The concrete cylinder compressive strength for each test series is presented in Table 8. It is important to note that for Test Series 2 even though a strength of 4000 psi was achieved at 7 days a malfunction of the Satec testing machine delayed testing until 15 days. For Test Series 1 the three specimens were tested over a span of two days which is the reason for the 7 and 8 day strength values. The yield strength from the mill certifications for the #5 and #6 reinforcing bars are provided in Table 9.

Age	Test Series 1	Test Series 2	Test Series 3	Test Series 4
1 Day (psi)	2483	2458	1915	2142
3 Day (psi)	3678	3325	3065	3532
7 Day (psi)	4436	4090	3636	4043
8 Day (psi)	4800	n/a	n/a	n/a
9 Day (psi)	n/a	n/a	4039	n/a
15 Day (psi)	n/a	4776	n/a	n/a

#5 Bar	71000 psi
#6 Bar	68852 psi

3.3.4.2. FlexBeam Shear Test Data Summary

For all test specimens force-displacement curves were generated based on the recorded data. The shear slip is taken as the average of the four LVDT sensors used to record the displacement of the plate relative to the top of the concrete specimen. Figure 45 shows the force-displacement curves for all twelve specimens. From the force-displacement curves it can be seen that some specimens are able to regain

strength past the initial peak. In these cases the reload peak occurred after the specimen had undergone significant damage. For this reason the maximum load for all cases is taken as the first peak. The concrete strength at the time of testing, maximum load and corresponding shear slip of the plate for each specimen are summarized in Table 10.

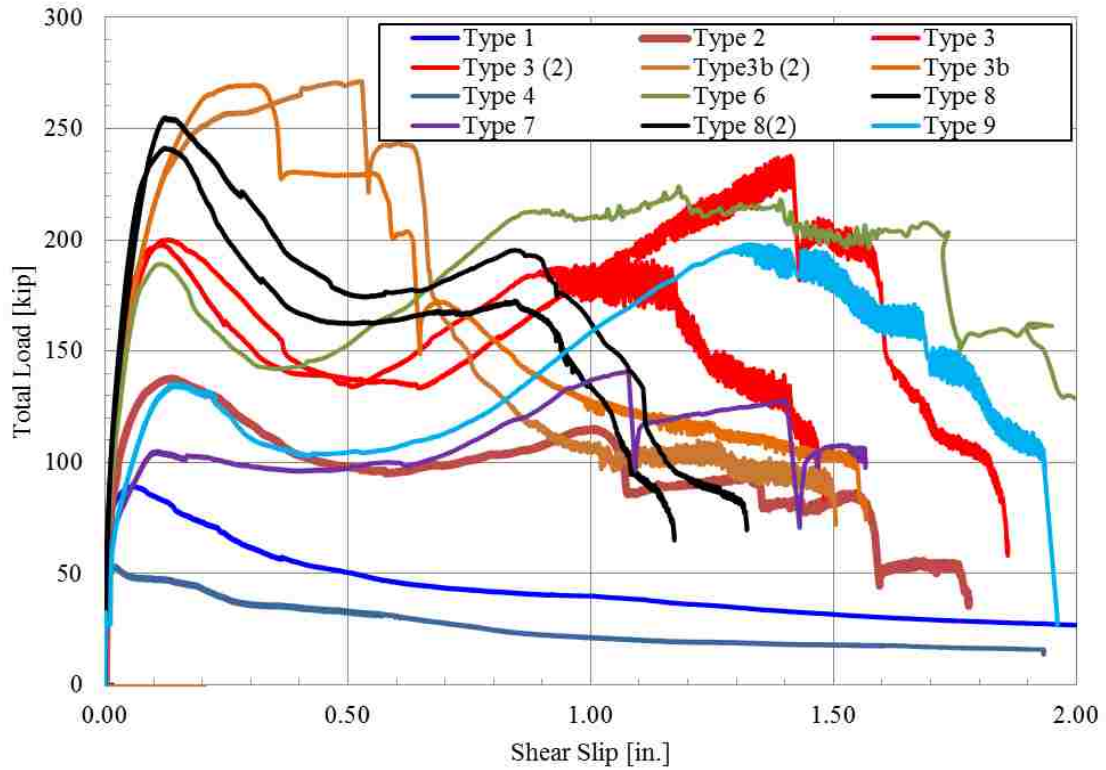


Figure 45: Experimental testing force-displacement curves

Connector Type	Average f'_c [psi]	First Peak Load [kips]	Slip at First Peak Load [in.]
Type 1	4436	89.5	0.06
Type 2	4800	137.7	0.14
Type 3	4800	200.2	0.13
Type 3(2)	4039	198	0.12
Type 3b	4800	269.7	0.31
Type 3b(2)	4039	271.3	0.53
Type 4	4776	53.6	0.02
Type 6	4776	189.3	0.11
Type 7	4043	105.0	0.10
Type 8(1)	4039	241.4	0.12
Type 8(2)	4043	255.0	0.12
Type 9	4043	135.4	0.14

Utilizing the experimental results a number of properties of the FlexBeam connector were analyzed including the effect of: hole size, reinforcing bar diameter, and hole spacing. The effect of the hole size can be examined by comparing the results between the Type 1 and Type 4 connectors where the only difference in the detailing is the change in hole diameter from 1 in. to 1.5 in. (see Figure 46). The comparison of these two connector details shows that as the area of the hole is increased so is the overall shear capacity. The effect of the hole size when bars are also present can be examined by comparing the results of Type 6 and Type 3 connectors. In this case the same increase in hole diameter (1 inch to 1.5 inch) only resulted in a 5% increase in shear capacity. This indicates that the concrete dowel action does not manifest itself when a bar is also present in the hole. For connections with bars through the holes the shear strength is driven by the steel dowel and not the concrete passing through the holes.

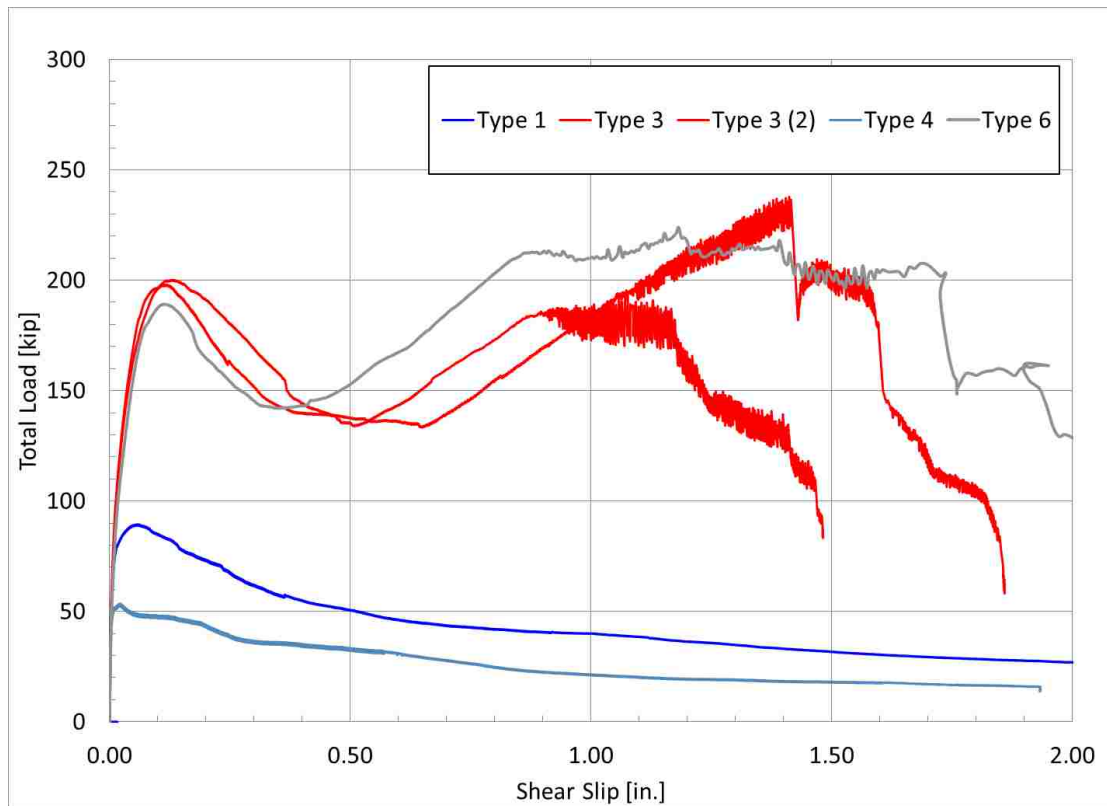


Figure 46: Effect of hole size

Testing also indicates that a concrete dowel mechanism is engaged and the strength of the dowel is related to the connector hole area. This concept can again be seen when comparing the Type 2 and Type 7 tests in Figure 47. These two connectors used the same rebar size and hole diameter but the Type 2 connector had four additional connector holes without reinforcing. These additional holes allowed for the formation of concrete dowel action in addition to the steel dowel action, which can be seen in the 33 kip increase in overall capacity of the Type 2 connector. This 33 kip increase correlates with the expected per hole capacity of a 1.5 in diameter hole, based on the experimental results of the Type 4 connector, of 7 kips per hole (28 kip increase accounting for the four additional holes used).

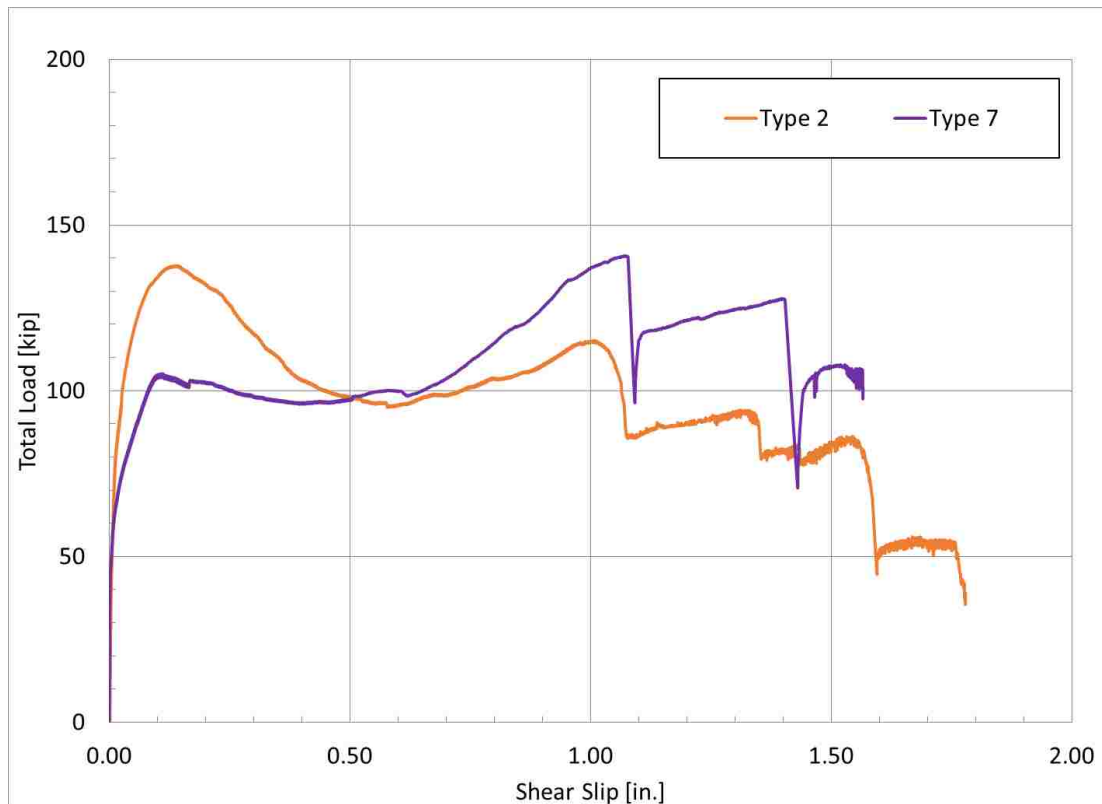


Figure 47: Effect of the concrete dowel

Reinforcing bar area also has an effect on the overall strength of the connection. Comparing the Type 3 and Type 8 results (Figure 48), in which the connector hole diameter, spacing and number of rebar used were kept the same, showed that going from #5 bars to a #6 bars resulted in an increase in overall strength of the connection. This trend can also be seen in the Type 7 and Type 9 results (Figure 48) where the connector hole diameter, spacing and number of rebar also remained the same but the bar size was increased from a #5 bar to a #6 bar. Again the increase in strength due to the increase in bar size can be observed. Based on the experimental results it is clear that increasing the bar diameter of the reinforcement passing through the connector holes will result in an increased shear capacity of the system. The fact that the strength is affected by the bar size indicates that the first peak load observed during experimental testing is driven by the steel dowel. The experimental data and analytical strength predictions suggest that decrease in

strength that occurs at the first peak load can be attributed to the initial yield of the rebar. The formation of this mechanism will be explained in more detail in a subsequent section.

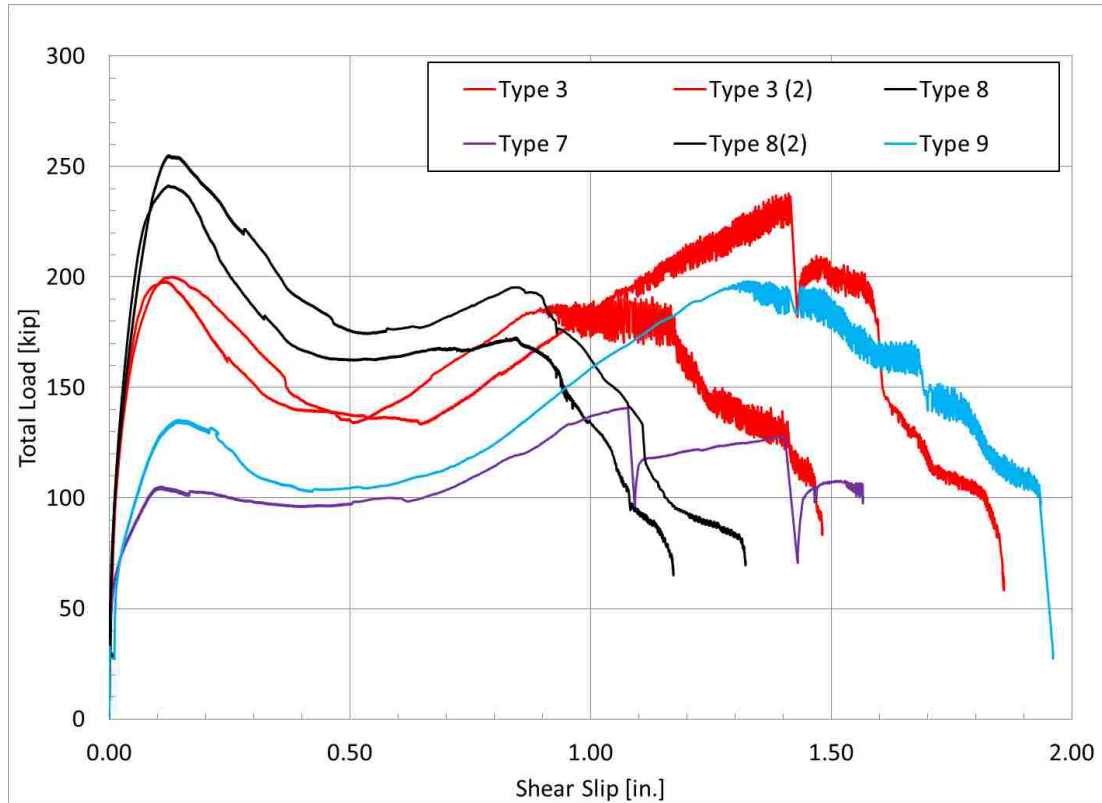


Figure 48: Effect of reinforcement size and hole spacing

Comparing the Type 3 and Type 7 as well as the Type 8 and Type 9 connectors (Figure 48), which have the same details expect for the hole spacing which was increased from 6 in. to 12 in., it can be seen that change in spacing had little effect on the per hole strength as indicted in Table 11. The specimens that had double the rebar and number of holes produced roughly double the strength. From the test results it can be assumed that any hole spacing greater than 6 in. will produce strengths equal to or greater than those approximated by a 6 in. spacing. It should be noted that there is likely a threshold spacing for which the per hole strength will decrease. This parameter was not investigated during this study and should be established through further experimental testing or finite element modeling.

Table 11: Shear strength per hole	
Connector Type	Per Hole Strength [kips]
Type 3	25
Type 7	26
Type 8	31
Type 9	34

3.3.4.3. FlexBeam Specimen Damage

Throughout testing photos were taken to document damage to the specimen. Of particular interest was the damage to the specimen corresponding to the first peak load. For all of the tests conducted there was no observable damage to the specimen when the first peak load was achieved. It was typical that as loading continued from this first peak small cracks began to appear on the inside face (corresponding to the bottom of the slab in the actual system) of the specimens. The final damage state of the specimens once the experimental failure load was achieved varied by connector type. The condition of the specimens after the experimental failure load had been reached can be seen in Table 12.

Table 12: Post Testing Specimen Damage	
<p>Type 1</p> <p>Hole Size 1.5" diameter</p> <p>Hole Spacing: 6"</p> <p>Hole Reinforcement: None</p>	

Table 12: Post Testing Specimen Damage









<p>Type 2</p> <p>Hole Size: 1.5" diameter</p> <p>Hole Spacing: 6"</p> <p>Hole Reinforcement: #5 bar at 12" spacing</p>		
<p>Type 3</p> <p>Hole Size: 1.5" diameter</p> <p>Hole Spacing: 6"</p> <p>Hole Reinforcement: #5 bar at 6" spacing</p>		
<p>Type 3(2)</p> <p>Hole Size: 1.5" diameter</p> <p>Hole Spacing: 6"</p> <p>Hole Reinforcement: #5 bar at 6" spacing</p>		
<p>Type 3b</p> <p>Hole Size: 1.5" diameter</p> <p>Hole Spacing: 6"</p> <p>Hole Reinforcement: #5 straight bar at 12" spacing</p> <p>#5 bent bar at 12" spacing</p>		

Table 12: Post Testing Specimen Damage










<p>Type 3b(2)</p> <p>Hole Size: 1.5" diameter</p> <p>Hole Spacing: 6"</p> <p>Hole Reinforcement: #5 straight bar at 12" spacing</p> <p>#5 bent bar at 12" spacing</p>		
<p>Type 4</p> <p>Hole Size 1" diameter</p> <p>Hole Spacing: 6"</p> <p>Hole Reinforcement: None</p>		
<p>Type 6</p> <p>Hole Size: 1" diameter</p> <p>diameter</p> <p>Hole Spacing: 6"</p> <p>Hole Reinforcement: #5 bar at 6" spacing</p>		
<p>Type 7</p> <p>Hole Size: 1.5" diameter</p> <p>diameter</p> <p>Hole Spacing: 12"</p> <p>Hole Reinforcement: #5 bar at 12" spacing</p>		

Table 12: Post Testing Specimen Damage

<p>Type 8(1)</p> <p>Hole Size: 1.5” diameter</p> <p>Hole Spacing: 6”</p> <p>Hole Reinforcement: #6 bar at 6” spacing</p>		
<p>Type 8(2)</p> <p>Hole Size: 1.5” diameter</p> <p>Hole Spacing: 6”</p> <p>Hole Reinforcement: #6 bar at 6” spacing</p>		
<p>Type 9</p> <p>Hole Size: 1.5” diameter</p> <p>Hole Spacing: 12”</p> <p>Hole Reinforcement: #6 bar at 12” spacing</p>		

As can be observed from the photos in Table 12 the connector types without rebar placed through the holes (Type 1 and Type 4) underwent the least amount of damage. Slight spalling of the concrete on the inside face occurred near the interface of the concrete and the bottom of the plate. Minimal cracking and spalling

was also observed along the inside face. In the connectors where straight rebar was utilized the damage level corresponds with the number and the size of the bar used. As the number of rebar crossing the shear plane was increased from four to eight per connector, the number of locations where cracking and spalling can be observed increased. In general the location where the cracking and spalling was initiated corresponds with the location of the rebar in the specimen. Therefore, as the number of holes with bars increased so did the number of locations of cracking and spalling along the inside face. As the size of the rebar increased the level of ultimate damage to the specimen increased. It is important to note that this damage occurred in the second range of response after the connection surpassed its initial peak strength. Comparing the Type 3 and Type 8 connectors it can be seen that the level of spalling on the inside face and the degree of splitting in the slab itself has become more apparent in the Type 8 connectors with the larger rebar size. When the shape of the rebar passing through the connector is altered, bent bars (Type 3b) versus straight bars (Type 3), so is the observable damage of the specimens. Utilizing the bent bars results in increased levels of spalling on the inside face and splitting of the deck slab. In one test specimen the Type 3b connector split the slab along the entire length specimen.

In general the higher levels of damage observed at the failure loads corresponded with a higher capacity of the connector type. As mentioned previously the images and resulting damage levels shown in Table 12 are a result of loading the test specimens until the strength drops to 30% of the peak load. The capacity of the connector, however, is established based on the first peak load observed during testing. At this level minimal damage is observed for all cases. Consequently, the level of damage shown in Table 12 is not expected in the actual FlexBeam even at overload. Under service loads the FlexBeam should have little to no visible cracking on the bottom of the deck.

3.3.4.4. Post-Testing Specimen Destructive Evaluation

After testing was completed a number of specimens were selected for destructive evaluation to better understand the failure mechanisms of the connector. One specimen of each of the following connector types was selected: Type 2, Type 3, Type 7 and Type 8. These specimens were selected based on the criteria that they include the different transverse rebar size, different holes spacing, and a combination of concrete and steel dowels. Using a hydraulic jack hammer the remaining concrete was removed from the specimens so that the transverse rebar through the connector and the connector plates could be removed and examined. The condition of the connector plates and connector bars removed post testing can be seen in Table 13 and Table 14.

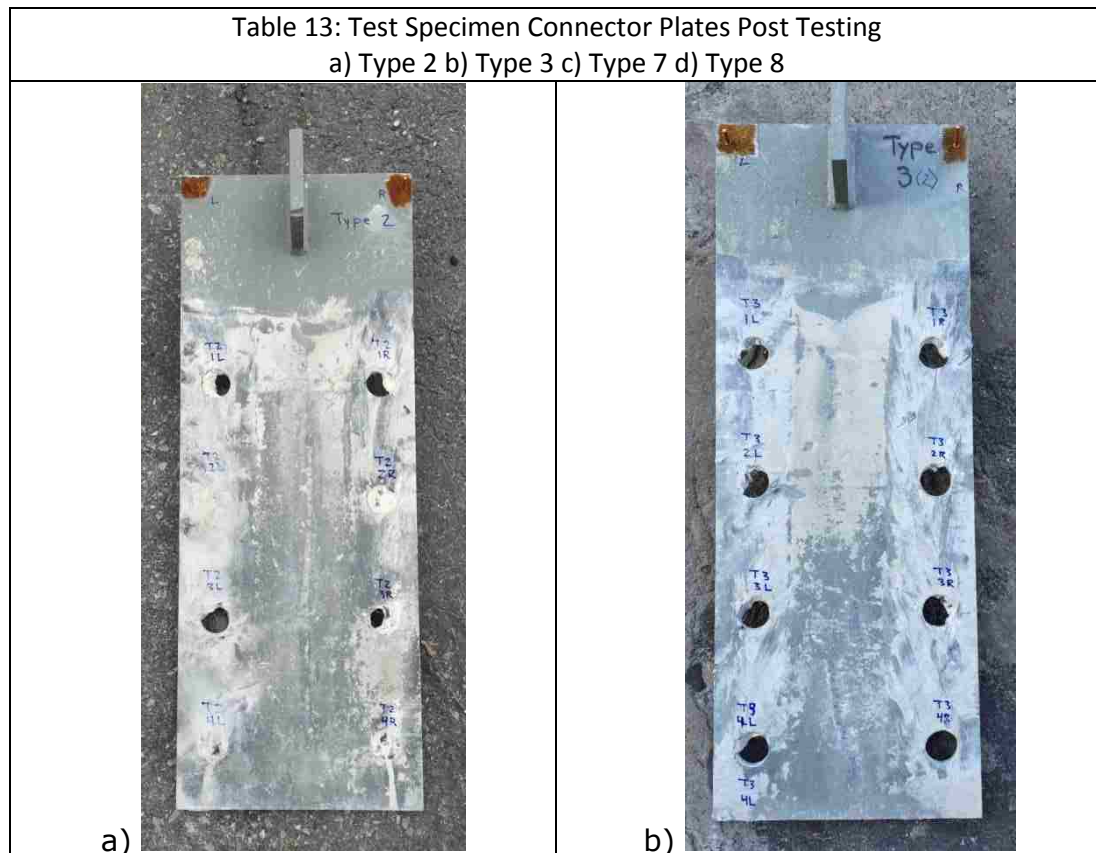


Table 13: Test Specimen Connector Plates Post Testing

a) Type 2 b) Type 3 c) Type 7 d) Type 8

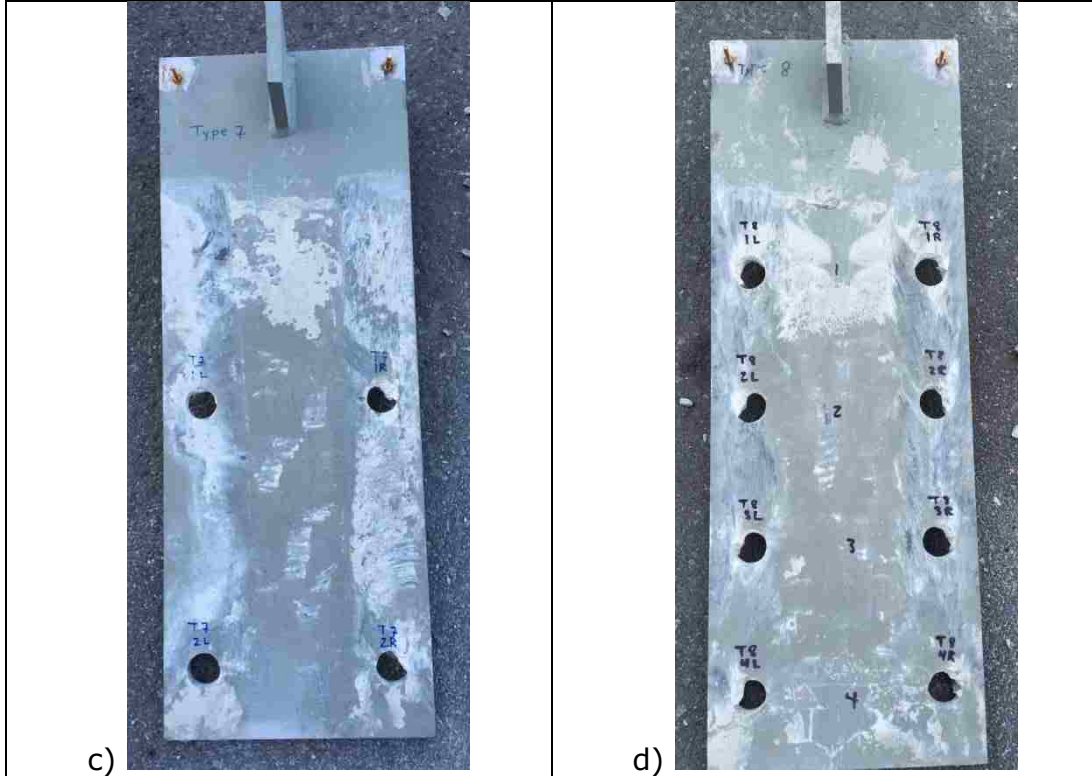
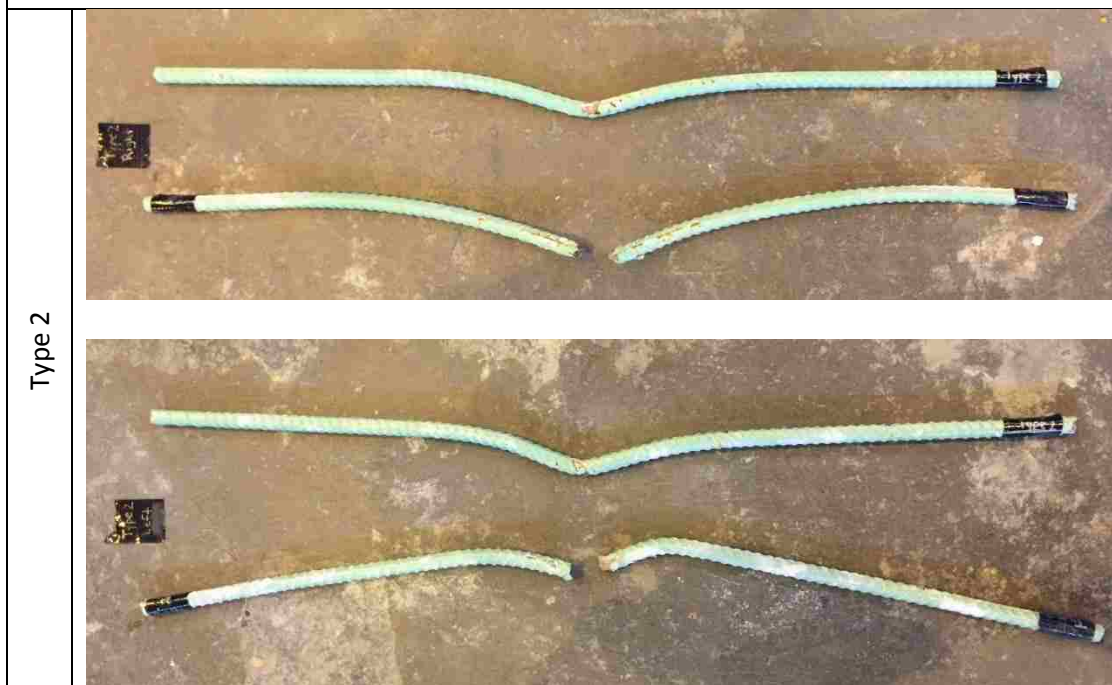


Table 14: Test Specimen Connector Bars Post Testing

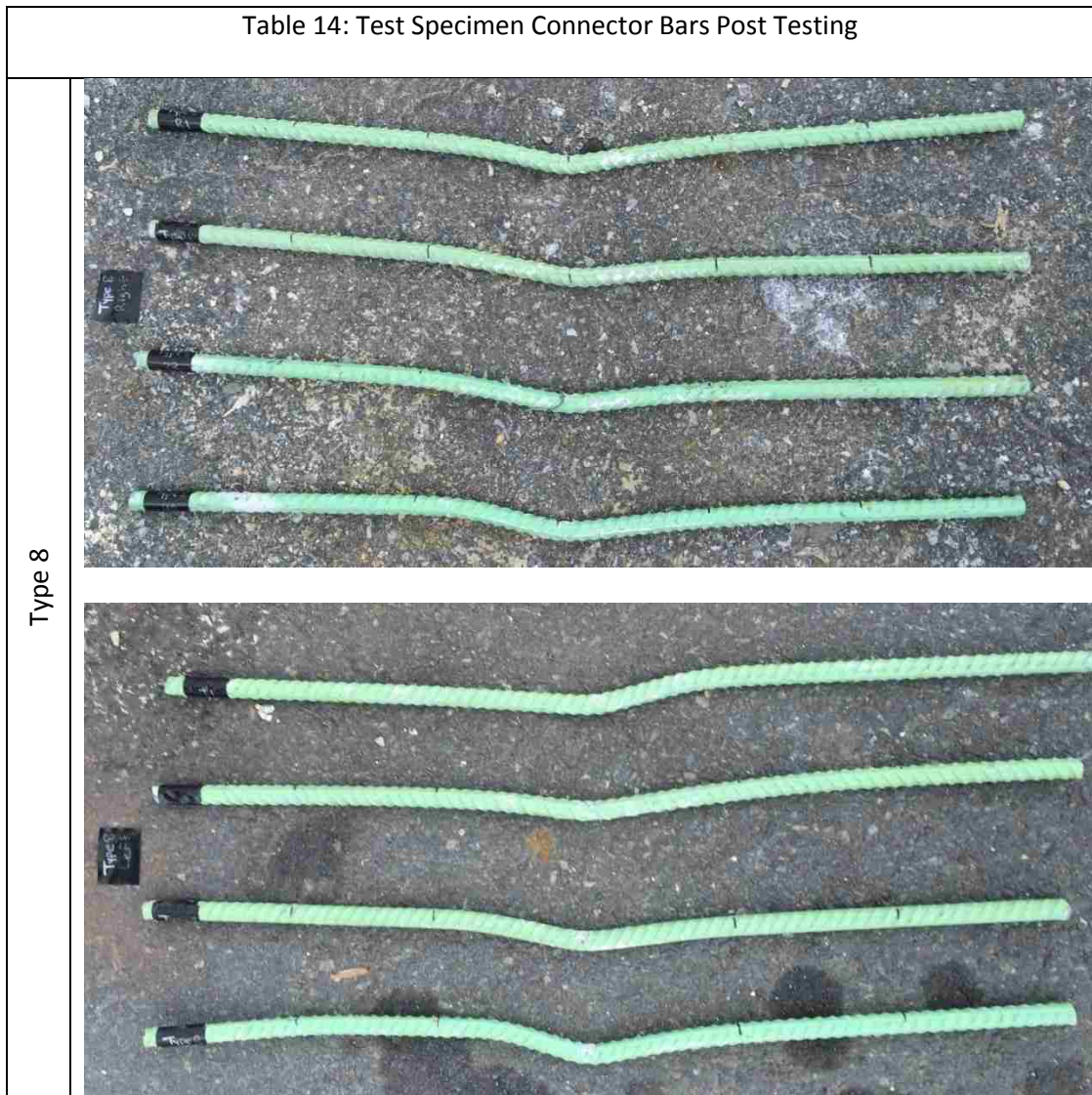


Type 2

Table 14: Test Specimen Connector Bars Post Testing

Type 3	
Type 7	

Table 14: Test Specimen Connector Bars Post Testing



Upon examination of the connector plate it was determined that the holes in the steel plates were not damaged during testing. Therefore, at a connector thickness of 5/8" or greater yielding/fracture of the plate is not a concern for the FlexBeam system. It can also be observed, from the small pieces of concrete remaining in the holes of the connector plates, that concrete crushing occurred in the holes that had reinforcement passing through. For the Type 2 connector which had reinforcement passing through four of the eight holes, shearing of the concrete dowel can clearly be observed in the holes without bars. The shearing of the concrete dowel is evident by the cylindrical piece of concrete remaining in the connector hole. This verified

that concrete dowel action is engaged and shear failure of the concrete dowel is one of the failure mechanisms.

The inelastic damage states of the bars after testing were examined to assess the mechanisms present. The damaged bars showed that all bars, at minimum, yielded at the location where the bars passed through the connector holes. The larger diameter bars (#6) sustained less damage than the smaller diameter (#5) bars. The specimens that utilized a fewer number of bars showed higher levels of damage to the bars; in some cases fracture of the bar was observed. In specimens where bars were utilized in every connector hole, no fracture of the bars were observed in this sample set. It should be noted that in the Type 2 connector one of the bars was further damaged during the jack hammering and the bend of the bar was therefore altered. A comparison of the level of yielding damage undergone by the bars from the different test specimens is presented in Figure 49. The deformation observed in the bars was consistent with what is expected from a steel dowel subjected to double shear. The theoretical progression of a steel dowel subjected to double shear is presented in Figure 50.



Figure 49: Comparison of Test Specimen Connector Bar Damage

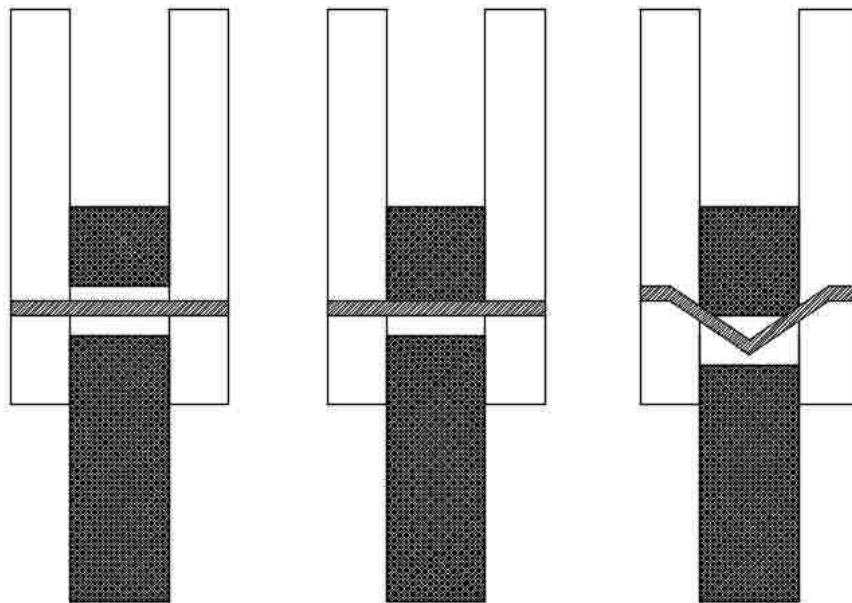


Figure 50: Dowel Progression Subjected to Double Shear

In some cases the test specimens regained strength past the level of the first peak load, for example the Type 7 connector. As a result the damage observed in the bars post testing is likely more severe than the damage that occurred at the time

of the first peak load. It is assumed based on the slip corresponding to the first peak load that any fracture of the bars occurred after the initial peak load was reached. In connectors that had reinforcement placed through every connector hole the failure at the initial peak load is attributed to a shear failure mechanism where at this load initial yield of the steel dowel occurs. In connectors that had no reinforcement placed through any of the connector holes the failure at the initial peak load is attributed to a shear failure of the concrete dowel. In the event where reinforcement is only placed through select connectors holes it is assumed that the shear capacity of the connector is due to a combination of steel and concrete dowel action.

3.3.5. Comparison of Experimental Results to Analytical

Approaches

A number of analytical equations have been developed to approximate the shear capacity of plate connection composite systems. These analytical equations were developed based on experimental evaluations of the Perfobond connector. Although the Perfobond connector shares many similarities with the FlexBeam connector there are critical differences in the components that contribute to the overall capacity of the connectors. As a result additional approaches to estimate the shear capacity of the FlexBeam connector must be explored. The following section will examine analytical approaches for estimating the capacity of a FlexBeam connector, provide a comparison of the FlexBeam experimental capacity to the estimated capacity based on the analytical equations and establish a newly developed equation to approximate the shear capacity of the FlexBeam connector

3.3.5.1. Analytical Equations

The following section presents a number of different analytical equations developed to estimate the capacity of the Perfobond connector, as well additional approaches

to estimate the shear capacity of the FlexBeam connector. Equation 5 was proposed by Oguejiofor & Hosain (1993) based on experimental push out test results. This empirical equation accounts for the contribution of three factors to the overall resistance of the connector: (1) the bearing concrete resistance at the connector face, (2) the steel reinforcement bars in the concrete slab and (3) the concrete cylinders in shear that are formed through the connector holes.

$$Q = 0.590A_{cc}\sqrt{f'_c} + 1.233A_{tr}f_y + 2.871nd^2\sqrt{f'_c} \quad \text{Equation 5}$$

where Q is the shear capacity per rib connector (N); A_{cc} is the shear area of concrete per connector (which is the longitudinal area of slab minus the connector area) (mm^2); f'_c is the compressive strength of concrete (MPa); A_{tr} is the total area of transverse reinforcement (mm^2); f_y is the yield strength of reinforcement (MPa); n is the number of rib holes; d is the diameter of the connector holes (mm).

Equation 6 (Oguejiofor & Hosain,1997; Oguejiofor & Hosain,1994) was proposed by Oguejiofor & Hosain as modification to Equation 5 based on numerical analysis of push out tests with the Perfobond connector.

$$Q = 4.50h_{sc}t_{sc}f_{ck} + 0.91A_{tr}f_y + 3.31nd^2\sqrt{f_{ck}} \quad \text{Equation 6}$$

where h_{sc} is connector height (mm); t_{sc} is the connector thickness; f_{ck} is concrete compressive strength in cylinder (MPa).

Equation 7 was proposed by Verissimo et al. and presented in (Martins, Costa-Neves & Vellasco, 2010; Ahn et al. 2010). The equation was developed based on experimental push out tests for a modified Perfobond connector. This shear connector used indented cut outs (symmetric cut with trapezoidal saliences and re-entrant angles) as opposed to a circular hole.

$$Q = 4.04 \frac{h_{sc}}{b} h_{sc} t_{sc} f_{ck} + 2.37 n d^2 \sqrt{f_{ck}} + 0.16 A_{cc} \sqrt{f_{ck}} + 31.85 * 10^6 \left(\frac{A_{tr}}{A_{cc}} \right) \quad \text{Equation 7}$$

where b is the axial spacing of two connectors placed side by side and all other variables have been previously defined.

Equation 8 and Equation 9 were proposed by Ushijima et al. (2001) for Perfobond connectors with reinforcing bars through the connector holes and without reinforcing bars through the connector holes, respectively. The equations were developed based on the results of a multi-linear regression analysis of experimental data. It should be noted that Equation 8 and Equation 9 provide the shear capacity per rib hole.

$$Q_{hole} = 1.45 [(d^2 - D_{st}^2) f_{cu} + D_{st}^2 f_{st}] - 26.1 \times 10^3 \quad \text{Equation 8}$$

with $51.0 \times 10^3 < (d^2 - D_{st}^2) f_{cu} + D_{st}^2 f_{st} < 488.0 \times 10^3$

$$Q_{hole} = 3.38 d^2 \sqrt{t/d} f_{cu} - 39.0 \times 10^3 \quad \text{Equation 9}$$

with $22.0 \times 10^3 < d^2 \sqrt{t/d} f_{cu} < 194.0 \times 10^3$

where Q_{hole} is the shear strength per hole of the connector (N); t is the connector thickness (mm); f_{cu} is the concrete cylinder compressive strength (N/mm²); d is the connector hole diameter; D_{st} is the reinforcement diameter (mm); f_{st} is the reinforcement tensile strength.

Equation 10 was proposed by Ahn et al (2010) based on experimental push out tests of the Perfobond shear connector. This equation was developed as a modified shear capacity equation that considers the Perfobond-rib arrangement, including the rib height and spacing.

$$Q = 3.14 h_{sc} t_c f_{ck} + 1.21 A_{tr} f_y + 3.79 n \pi (d/2)^2 \sqrt{f_{ck}} \quad \text{Equation 10}$$

where the variables have been previously defined.

Equation 11 and Equation 12 estimates the shear capacity of the connector based on the assumed capacity of a dowel in double shear. Equation 11 is applicable when accounting for steel dowel action which is the case when rebar is passed through the holes of the connector. Although there are three mechanisms that contribute to steel dowel action: flexural, shear and kinking, only the shear mechanism is considered for this approximation. In this equation the shear yield stress is determined based on the von Mises yield criteria. Additionally, the shear force due to friction is neglected. Equation 12 was developed by Leonhardt et al., 1987 based on experimental testing of the Perfobond connector and is applicable when accounting for concrete dowel action.

$$Q = 2 \frac{n_{bar} A_{bar} f_y}{\sqrt{3}} \quad \text{Equation 11}$$

$$Q = 2n_{hole} \frac{\pi d^2}{4} 1.6f'_c \quad \text{Equation 12}$$

Where Q is the shear capacity of the connector (kip); n_{bar} is the number of reinforcing bars passing through holes in the connector; A_{bar} is the area of the reinforcing bars (in²); f_y is the yield strength of reinforcement (ksi), f'_c is the compressive strength of concrete (ksi), n_{hole} is the number of holes without reinforcement in the connector, d is the diameter of the connector hole.

The analytical equations presented for shear capacity approximations of composite connectors are summarized in Table 15. For all equations Q is the total shear force per connector.

Table 15: Shear Capacity Equations	
Equation	Shear Capacity
Equation 5	$Q = 0.590A_{cc}\sqrt{f'_c} + 1.233A_{tr}f_y + 2.871nd^2\sqrt{f'_c}$
Equation 6	$Q = 4.50h_{sc}t_{sc}f_{ck} + 0.91A_{tr}f_y + 3.31nd^2\sqrt{f_{ck}}$
Equation 7	$Q = 4.04\frac{h_{sc}}{b}h_{sc}t_{sc}f_{ck} + 2.37nd^2\sqrt{f_{ck}} + 0.16A_{cc}\sqrt{f_{ck}} + 31.85 * 10^6\left(\frac{A_{tr}}{A_{cc}}\right)$
Equation 8	$Q_{hole} = 1.45[(d^2 - D_{st}^2)f_{cu} + D_{st}^2f_{st}] - 26.1 \times 10^3$ with $51.0 \times 10^3 < (d^2 - D_{st}^2)f_{cu} + D_{st}^2f_{st} < 488.0 \times 10^3$
Equation 9	$Q_{hole} = 3.38d^2\sqrt{t/d}f_{cu} - 39.0 \times 10^3$ with $22.0 \times 10^3 < d^2\sqrt{t/d}f_{cu} < 194.0 \times 10^3$
Equation 10	$Q = 3.14h_{sc}t_{sc}f_{ck} + 1.21A_{tr}f_y + 3.79n\pi(d/2)^2\sqrt{f_{ck}}$
Equation 11	$Q = 2\frac{n_{bar}A_{bar}f_y}{\sqrt{3}}$
Equation 12	$Q = 2n_{hole}\frac{\pi d^2}{4}1.6f'_c$

3.3.5.2. Comparison of analytical equations and experimental results

The equations presented in the previous section were applied to approximate the shear capacity of the FlexBeam connectors. The accuracy is assessed relative to the measured response. The material properties for f'_c and f_y used in the analytical equations are based on the actual properties of the test specimen, which were previously presented in Table 8 and Table 9. The experimental and analytical shear capacity estimates are presented in Table 16. The ratios of predicted strength to experimental capacity for each connector type and equation are presented in Table 17 and the mean values for all connector types are presented in Table 18, where a value over one represents an overestimation of capacity.

Table 16: Comparison of experimental and analytical shear capacity										
	Experimental [kip]	Eq. 6 [kip]	Eq. 7 [kip]	Eq. 8 [kip]	Eq. 9 [kip]	Eq. 10 [kip]	Eq. 11 [kip]	Eq. 12 [kip]	Eq. 13 [kip]	
Connector Type	1	90	265	177	123	n/a	118	184	n/a	217
	2	138	373	257	162	247		290	209	
	3 (1)	200	482	337	200	377	n/a	397	203	n/a
	3 (2)	198	469	326	192	362	n/a	388	203	n/a
	3b (1)	270	482	337	200	413	n/a	397	203	n/a
	3b (2)	272	469	326	192	399	n/a	388	203	n/a
	4	54	237	149	104	n/a	64	159	n/a	96.5
	6	189	449	305	181	306	n/a	369	203	n/a
	7	105	338	223	139	181	n/a	261	102	n/a
	8 (1)	241	592	416	241	481	n/a	509	280	n/a
	8 (2)	255	592	416	241	481	n/a	509	280	n/a
	9	135	419	283	172	241	n/a	342	140	n/a

Table 17: Ratio of predicted strength to experimental capacity									
	Eq. 6 [kip]	Eq. 7 [kip]	Eq. 8 [kip]	Eq. 9 [kip]	Eq. 10 [kip]	Eq. 11 [kip]	Eq. 12 [kip]	Eq. 13 [kip]	
Connector Type	1	2.94	1.97	1.37	n/a	1.31	2.04	n/a	2.43
	2	2.70	1.86	1.17	1.17		2.10	1.17	
	3 (1)	2.41	1.69	1.00	1.89	n/a	1.99	1.02	n/a
	3 (2)	2.37	1.65	0.97	1.83	n/a	1.96	1.03	n/a
	3b (1)	1.79	1.25	0.74	1.53	n/a	1.47	0.75	n/a
	3b (2)	1.72	1.20	0.71	1.47	n/a	1.43	0.75	n/a
	4	4.39	2.76	1.93	n/a	1.19	2.94	n/a	1.79
	6	2.38	1.61	0.96	1.62	n/a	1.95	1.07	n/a
	7	3.22	2.12	1.32	1.72	n/a	2.49	0.97	n/a
	8 (1)	2.46	1.73	1.00	2.00	n/a	2.11	1.16	n/a
	8 (2)	2.32	1.63	0.95	1.89	n/a	2.00	1.10	n/a
	9	3.10	2.10	1.27	1.79	n/a	2.53	1.04	n/a

Table 18: Mean ratio of predicted strength to experimental capacity								
	Eq. 6 [kip]	Eq. 7 [kip]	Eq. 8 [kip]	Eq. 9 [kip]	Eq. 10 [kip]	Eq. 11 [kip]	Eq. 12 [kip]	Eq. 13 [kip]
Mean for all connector types	2.65	1.80	1.12	1.69	1.22	2.08	1.01	1.40

The equations developed for the Perfobond connector (Equation 5, Equation 6, Equation 7, Equation 8, Equation 9, Equation 10 and Equation 12) consistently overestimate the shear capacity of the FlexBeam connector. One of the reasons for this overestimation is attributed to the contribution of end bearing to the overall capacity that is present in the Perfobond connector and not in the FlexBeam connector. The contribution of the end bearing component can be seen clearly in Equation 5, Equation 6, Equation 7 and Equation 10 and although not as clear in Equation 8 and Equation 9 most likely influenced the constants determined from the multi-linear regression analysis. Additionally, it appears that Equation 5, Equation 6 and Equation 10 overestimate the contribution of the transverse reinforcement to the overall shear capacity. These three equations account for all transverse reinforcement present in the deck slab in the calculation when it is clear from the experimental testing of the FlexBeam connector that the transverse reinforcement running through the connector contributes significantly more to the overall capacity than the additional layer of transverse reinforcement.

As a means to approximate the shear capacity without using equations specific to the Perfobond connector Equation 11 was utilized. Equation 11 approximates the capacity of the connector by using the von Mises yield criteria for a steel dowel in double shear. This equation is only applicable in cases where the connector has rebar running through all the holes, as it provides no means to account for the contribution of the concrete shear dowel. In addition the equation does not account for frictional effects, concrete strength, and concrete in the shear plane.

Equation 12, estimates the shear capacity of the connector assuming concrete dowel action subjected to double shear. This equation does not account for any contribution of the steel dowel and therefore is only applicable in situations where holes without rebar are utilized in the connector. Equation 12 was developed using

test data from Perfobond connector tests, therefore the shear strength factor of 1.6 is not appropriate for the FlexBeam connector, which is why the equation over predicts the connector strength. For connectors with both holes with steel and concrete dowels Equation 11 and Equation 12 can be combined to approximate the capacity of the shear connector.

3.3.5.3. Development of FlexBeam Shear Equation

Based on the poor accuracy of the available equations it was determined that a modified equation for shear capacity of a FlexBeam connector is needed. Failed specimens were forensically examined to see if any failure modes could be identified. Removal of the connector plate from the Type 2 specimen confirmed that concrete dowel action contributes to the overall strength of a connector when holes without reinforcing are used. It was determined that the concrete dowels failed in shear based on the fact that the concrete remaining in the holes was completely intact. Upon investigation of the reinforcing bars passing through the connector holes most bars were found deformed at the location of the connector hole. In some cases reinforcing bars were found to have fractured near the location of the connector hole. In all cases the observed rebar deformation was consistent with the deformation expected for a steel dowel placed in double shear (see Figure 50). Based on these observations it was determined that the double shear dowel mechanism is the controlling mechanism for the FlexBeam connector.

The experimental results indicate that for FlexBeam connections utilizing steel dowels in all connector holes the first peak load corresponds to initial yield of the reinforcing bars. This conclusion is based on the fact that the first peak load corresponds closely with the predicted shear capacity based on the von Mises yield criteria for a steel dowel, as well as the observed yielding damage of the bar. In connectors where only connectors holes are utilized the experimental results

indicate that first peak load corresponds to a concrete dowel failing in shear. Based on the experimental indications of the failure mechanism a design equation will be developed to approximate the load at which initial yield of the bars occurs and the load at which the concrete dowel will fail in shear based on the FlexBeam connector details.

First, examining the contribution of the concrete dowel, experimental testing of the Perfobond connector concluded that the overall shear capacity can be estimated by taking the area of the hole multiplied by a shear strength parameter. This is then multiplied by 2.0 due to the fact that there are two shear planes. This concept is presented in a previously developed equation for the perfobond system (Equation 12), where the shear strength developed in the concrete is given by the shear strength parameter of 1.6 times the concrete strength. One reason this equation does not accurately predict the capacity of the FlexBeam system is due to the selected shear strength parameter. The shear strength parameter is dependent on the properties of the connector system including confining stress, hole size, hole spacing and end bearing condition. As illustrated for the Type 1 connector the shear strength parameter also varies as force is applied (Figure 51). The goal is to identify an applicable shear strength parameter, which will be referred to as the shear force capacity factor, that can accurately predict the capacity at which the concrete dowel fails in shear for a FlexBeam connector.

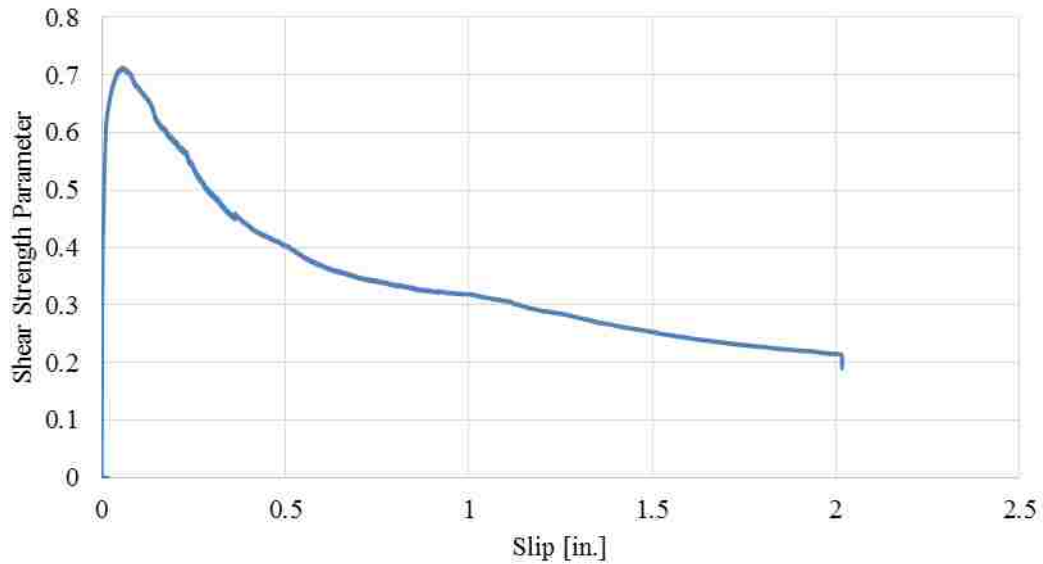


Figure 51: Shear Force Capacity Factor for Concrete Dowels

Since the steel rebar passing through the connector is also failing in shear a similar approach can be used to quantify the capacity of a connector that utilizes reinforcing through the connector holes. In this case the capacity of the steel dowel can be approximated as the area of the rebar multiplied by the yield strength of the rebar times a shear force capacity factor. This value would also be multiplied by two because of the double shear plane. The shear force capacity factor essentially relates the shear strength developed in the reinforcing bar to the uniaxial yield strength. It is expected that the steel dowel shear force capacity factor developed for the FlexBeam connection be in the range of 0.50 – 0.577, which correlates to the Tresca and von Mises theoretical shear yield failure predictions. Appropriate shear force capacity factors for both concrete dowel action and steel dowel action in the FlexBeam system need to be established so that a more accurate strength prediction equation can be developed. A procedure to establish these shear force capacity factors is presented.

For the application of the steel dowel there were seven tests performed in which there were straight reinforcing bar through all the connector holes: Type 3(1), Type

3(2), Type 6, Type 7, Type 8(1), Type 8(2) and Type 9. These tests were used to develop the shear strength parameter for the steel dowel in the FlexBeam system. These tests included connectors with a 1 inch and 1.5 inch diameter connector hole, 6 and 12 inch hole spacing as well as #5 and #6 rebar. The variation of the shear force capacity factor for each connector is shown in Figure 52 and the value of this factor at the first peak load, which is assumed to correspond to the initial yield of the reinforcement, is summarized in Table 19. The mean, standard deviation and coefficient of variation of the steel dowel shear strength parameter is presented in Table 20. From the coefficient of variation it can be seen that there is little dispersion in the data so utilizing the mean value shear strength parameter in this case can be justified.

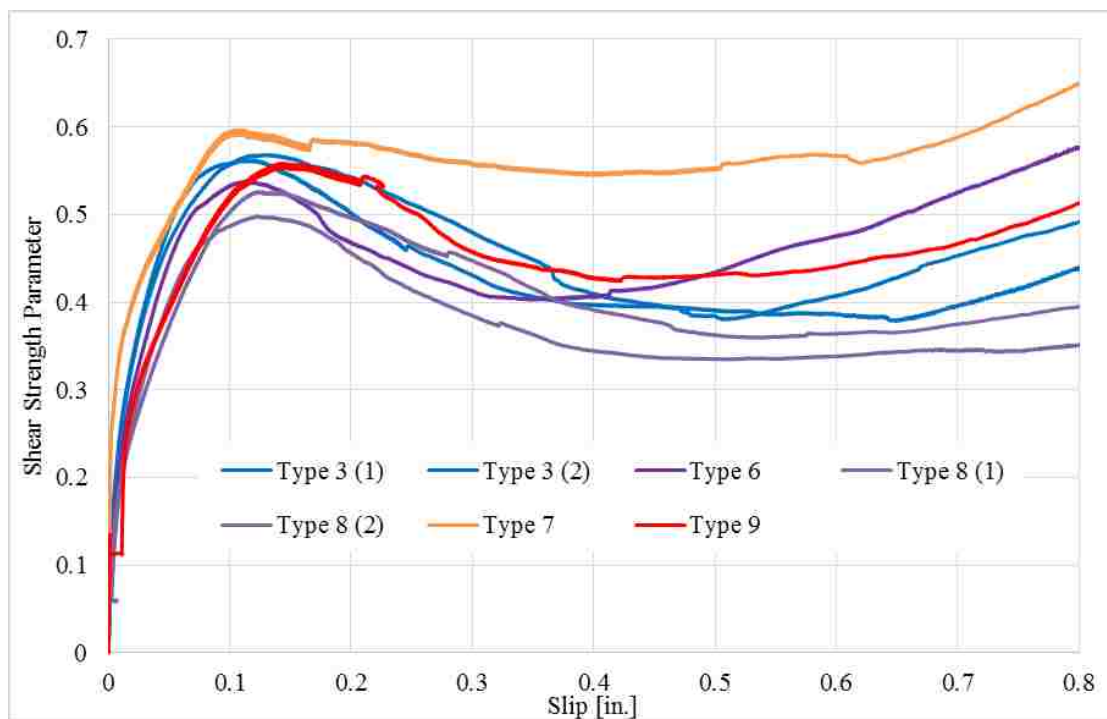


Figure 52: Shear Force Capacity Factor for Steel Dowels

Connector Type	Shear Strength Parameter at Peak
Type 3(1)	0.568
Type 3(2)	0.562
Type 6	0.538
Type 8 (1)	0.498
Type 8 (2)	0.526
Type 7	0.597
Type 9	0.559

Mean Shear Strength Parameter at Peak	Standard Deviation of Shear Strength Parameters	Coefficient of Variation
0.55	0.032	0.058

Examining the results for the shear force capacity factor at peak, variations can be seen between the different connector types. This is due to the effect of varying the details of the connector. For example comparing Type 3 and Type 8 shows the effect of changing the rebar from a #5 to a #6. To select a single value to use as the shear force capacity factor for the FlexBeam connector two approaches were considered: one is based on the five percent fractile method presented in ACI 318 for embedded anchors and the other utilizes the application of a safety factor to the mean value.

As defined in ACI 318-11 the five percent fractile is a statistical term meaning that there is a 90% confidence that there is a 95% probability of the actual strength exceeding the nominal strength. Equation 13 presents the method to obtain the five percent fractile value (ACI 355.2-07).

$$SF_{5\%} = SF_m(1 - K \cdot v)$$

Equation 13

where SF_m is the mean shear strength parameter, K is factor for one-sided tolerance limits for normal distribution and corresponds to a 5% probability of non-exceedance with a confidence of 90%, and v is coefficient of variation. For the case of 7 tests $K=2.894$ (ACI 355.2-07).

The second approach to calculate the nominal capacity involves taking the average of the results of all seven tests and utilizing a strength reduction factor. Since there are two approaches to calculate the required shear capacity, the discrete shear capacity and the average shear capacity, two different strength reduction factor are utilized. In the case of discrete shear capacity a strength reduction factor of 0.9 is applied as this approach is based on Strength I loading, which is an ultimate loading condition. When the average shear capacity is used the traditional strength reduction factor for shear of 0.75 is used.

Table 21 compares the average experimental shear force capacity factor with the reduced shear force capacity factors calculated by applying the 5% fractile method and strength reduction factors. The reduction from the average shear strength parameter can be seen graphically in Figure 53, here it is clear that all peak values occur at or above both the five percent fractile and mean value strength reduction factor threshold. It is recommended for design purposes that the mean shear force capacity factor be used and the appropriate strength reduction factor be utilized when calculating the nominal shear strength capacity of the system.

Table 21: Shear Force Capacity Factor Steel Dowel			
Average Experimental	5% Fractile	0.75 x Avg. Experimental	0.90 x Avg. Experimental
0.55	0.46	0.413	0.495

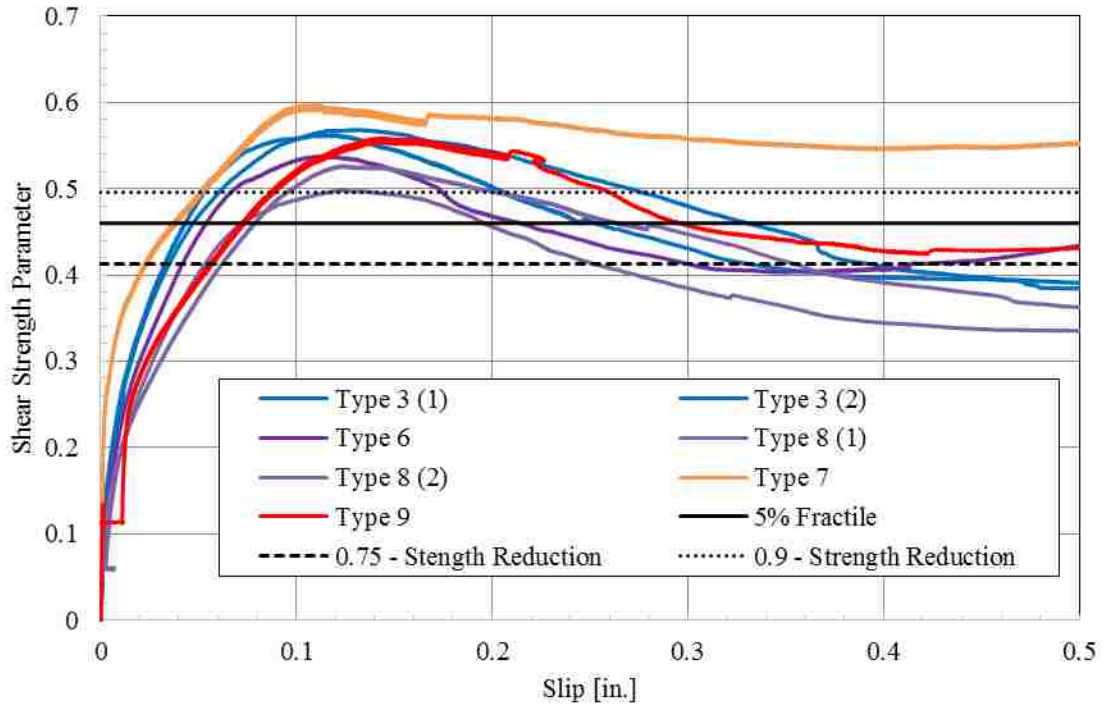


Figure 53: Steel Dowel Shear Strength Parameter Thresholds

The contribution to the overall shear capacity of the FlexBeam connector from the steel shear dowel component is presented in Equation 14.

$$Q_{sd} = 2n_{bar}A_{bar}SF_{sd}F_y \quad \text{Equation 14}$$

where Q_{sd} is the shear strength due to contribution of steel dowels (kip), n_{bar} is the number of holes with rebars passing through the connector holes, A_{bar} is the area of the bar (in^2), SF_{sd} is the mean shear force capacity factor for steel dowels (0.55 based on the experimental data) and F_y is the yield strength of the reinforcing (ksi).

For the case of concrete dowel action only two tests were performed in which the connector capacity was purely attributed to the concrete dowels, meaning no rebar was passed through the connector holes. The Type 1 and Type 4 connectors utilized 1.5 and 1 inch connector holes respectively. The variation of the shear force capacity factor for each connector is shown in Figure 54 and factor at the first peak load is summarized in Table 22.

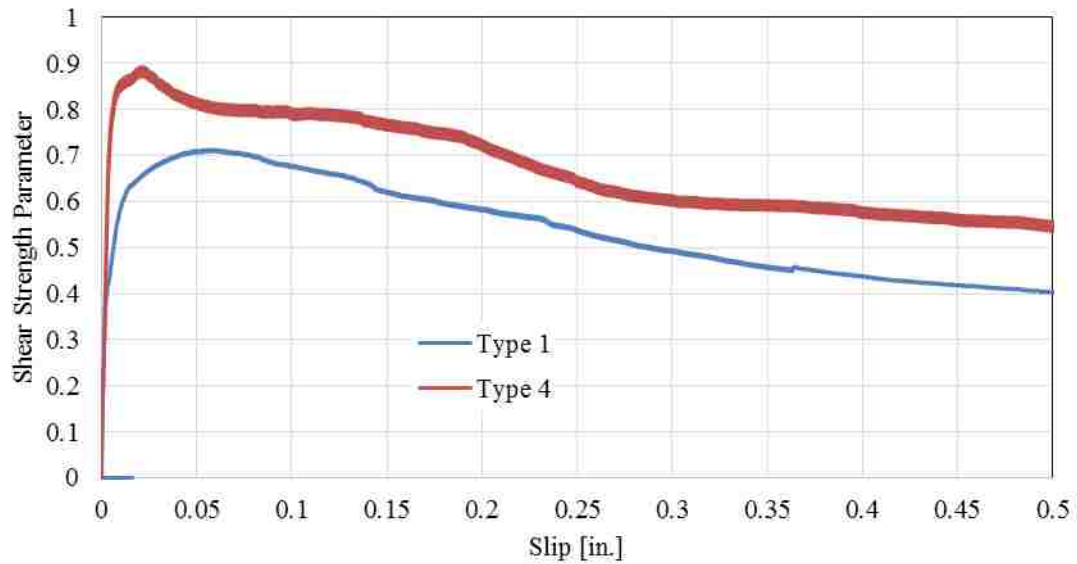


Figure 54: Shear Force Capacity Factor for Concrete Dowel

Connector Type	Shear Force Capacity Factor at First Peak
Type 1	0.713
Type 4	0.892

The five percent fractile method is not applicable when only two sets of data are available; therefore a strength reduction factor will be applied to the shear force capacity factor. Due to the lack of test data, the shear force capacity factor from the Type 1 connector will be selected as the FlexBeam shear strength factor for concrete dowels to be conservative. The shear strength factor for the FlexBeam concrete dowel and the application of the strength reduction factors for shear are shown in Table 23.

Experimental	0.75 x Experimental	0.90 x Experimental
0.71	0.53	0.639

For design applications the appropriate strength reduction factor would need to be

applied to the experimental shear force capacity factor when determining the nominal shear capacity. The contribution to the overall shear capacity of the FlexBeam connector from the concrete shear dowel component is presented in Equation 15.

$$Q_{cd} = 2n_{hole}A_{hole}SF_{cd}f'_c \quad \text{Equation 15}$$

where Q_{cd} is the shear strength due to the contribution of concrete dowels (kip), n_{hole} is the number of holes with no rebar passing through in the connector holes, A_{hole} is the area of the hole (in²), SF_{cd} is the experimental shear force capacity factor for concrete dowels (0.71 based on the experimental data) and f'_c is the concrete compressive strength (ksi).

In some cases connectors with a combination of concrete and steel dowels are utilized. As a result the general equation to determine the nominal capacity of the FlexBeam connector is presented in Equation 16.

$$Q_{FB} = Q_{sd} + Q_{cd} \quad \text{Equation 16}$$

where Q_{FB} is the shear capacity of the FlexBeam connector (kip), Q_{sd} is the shear strength due to the contribution of steel dowels (kip) and Q_{cd} is the shear strength due to contribution of concrete dowels (kip).

The developed FlexBeam equation was utilized to predict the shear strength of the test specimens and compared to the experimental values. The results are presented in Table 24. The values in this table for both the FlexBeam equation and experimental testing do not include the use of a strength reduction factor. Additionally, the analytical approximations of capacity use the known material properties for the yield strength of the rebar and concrete compressive strength.

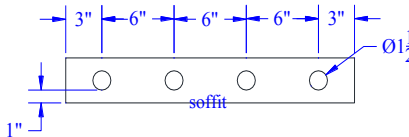
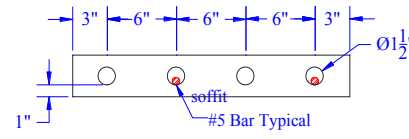
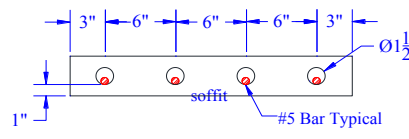
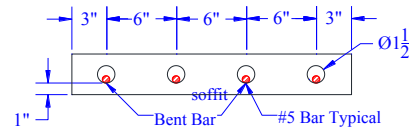
Table 24: FlexBeam Test Specimen Capacity Summary				
Connector Type	Description	Connector Schematic	FlexBeam Equation [kip]	Experimental First Peak [kip]
Type 1	Hole Size: 1.5" diameter Hole Spacing: 6" Hole Reinforcement: None		96	90
Type 2	Hole Size: 1.5" diameter Hole Spacing: 6" Hole Reinforcement: #5 bar at 12" spacing		145	138
Type 3	Hole Size: 1.5" diameter Hole Spacing: 6"		194	200
Type 3 (2)	Hole Reinforcement: #5 bar at 6" spacing		194	198
Type 3b	Hole Size: 1.5" diameter		194	270

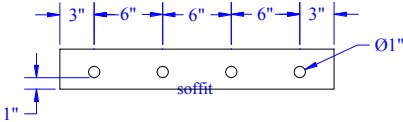
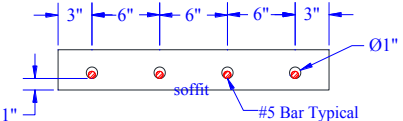
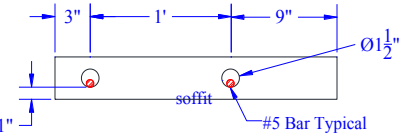
Table 24: FlexBeam Test Specimen Capacity Summary				
Connector Type	Description	Connector Schematic	FlexBeam Equation [kip]	Experimental First Peak [kip]
Type 3b (2)	Hole Spacing: 6" Hole Reinforcement: #5 straight bar at 12" spacing #5 bent bar at 12" spacing		194	272
Type 4	Hole Size 1" diameter Hole Spacing: 6" Hole Reinforcement: None		21	54
Type 6	Hole Size: 1" diameter Hole Spacing: 6" Hole Reinforcement: #5 bar at 6" spacing		194	189
Type 7	Hole Size: 1.5" diameter Hole Spacing: 12"		97	105

Table 24: FlexBeam Test Specimen Capacity Summary				
Connector Type	Description	Connector Schematic	FlexBeam Equation [kip]	Experimental First Peak [kip]
	Hole Reinforcement: #5 bar at 12" spacing			
Type 8	Hole Size: 1.5" diameter Hole Spacing: 6"		267	241
Type 8 (2)	Hole Reinforcement: #6 bar at 6" spacing		267	255
Type 9	Hole Size: 1.5" diameter Hole Spacing: 12" Hole Reinforcement: #6 bar at 12" spacing		133	135

The FlexBeam shear strength approximation equation (Equation 16) provides a conservative approach for predicting the nominal strength when utilizing the strength reduction factors. This can be observed by applying the appropriate strength reduction factor to the FlexBeam equations results in Table 24 and by the examination of the Type 2 connector performance. The test data for this connector type was not utilized in the development of the shear force capacity factors. The

Type 2 connector consists of a combination of concrete and shear dowels. The results using the discrete and average strength reduction factors for the steel dowel and concrete dowel, SF_{sd} , SF_{cd} are compared with the experimental results in Table 25.

Table 25: Nominal Strength Estimate			
Connector Type	Experimental (kip)	FlexBeam Equation Discrete Factor – 0.9 (kip)	FlexBeam Equation Average Factor – 0.75 (kip)
Type 2	138	130	108

These results indicate that the developed equation for the FlexBeam connector shear capacity is able to produce conservative estimates of the overall capacity for this connector. Utilizing the steel dowel shear force capacity factor developed based on the discrete formulation produced more accurate approximations, a 6% under approximation compared to 22% using the average strength force capacity factor. Given the limited number of experimental tests performed these initial shear strength parameters values were selected with the intention of producing conservative values. Additional testing and the use of finite element simulations may allow these shear parameters to be further refined resulting in better approximations of the overall shear capacity.

For design purposes it is often more practical to express the shear capacity of the connector in terms of shear flow or shear per unit length. Equation 14 and Equation 15 calculate the total shear capacity of the connector due to the contribution of the steel dowel and concrete dowels. These equations can be formulated to calculate the shear per unit length along the connector which is a more practical application in the design process where the number of bars and/or holes has not yet been

established. The shear flow equations are presented as Equation 17, Equation 18 and Equation 19.

$$q_{sd} = \frac{2A_{bar}SF_{sd}F_y}{s} \quad \text{Equation 17}$$

where q_{sd} is the shear strength per unit length due to contribution of steel dowels (kip/in), A_{bar} is the area of the bar (in²), SF_{sd} is the mean shear force capacity factor for steel dowels and F_y is the yield strength of the reinforcing (ksi) and s (in) is the center to center spacing of the connector holes.

$$q_{cd} = \frac{2A_{hole}SF_{cd}f'_c}{s} \quad \text{Equation 18}$$

where q_{cd} is the shear strength per unit length due to the contribution of concrete dowels (kip/in), A_{hole} is the area of the hole (in²), SF_{cd} is the experimental shear force capacity factor for concrete dowels and f'_c is the concrete compressive strength (ksi) and s (in) is the center to center spacing of the connector holes.

$$q_{FB} = q_{sd} + q_{cd} \quad \text{Equation 19}$$

where q_{FB} is the shear capacity of the FlexBeam connector per unit length (kip/in), q_{sd} is the shear strength per unit length due to contribution of steel dowels (kip/in) and q_{cd} is the shear strength per unit length due to contribution of concrete dowels (kip/in).

Although Equation 14 and Equation 15 have been shown to produce conservative shear capacity approximations for the FlexBeam test specimens it is important to understand the limitations of these equations. This equation was developed based on testing of FlexBeam connectors with 1 in. to 1.5 in. diameter connector holes, transverse rebar size of #5 or #6 bars, and a connector hole spacing of 6 to 12 in.

It is also assumed that the actual FlexBeam deck slab reinforcement layout is in line with that utilized in the test specimens. In general it is recommended that for the final system design a connector detail of 1.5 inch holes with steel dowels in every hole be used. Connector holes without reinforcement are not recommended to be used in the FlexBeam system. Unless further experimental testing is conducted the steel dowel equation should be limited to applications of a #6 bar or smaller. This limitation is based on the fact that larger bars have not been tested and the shear strength capacity factor appears to be decreasing with an increase bar size therefore the current recommended factor (0.55) may not be appropriate for larger bar sizes. Additionally, the equation developed for the concrete dowel is based on the very limited number of experimental test points. Although the developed concrete dowel equation does produce conservative approximations for the 1 and 1.5 inch diameter holes tested it is not recommended for strength predictions of other hole sizes until further experimental testing is conducted.

3.3.5.4. Utilizing Experimental First Peak Load for Design Capacity

The FlexBeam design equations (Equation 14, Equation 15 and Equation 16) used to predict the capacity of a connector were developed based on the first peak load of the generated experimental data. As observed in the experimental data presented in Figure 45, some connector types are able to regain strength past the first peak load. An increase in strength past the first peak load is only observed in some connector types where reinforcement is utilized through the connector holes. The fact that some reinforcing bars were able to fracture during testing shows that in certain connector types the shear force in the reinforcing was able increase past the initial yield of the bar. One reason may be attributed to the fact that these bars were able to stay anchored in the concrete slab for larger values of slip which allowed the force in the bar to continue to increase until either the bar fractured or the bar pulled out of the concrete due to spalling. The behavior of the connector is

not consistent or predictable after the initial peak load therefore any strength gain past the first peak load is not reliable for design purposes.

There are a number of reasons the first peak load was selected as the experimental shear capacity of the connector. First, the failure mechanism at this experimental peak load was found to be consistent with the prediction of initial yield of the steel dowels based on the comparison of the experimental and theoretical data as well as conclusions from previous research studies. The assumption that the concrete dowels fail in shear was also supported by the destructive evaluation. Second the design shear demand is determined based on the ultimate capacity of the system and the typical demands on the system due to service loading will be significantly less. In addition the FlexBeam shear design capacity is reduced by a strength reduction factors and the reduced value is taken as the shear capacity of the connector. Also the shear force capacity factors established for the FlexBeam design equation were developed based on the actual reinforcing yield strength and concrete strength compressive strength, where as the design values that will be used in the equation are inherently more conservative. Finally, the design of the FlexBeam system allows for redistribution of the shear throughout the length of the connection if one bar were to fail. The failure of the bar would also results in visual damage to the concrete deck which would provide warning signs that the system was distressed.

Full scale overload testing of the FlexBeam system will also be conducted before this system is put into place in the field. The system will be instrumented to verify the failure mechanism of the steel dowels. Connector holes without reinforcing are not currently recommended for use in the FlexBeam system at this point due to the low experimental capacities per connector hole. In addition only two experimental

tests were conducted utilizing only concrete dowel action and further experimental testing is recommended to verify the shear force capacity factor.

3.4. FlexBeam Final Prototype Design

3.4.1. Shear Transfer Design

Having established the experimental capacity and equation based approximation of connector strength, the prototype FlexBeam system can be designed. Based on the flexural analysis conducted during the previous phase of this project (Piran-Aghl, Naito, and Sause 2015) two steel sections were considered for the prototype design: WT 20 x 74.5 and WT 20 x 83.5. The lighter WT 20 x 74.5 was selected for as the section to be used for the prototype shear design. In order for the FlexBeam system to meet the shear transfer demands placed on the composite section a connector detail needs to be established. The interface shear demands will be computed using two approaches: (1) the shear demand for the Strength I load combination and (2) the ultimate strength shear demand corresponding to the ultimate flexural strength from a simplified estimate.

The horizontal shear demand along the length of the FlexBeam under the Strength I combination is calculated from the shear force envelope using the formulation presented in Equation 20.

$$q = \frac{VQ_t}{I_{short}} \quad \text{Equation 20}$$

in which Q_t is the first moment of the transformed (short-term elastic modulus) area of the concrete slab about the neutral axis of the short-term composite section, V is the shear force demand due to the Strength I combination, and I_{short} is the moment of inertia for the short-term composite section.

The ultimate strength horizontal shear demand was computed using a simplified estimate in accordance with AASHTO Article 6.10.10.4.2. This approach estimates the shear force demand based on a stress in the composite concrete deck of 0.85

f'_c at the section with maximum bending moment. This is a conservative approximation of the maximum compression force in the deck and does not necessarily represent the force in the deck when the flexural strength is achieved. This shear force is the total horizontal shear force that needs to be transferred between the concrete deck and steel beam section from the point of maximum moment to the point of contra-flexure. For the simply supported composite bridge beam this is the distance from the bearing to the axle of the design tandem (AASHTO 3.6.1.2.3), assuming the center of the axle spacing is located at midspan. In the case of the AASHTO design tandem the axle spacing is 4 ft, therefore the maximum moment occurs 23 ft from each end bearing. This approximate ultimate strength horizontal shear is assumed to be distributed uniformly over the length from the axle of the design tandem to the bearings. The shear demands using the Strength I and ultimate strength approach is presented in Figure 55.

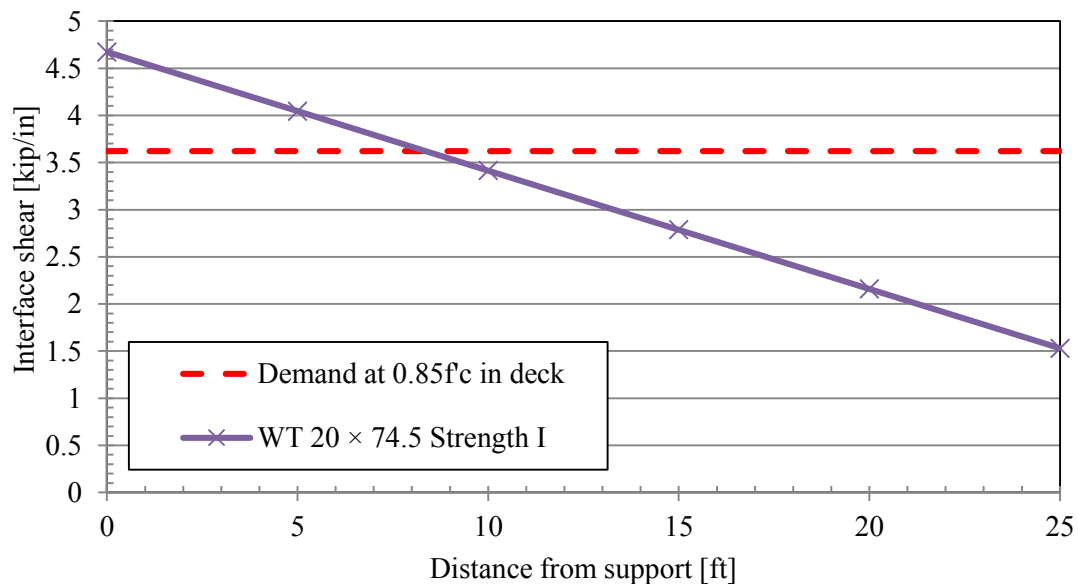


Figure 55: FlexBeam Shear Demands

In order to determine the shear capacity of the FlexBeam system the connector details need to be selected. The prototype design will utilize 1.5 in diameter holes

with #6 bars in every hole. The spacing of the holes will be determined based on the shear demand along the length of the beam. The connector strength is determined from the FlexBeam equation approximation (Equation 19).

When applying the FlexBeam equation for the design of the connector a strength reduction factor of 0.90 is used when accounting for the discrete connector strength and a strength reduction factor of 0.75 is used when computing the average strength. The less conservative strength reduction factor is used for the discrete case because there is less likelihood that the shear strength will be over estimated at any specific location. Additionally, conservative values for material properties are used in the design equation. In this case the minimum allowable concrete strength of 4000 psi and reinforcement yield strength of 60,000 ksi are used in the design. The connector details and connector strengths are presented in Table 26.

Table 26: FlexBeam Connector Details	
Hole Size [in.]	1.5
Bar Size	#6
Shear Factor (see Eq.11)	0.55
Discrete Strength Reduction Factor	0.9
Discrete Capacity [kip/dowel]	26.14
Average Strength Reduction Factor	0.75
Average Capacity [kip/dowel]	21.78

For this design, three different connector spacings were used in order to limit the complexity of fabrication. The system can be optimized by using more variations on the connector spacing and fabrication can be simplified by further limiting the

number of connector spacing changes allowed. This decision will ultimately be left up to the design engineer. Two different shear capacities will be presented: (1) discrete interface capacity and (2) average interface capacity. The discrete interface capacity is the shear capacity along the length of the beam and can be compared to the Strength I shear demand and the average interface capacity assumes the shear capacity to be uniformly distributed over the length of the beam and can be compared with the ultimate shear demand.

Using the shear strength estimate from the FlexBeam equation the number of required holes is estimated. The design is initially performed so that the discrete interface capacity meets the Strength I shear demand (see Figure 56). An average capacity of the FlexBeam is then calculated based on the connection design determined from the discrete capacity calculation. The average capacity is then checked against the average demand in the deck (see Figure 57). An estimated 50 holes with bars are needed over half the beam span to meet the FlexBeam equation capacity. The corresponding layout of holes and bars are illustrated in Figure 58. A higher number of shear holes are placed at the end of the beam in conjunction with the higher shear demands. Comparing the average interface capacity with the maximum expected demand in deck strength it can be seen that the proposed layout is conservative on average (see Figure 57). The locations of changes in the discrete capacity (Figure 56) are the locations at which the hole spacing is changed. The capacity at the end of the beam may appear to be over designed but this added capacity is due to the additional holes and rebar at the end block. Although a larger spacing here would result in a reduced over design at the end block, altering the spacing over such a small length would add unnecessary complexity to the fabrication so the spacing is kept constant for the first portion of beam length.

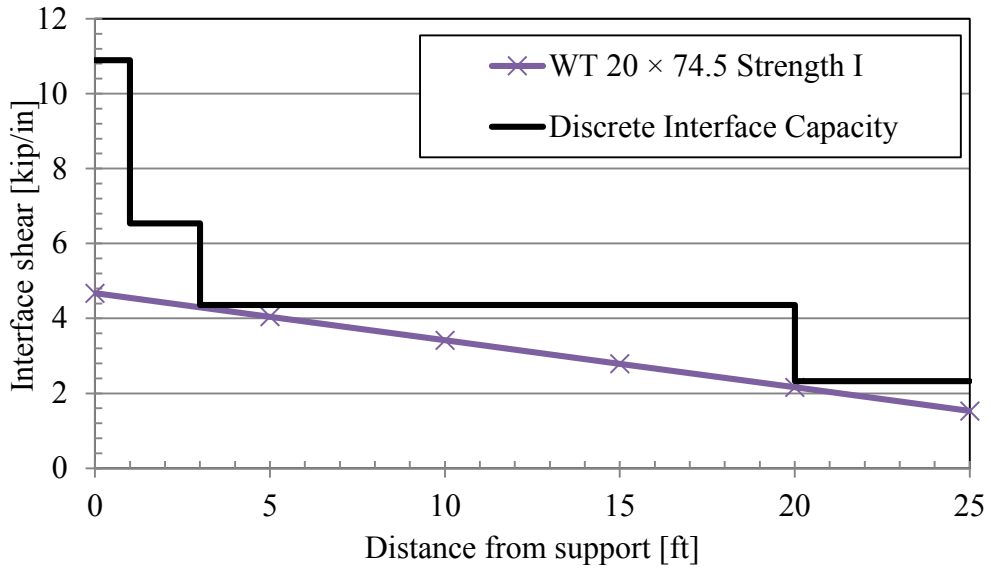


Figure 56: Discrete Interface Shear Capacity

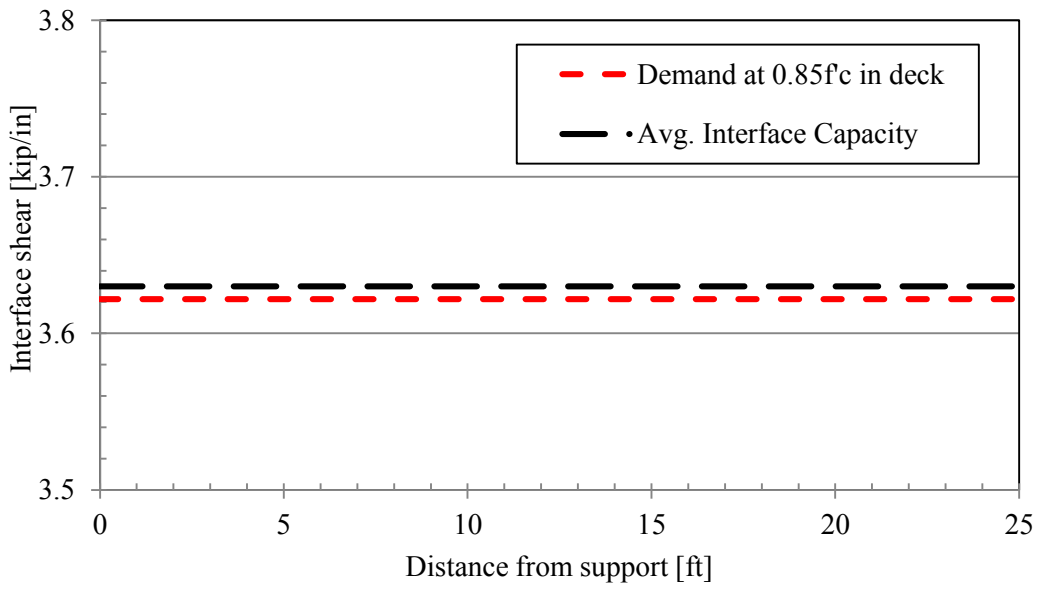


Figure 57: Average Interface Shear Capacity and Demands

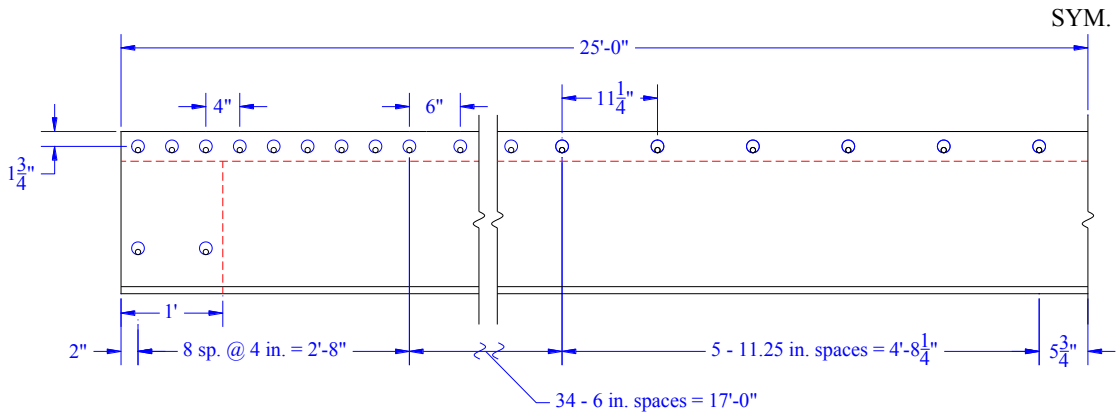


Figure 58: Proposed shear transfer detail for PA FlexBeam

3.5. Construction Methods

3.5.1. Steel Sections

The steel sections that will be utilized in the FlexBeam system are some of the largest rolled sections available. The W 40 x 149 and W 40 x 167 are only made by a small number of producers and are only rolled a limited number of times a year. This means that unless special orders are coordinated with these producers special attention must be paid to the rolling schedule of these shapes in order not to delay the project schedule.

Splitting of the wide flange sections will need to be performed by a PennDOT approved steel fabricator as the required WT sections cannot be acquired directly from the steel producers. Once the section is split the WT web may need to undergo a straightening process. This is something that will need to be assessed on a case by case basis. After any required straightening has been performed the section will then be cambered. The cambering technique may vary from fabricator to fabricator, but any cold cambering or heat cambering techniques must be done by PennDOT approved vendor according to PennDOT cambering specifications.

The determination of the required camber in the WT will be based on the specified final long term camber in the composite bridge system. Camber of the WT section is conventionally imparted with the beam on its side as illustrated in Figure 59. This orientation is referred to as the "no-load" camber. The terminology of no-load indicates that the camber does not account for gravity. Once the beam is completed and placed in a vertical orientation with the flange horizontal, the self-weight will be applied and a portion of the no-load camber will be lost.

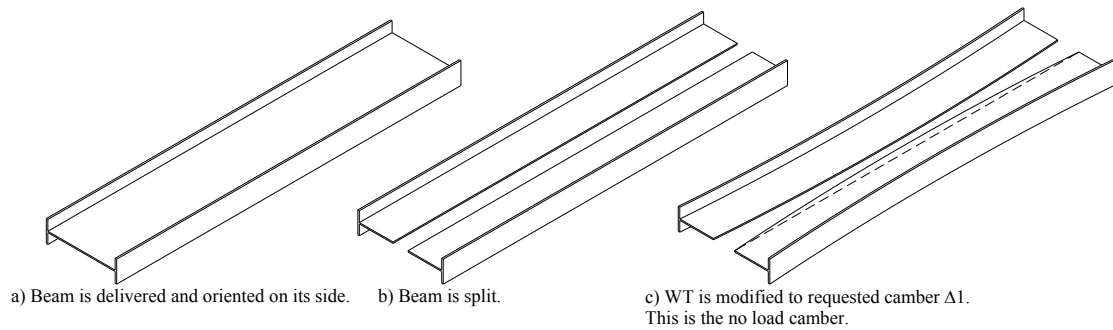


Figure 59: WT fabrication

3.5.2. Constructing the Concrete Deck

After the wide flange section is split the composite FlexBeam section can be cast. The WT section will be cambered following PennDOT specifications to a no-load camber profile designated by the engineer based on the desired final bridge profile. The WT section will then be placed on a three point support system as shown in Figure 60 and Figure 61(a). The ends of the WT will be simply supported and the midspan support will be set to a predetermined height equivalent to the specified no-load camber of the WT section. Due to camber tolerances (0 to +0.75 in.) variations in the WT camber profile of the WT sections can be expected. Using the proposed three point support set up for the WT section allows for the same initial profile all steel sections, thus allowing the deck profile and shoring to remain constant throughout the fabrication process.

There are three possible scenarios that need to be considered for the cambered steel section. The first scenario is that the midpoint camber of the WT is delivered with the specified no-load camber (excess no-load camber of 0 in.). In this case WT profile will not require any adjustment and the deck can immediately be cast. The second case is that the WT is delivered with an excess no-load camber less than or equal to the self-weight deflection of the WT section. In this case the WT section will be allowed to deflect under its own self weight until it comes in contact with the shoring at the middle support location. Once the beam is in contact with the middle

support the desired profile has been achieved and the deck can be cast. The third case is that the excess no-load camber is larger than the self-weight deflection and the midspan of the steel section needs to be pulled down to reach the level of the middle support (Figure 62). In this situation a jacking force will be applied to pull the center of the WT down until it is in contact with the shoring at the middle support at which point the deck can be cast.

The main reason for correcting camber errors in this manner is to achieve an initial steel profile that is common to all WT sections. This simplifies the process needed to form and cast the concrete deck. Allowing the steel profile to remain constant for all WT sections also allows the deck formwork profile to remain the same for each FlexBeam component. This is important because altering the formwork profile for different steel profiles would be time consuming and costly. Additionally, this ensures that the critical embedment depth of the WT stem into the concrete deck is achieved for all precast components. The concrete formwork will be fully shored so that during casting no weight will be placed on the steel WT section (Figure 60 and Figure 61 (b)). After the deck is cured the composite beam can be lifted from the formwork using a crane and delivered to the construction site (Figure 60 and Figure 61 (c)).

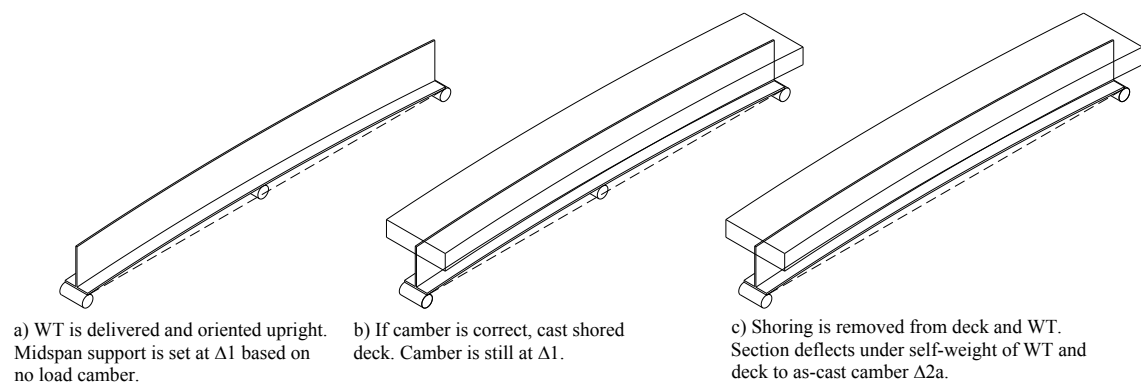


Figure 60: Construction case A

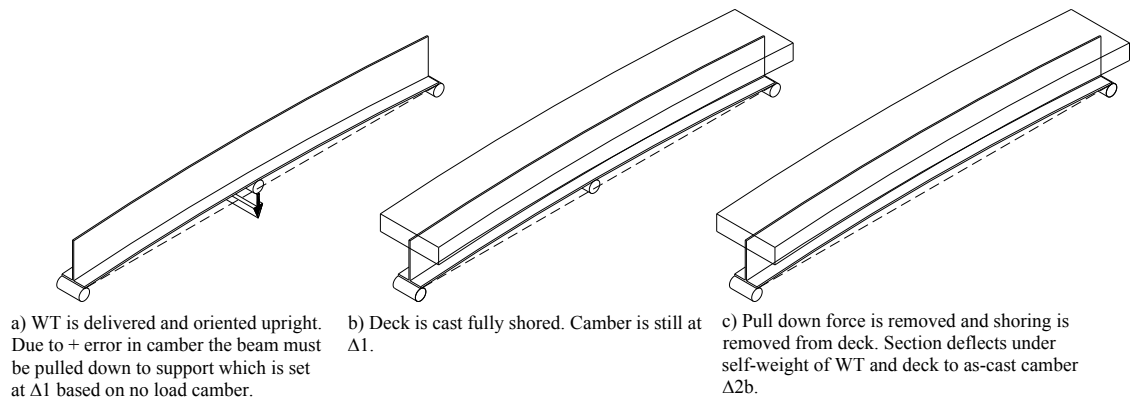


Figure 61: Construction case B

The process and assumptions used to calculate the desired no-load camber of the WT section are as follows. The first assumption is that because the WT and deck are shored during fabrication that the composite section will carry the self-weight of the WT and deck slab. In addition, any superimposed dead load is applied to the composite section and included in deflection calculations. Since the FlexBeam is a composite system, deflection calculations will need to be performed using a transformed section moment of inertia. Due to creep and other effects of the concrete, a long term and short term moment of inertia of the composite section must be calculated. The specified no-load camber of the beam equals the long term deflection of the composite system plus the desired final longitudinal profile of the bridge system.

Before the camber of the beam can be finalized the construction load stresses on the section need to be checked. These stresses will include the effect of construction dead load, superimposed dead load, live load and, if applicable, the applied pulldown force. To study the possible range of stresses that can be developed during fabrication two cases will be examined: (A) the WT is delivered with an excess no-load camber equal to 0" and (B) the WT is delivered with an excess no-load camber equal to the specified tolerance of + 0.75 in. For case A, all loads including the weight of the WT section, are assumed to act on the composite section. For case B,

it is assumed that the WT carries its own self weight and a pull down force is required. The self-weight of the deck, superimposed dead loads and construction live loads are all assumed to act on the composite section. When a pulldown force is required due to the excess camber of the WT, an equivalent "rebound force" will need to be applied on the composite section and included in the deflection calculations. These scenarios are illustrated in Figure 62. The limiting stresses during construction will be the compression stress at the top fiber in the deck which cannot exceed $0.6f'_c$ to prevent inelastic compression damage to the deck and the stress in the flange of the WT which cannot exceed the yield stress of the steel member. In these stress calculations it is advised to use the short term moment of inertia as this loading condition occurs only in the initial stages of the bridges lifespan.

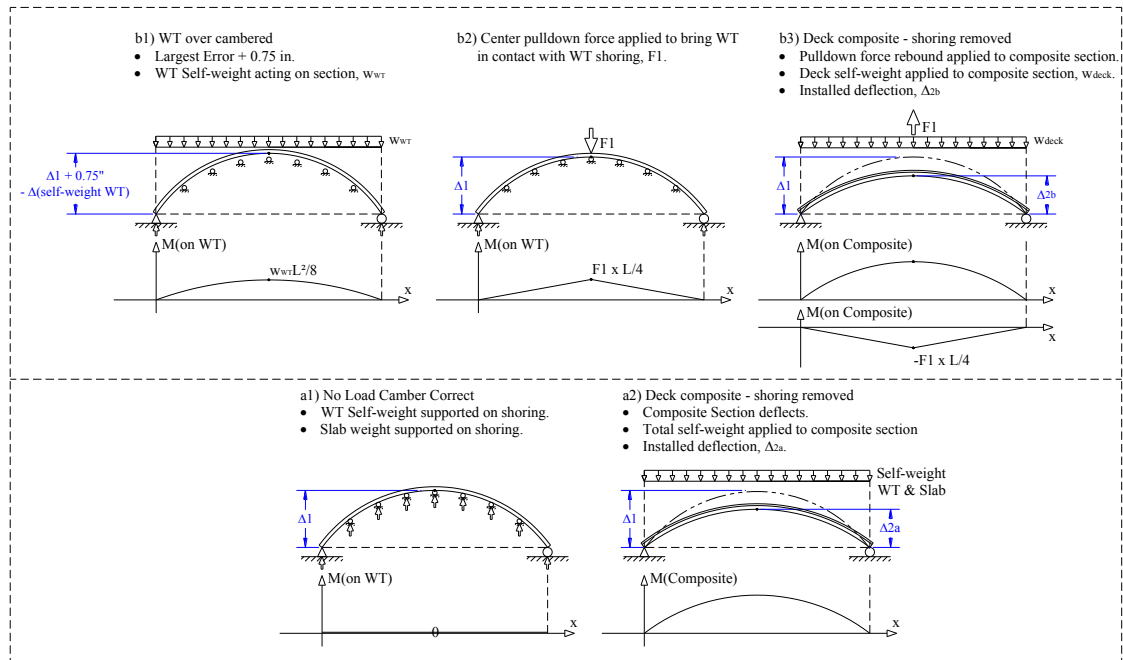


Figure 62: Stages of beam deformation

An analysis for the required camber of a WT 20 x 74.5 FlexBeam section based on the proposed construction method was conducted. A summary of the camber calculations for both the case A and case B conditions are presented in Table 27.

The specified camber of the WT is intended to provide a long-term longitudinal profile with the midspan elevation approximately 0.5 in. higher than the bearing elevations. In addition to camber calculations, the stresses developed in both case A and case B are compared with the limiting stress states in Table 28 and Table 29. Figure 63 indicates the locations of the stress given in the stress summary tables.

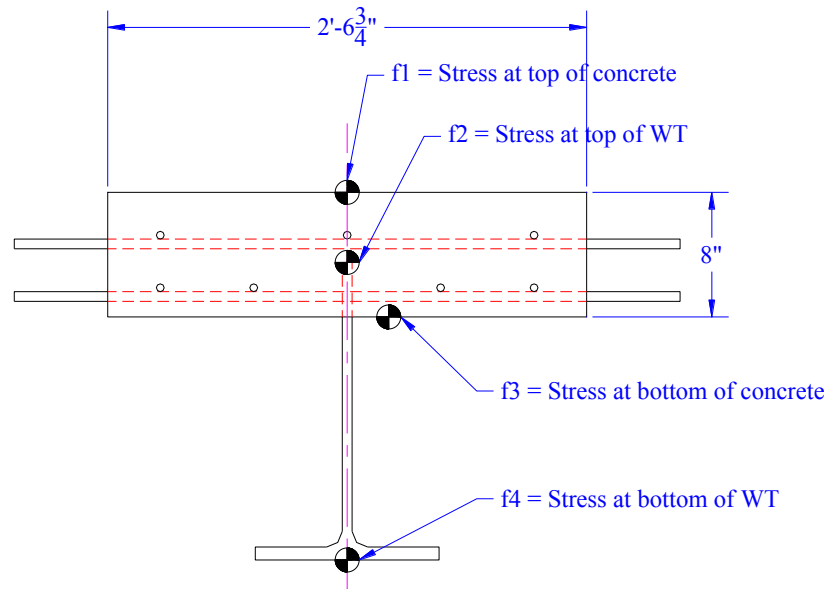


Figure 63: Section stress locations

Table 27: Camber Summary								
Case	Specified No-Load Camber of WT [in.]	Actual No-Load Camber of WT [in.]	Deflection of WT under Self Weight [in.]	Pulldown Force on WT [kip]	Pulldown Deflection of WT [in.]	Initial Rebound Deflection of Short-Term Composite Section [in.]	Total Dead Load Deflection of Long-Term Composite Section [in.]	Final Long-Term Longitudinal Profile Mid-Span Camber [in.]
A	1.5	1.5	NA	NA	NA	NA	0.968	0.532
B	1.5	2.25	0.443	1.61	0.307	0.102	0.820	0.782

Table 28: Case A Stress Summary				
Loading	f1 [ksi]	f2 [ksi]	f3 [ksi]	f4 [ksi]
Self-weight of WT non-composite	N/A	N/A	N/A	N/A
WT section under pulldown force	N/A	N/A	N/A	N/A
Composite section simply supported self-weight and super imposed dead load	-0.57	-2.33	-0.078	6.99
Composite section simply supported rebound	N/A	N/A	N/A	N/A
Construction Live Load	-0.23	-0.95	-0.032	2.84
Total Factored Construction Load Stress Case A	-1.01	-4.16	-0.14	12.44
Stress Limit	-2.40	50	-2.40	50

Table 29: Case B Stress Summary				
Loading	f1 [ksi]	f2 [ksi]	f3 [ksi]	f4 [ksi]
Self-weight of WT non-composite	NA	-4.68	NA	1.87
WT section under pulldown force	NA	-4.05	NA	1.62
Composite section simply supported self-weight and super imposed dead load	-0.48	-1.98	-0.066	5.93
Composite section simply supported rebound	0.075	0.31	0.01	-0.92
Construction Live Load	-0.23	-0.95	-0.032	2.84
Total Factored Construction Load Stress Case B	-0.83	-13.30	-0.11	14.14
Stress Limit	-2.40	50	-2.40	50

3.6. Construction Limit State Checks

In a typical steel girder design the nominal flexural strength of the section is the lowest value obtained according to the limit states of compression flange yielding, lateral torsional buckling, compression flange buckling, and tension flange yielding. During construction of the FlexBeam composite system the limit states of concern are defined as compression flange crushing, lateral torsional buckling, and tension flange yielding. The calculation of the limit state capacities and comparison with the construction load demands of the FlexBeam system are presented in this section.

3.6.1. Compression Flange Crushing and Tension Flange Yielding

During construction, the stresses in the FlexBeam components are limited those that would cause damage to the system. The stress in the WT section is limited to steel yielding. Stress in the composite section is limited to $0.6f'_c$ in the concrete compression flange and yielding of the tension flange. Damage of the compression flange is assumed to occur when the extreme fiber of the deck reaches a stress level of $0.6f'_c$. For the composite FlexBeam section the limit states and construction load demands for the controlling case where the WT was not delivered with excess cambered are presented in Table 30. The results demonstrate that during the construction phase the FlexBeam system will not reach crushing of the concrete deck and/or yielding of the tension flange of the WT.

Table 30: Compression Flange Cracking and Tension Flange Yielding of Composite Section			
Stress Demand Bottom of WT [ksi]	Tension Flange Yielding [ksi]	Stress Demand at Top Fiber in Deck [ksi]	Compression Flange Damage [ksi]
13.1	50	1.06	2.4

3.6.2. Lateral Torsional Buckling

Lateral torsional buckling is of concern at two stages of specimen construction: (1) when the WT section is erected on the support set up prior to deck casting, and (2) when the composite section is placed in the field prior to joint closure. For both cases the section is considered to be simply supported with a 50 ft span length. In the most extreme case of fabrication, due to camber tolerances, the WT section may be subjected to its own self weight and a pull down force. A lateral torsional buckling analysis is conducted and compared to the construction loading stresses induced by the self-weight and pull down force. For this analysis the equations in Section F9 of the AISC Steel Construction Manual (AISC, 2005) for lateral torsional buckling of WT sections can be applied. The limit states for lateral torsional buckling and flange local buckling are compared with the construction load demands on the WT section in Table 31. This analysis concludes that the WT section is not subjected to lateral torsional buckling during construction.

Table 31: Lateral Torsional Buckling of WT Section		
Moment Demand [kip-ft]	Lateral Torsional Buckling Limit State (Critical Moment [kip-ft])	Flange Local Buckling Limit State
54	128	*Section is compact, therefore limit state of flange local buckling does not apply

Once the deck is cast and cured the composite section needs to be analyzed to determine if the section is subjected to lateral torsional buckling during the erection of the individual FlexBeam components. This analysis is more complex as the formulas in AISC cannot be applied directly to a composite beam. Modified equations have been developed for a lateral torsional buckling of a section with a concrete compression flange and applied to the FlexBeam system. Equation 21 and Equation 22 present modified equations to calculate the effective radius of gyration

for lateral torsional buckling. The modular ratio is utilized to convert the portion of the steel web area in compression into an effective concrete section. Variable definitions presented in Section F3 of AISC will not be redefined in this section.

$$a_w = \frac{h_c t_w n}{b h_f} \quad \text{Equation 21}$$

$$r_t = \frac{b_{fc}}{\sqrt{12(1 + \frac{1}{6} a_w)}} \quad \text{Equation 22}$$

where n is the modular ratio (E_s/E_c)

The limit state yielding stress (F_y) and the inelastic lateral torsional buckling limit stress (F_L) need to be redefined since the compression flange is concrete. The yielding limit state is replaced by the limit state of concrete damage at the extreme fiber of the deck, where F_c is the corresponding stress defined in Equation 23. The inelastic lateral torsional buckling limit stress is defined to be the stress at the mid-height of the deck when the stress at the extreme fiber is equal to F_c and where the mid-height stress F_{Lc} is defined in Equation 24.

$$F_c = 0.6 f'_c \quad \text{Equation 23}$$

$$F_{Lc} = F_c \frac{(h - y' - h_f/2)}{(h - y')} \quad \text{Equation 24}$$

where y' is the distance to the neutral axis in the transformed section measured from the bottom.

As a result of redefining the limit state stress for yielding and inelastic lateral torsional buckling the limiting unbraced lengths also need to be redefined. The modified equations for the limiting unbraced length for yielding (L_{pc}) and inelastic lateral torsional buckling (L_{rc}) assuming the torsional constant J is taken as zero are presented in Equation 25 and Equation 26 respectively.

$$L_{pc} = 1.1r_t \sqrt{\frac{E_c}{F_c}} \quad \text{Equation 25}$$

$$L_{rc} = \pi r_t \sqrt{\frac{E_c}{F_{Lc}}} \quad \text{Equation 26}$$

The critical lateral torsional buckling stress, F_{cr} , depends on the unbraced length of the FlexBeam section. To determine the critical lateral torsional buckling stress for an unbraced length greater than the limiting unbraced length for inelastic lateral torsional buckling ($L_b > L_{rc}$) Equation 27 is used. The buckling stress for an unbraced length larger than the limiting length for yielding and less than or equal to the limiting unbraced length for inelastic lateral torsional buckling ($L_p < L_b \leq L_r$) can be computed using Equation 28.

$$F_{cr} = \frac{\pi^2 E_c}{\left(\frac{L_b}{r_t}\right)^2} \quad \text{Equation 27}$$

$$F_{cr} = F_c - (F_c - F_{Lc}) \left(\frac{L_b - L_{pc}}{L_{rc} - L_{pc}}\right) \quad \text{Equation 28}$$

To determine if lateral torsional buckling of the composite section occurs, the critical stress is compared with the stress at the mid-height of the deck. The system is analyzed under the application of self-weight superimposed dead load and construction live load. The assumption is made that no pull down force is applied. The results are summarized in Table 32. As noted, the demands on the composite section are well below the lateral torsional buckling limit state. Consequently, the section is not sensitive to lateral torsional buckling during erection and no transverse web stiffeners are needed.

Table 32: Lateral Torsional Buckling of Composite Section	
Stress Demand at Mid-Height of Deck [ksi]	Lateral Torsional Buckling Limit State Stress [ksi]
0.605	2.28

3.7. Future Work

The FlexBeam design equation was developed based on experimental testing of a limited number of test specimens. The developed shear capacity equation and prototype system shear design should be verified with full scale testing of the prototype FlexBeam components before this system is implemented in the field. As part of the full scale prototype testing the established fabrication and construction methods should be utilized. Any issues that arise during this process should be identified so that the required modifications to the established construction procedure can be implemented in future projects.

After the fabrication and construction methods are investigated the shear capacity of the FlexBeam prototype system will be verified. The system will be loaded to the design shear capacity to determine if the FlexBeam design equation can accurately predict the shear capacity of the system. Another aspect that will be verified during the full scale testing is the use of 4 inch hole spacing, which is a smaller spacing than was utilized for testing. Although this spacing is expected to achieve the same strength per hole as the 6 inch or greater spacing this still needs to be verified experimentally. Loading will continue until the system has reached the failure load. Observed damage of the system should be studied throughout loading to see if early warning signs of individual connector bar failure can be observed prior to the failure of the entire system.

Additional small scale experimental testing and/or FEM modeling should be conducted to investigate the effect of using larger bar sizes through the connector holes. At this point the FlexBeam steel dowel equation is limited to maximum bar size of #6 which is sufficient for the design a 50 ft .span but larger bar sizes may be useful in future system design. The concrete dowel equation was proposed based on very limited data points. This along with the low experimental per hole capacity

are the main reasons why the use of connectors with no bars is not currently recommended for the FlexBeam system. Further experimental testing or finite element analysis of connectors with different hole diameters can be used to establish a more reliable shear strength factor for this equation.

3.8. Conclusions and Contributions

This section summarizes the conclusions of this research effort and contributions made to the field of structural engineering. The result of this overall research effort is the development of an innovative composite highway bridge system which meets Pennsylvania design standards. The bridge system, called the FlexBeam system, utilizes a newly developed shear connection detail for which experimental testing was conducted and an analytical design equation to predict shear capacity was developed. As part of this research effort the required fabrication and construction methods to produce and erect the prefabricated FlexBeam components are presented. The results of this research effort has been published in an ATLSS report (Cercone, Naito and Sause, 2016).

It is recommended that FlexBeam systems are designed utilizing 1.5 inch holes with reinforcing bars in every hole, where the spacing of the holes is determined by the shear demands. At this point the use of connector holes without reinforcement is not recommended. It should also be noted that the FlexBeam equation has the following limitations based on the experimental data. The FlexBeam concrete dowel equation is limited by the connector hole size that is utilized. At this point it is only recommended for the approximation of hole diameters up 1.5 inch. The steel dowel equation is also limited by bar size and should only be applied to a bar size of #6 or smaller. Further testing is recommended to develop shear strength factors that include the effects of large bar and holes size; however, due to the fact that the reinforcement used in the connector is the same size as the bar used in the bottom layer of deck reinforcement the development of the equation to include the effect of larger bar sizes is not necessary at this time.

Summarized below are the major contributions of this research effort:

- A composite highway bridge system comprised of light-weight precast components was designed to meet PA standards for flexure and shear. The FlexBeam system was designed using a WT steel section cast into a concrete deck, where the stem of the WT was detailed to provide the shear connection in the composite system. The newly developed shear connection reduces material costs associated with traditional shear connector types that require welding to the top flange a wide flange section. In addition, the FlexBeam system will reduce the cost and time required for erection in the field. This can be attributed to the design of the light-weight precast FlexBeam segments that will reduce transportation and erection equipment costs typically associated precast systems.
- Utilizing WT sections, which can be unstable sections at long lengths, requires the section to be analyzed for the potential of lateral torsional buckling during fabrication and erection. Design equations are readily available for the lateral torsional buckling analysis of the steel WT section, however for the individual composite FlexBeam members a simplified approach to analyze for lateral torsional buckling was developed. Due to the fact that the composite section has a concrete deck, traditionally available lateral torsional buckling equations which were developed based on steel limit states cannot be applied directly to this system. As part of this research effort modified design equations utilizing concrete limit states were developed. Since this analysis is being performed for the construction state, stresses were limited to those that would cause damage in the concrete deck.
- A test specimen was designed to investigate the effect of different detailing parameters on the shear capacity of the FlexBeam connection. From this testing program experimental data was generated that captured the effect

of the connection detailing on the overall shear capacity of the FlexBeam connector. The detail parameters investigated for the FlexBeam connection included; hole size, reinforcement size, reinforcement spacing and the use of bent versus straight bars. The result of the experimental testing was that increasing the hole size, reinforcement size and using bent bars increased the shear capacity of the connector while increasing the spacing between reinforcement decreased the shear capacity of the connector.

- Based on the experimental test results and the destructive evaluation of the specimen the major mechanisms contributing to the shear capacity of the FlexBeam connection were identified. These mechanisms include steel and concrete dowels placed in double shear. Shear force capacity factors specific to the FlexBeam connection were developed for both the steel and concrete dowels which relate the shear capacity of the connection to the steel yield and concrete compressive strength. Utilizing the shear force capacity factors a design equation specific to the FlexBeam connection was developed to approximate the shear capacity of the system. The equations accounts for changes in details including hole size and rebar size as well as material properties such as concrete compressive strength and yield strength of the reinforcement. The FlexBeam shear capacity equation was validated with the experimental results for a connector type not used in developing the shear force capacity factors. It should be noted that there are current limitations of the developed FlexBeam design equation which must be heeded by design engineers.
- Being that the FlexBeam system utilizes newly developed beam components construction methods for the fabrication and erection of the FlexBeam precast components needed to be established. The development of the construction methods for the FlexBeam system include establishing: the

procurement of WT sections, required no-load camber measurements for the WT section, formwork details and setup, precast segment fabrication sequence, short-term and long-term deflection calculations and construction limit state requirements checks.

4. NONDESTRUCTIVE EVALUATION TECHNIQUES FOR FULLY GROUTED POST TENSIONED BRIDGE SYSTEMS

4.1. Introduction

Post-tensioned concrete bridges represent a major component of the American bridge inventory and due to the benefits provided by this construction technique it is likely that many new post-tensioned concrete bridges will be built in the future to meet our infrastructure needs. Post-tensioning tendons are comprised of prestressing strand, ducts, anchorages, grout, and corrosion protection equipment. Current details for the construction of post-tensioning tendons do not facilitate the long term inspection of the various tendon components. Recent cases of unexpected corrosion of post-tensioning tendons have illustrated the importance of developing detailing changes that would allow for improved inspection and the integration of nondestructive evaluation (NDE)/ nondestructive testing (NDT) methods.

As part of this research effort a study was conducted to examine commonly used post-tensioned construction systems (Cast-in-Place on Falsework, AASHTO, Bulb-T, Spliced Girders, Segmental Box Girders, and Transverse Top Slab Post-Tensioning) and post-tensioned components (Anchorage, Ducts, Permanent Grout Caps, Prestressing Strand and Post-Tensioning Bars). In addition damage conditions observed in PT tendons of current post-tensioning systems were assessed to identify the location and extent of damage.

An extensive literature review of available NDE methods for post-tensioned tendons was also conducted. The literature review focused on NDE techniques that can be used to detect the following issues in post-tensioned bridge girder systems: (1) Grout Voids/Condition, (2) Strand/Anchorage Corrosion, (3) Remaining Prestress Force and (4) Strand Location. The following NDE techniques were evaluated for use in fully grouted PT systems: acoustic emission, electrically isolated tendons,

ground penetrating radar, half-cell potential, impact echo, infrared thermography, magnetic flux leakage, radiography, time domain reflectometry, ultrasonic testing and visual inspection.

Many of the NDE methods investigated during the literature review stage are not yet used in the United States to inspect PT bridges. Further testing and verification of these methods capabilities is required before integration of these technologies into future PT systems can be recommended. As part of this research effort a testing plan was developed for the validation of selected promising NDE technologies for integration into fully grouted PT systems.

4.2. Background

Inspection of civil engineering infrastructure plays an integral role in maintaining our nations aging transportation network. The use of non-destructive testing (NDT) methods as an evaluation tool for civil engineering structures has become more readily available due to enhanced technologies and commercially available systems. The application of NDT techniques can provide vital information in post-tensioned (PT) structural systems, where visual inspection is prohibited due to the lack of access to key components inherent in these designs.

The discovery of severely corroded tendons within fully grouted post-tensioned bridge systems, such as the Midbay Bridge (Corven Engineering, 2001; Beitelman, 2000), has sparked industry wide concern and led to a moratorium on PT construction in some states. In many cases damage to post-tensioned tendons is not evident from external visual inspection and if unaddressed can lead to costly repairs and in extreme cases failure of the system. The ability to identify damaged tendons in seemingly "healthy" post-tensioned bridge systems has increased

interest in effectively utilizing nondestructive testing techniques to detect early warning signs of tendon distress.

Currently there are no inspection requirements for the application of NDT techniques in post-tensioned construction. The application of specific NDT methods and the interval at which, if at all these techniques are used in post-tensioned bridges systems is currently at the discretion of the owner/inspectors. In order to effectively utilize NDT techniques in post-tensioned bridge inspection it is important to understand the currently available technologies and select the method that is best suited for the inspection need at hand.

4.2.1. Damage Detection Needs for Grouted Post-Tensioned Tendons

To identify NDT methods that can be applied for PT tendon inspection the damage detection needs of grouted PT tendons must first be determined. In the case of post-tensioned systems one of the major concerns is monitoring the condition of the prestressing strand, as this is the main force resisting component. Based on a review of current grouted PT infrastructure and related damage case studies three main damage detection needs have been identified to assist in monitoring strand condition. These three main needs include: (1) grout voids, (2) strand corrosion, and (3) strand location. In response to the inspection needs of PT tendons a variety of applicable NDT methods have been selected for investigation including; acoustic emission, electrically isolated tendons, ground penetrating radar, half-cell potential, impact echo, magnetic flux leakage, time domain reflectometry and ultrasonic testing.

4.2.1.1. Grout Voids

Grouting material is one of the main corrosion protection mechanisms for post-tensioned tendons. The main function of the grout in terms of corrosion protection is to provide a protective barrier preventing any harmful substance, such as water and chlorides, from coming into contact with the strand. Grout voids in PT ducts are generally formed during construction leaving the tendons susceptible to future corrosion. Poor-quality grout materials and poor grouting procedures have been cited as the main causes for void formation in PT bridges (Corven Engineering, 2001). In an attempt to reduce grouting related issues in post-tensioned systems the Florida DOT has developed a training manual for grouting of PT tendons (FDOT, 2002) and various other papers have addressed issues related to grouting of PT tendons (Pielstick, 2002) and how to effectively repair poorly grouted ducts (Im, Hurlebaus and Trejo, 2010).

Despite efforts to educate the industry in proper grouting techniques, grout voids can still occur during the construction phase and are present in existing structures. One of the main issues with grout voids is that they cannot be identified through visual inspection (they can be identified through the use of a borescope but this requires invasive drilling) during construction or throughout the lifespan of the structure due to lack of visual access inside the duct. Since the presence of grout voids at the anchorages or along the free length of the tendon can lead to corrosion and possible failure of the tendons the ability to detect grout voids through the use of NDT techniques can prove useful to many bridge owners. In addition to using borescopes for enhanced visual inspection inside of the duct systems many different NDT methods have been explored for use in grout void detection in post-tensioned tendons including: ground penetrating radar (Zhou, Wang & Zhang, 2012; Maierhofer et al., 2004), impact echo (Ohtsu and Watanabe, 2002), radiography

(Brown and St. Leger, 2003), time domain reflectometry (Li et al., 2005; Chajes et al., 2003), and ultrasonic testing (Krause et al., 2008).

4.2.1.2. Strand Corrosion (Corrosion Protection Systems)

Corrosion of the prestressing strands in post-tensioned systems is one of the main concerns of bridge owners due to the integral role of these components in the load carrying capacity of the system. Even with the presence of the corrosion protection systems, chloride induced water and other harmful substances have been known to infiltrate these protective layers and come in contact with the strand, leading to corrosion. Known cases of strand corrosion that have led to tendon failure were observed in number of bridges including the Niles Channel Bridge (Powers, 1999) and Midbay Bridge (Corven Engineering, 2001).

The ability for strand corrosion to occur with little to no visual warning signs and the identification of multiple bridges with significant strand corrosion has sparked industry wide concern about the durability of post-tensioned systems. The capability to detect strand corrosion or breeches in the corrosion protection system that can lead to corrosion onset through the use of NDT methods can provide vital information to the owners about the condition of their bridge increasing confidence in the durability of post-tensioned bridge systems. A variety of NDT methods have been explored for the identification of strand corrosion or breeches in the corrosion protection system in post-tensioned systems including; acoustic emission (Azizinamini and Gull 2012; Salamone et al. 2012; Cullington et al. 2001), electrically isolated tendons (Elsener and Buchler 2011; Elsener, 2008; Elsener 2004a), half-cell potential (Iyer, Sinha and Schokker 2005; Elsener et al., 2003), magnetic flux leakage (Azizinamini and Gull 2012; Elsener and Buchler, 2011), radiography (Pimentel et al. 2010; Mariscotti et al. 2008), time domain

reflectometry (Hunsperger et al. 2003; Liu et al. 2002) and ultrasonic testing (Beard, Lowe and Cawley 2003; Bartoli et al. 2009).

4.2.1.3. Strand Location

Although not used specifically for evaluating PT tendon condition, determining strand location in existing structures can be an important initial step in applying NDT methods and certain visual inspection techniques such as borescope. In the case of internal tendons the location of the duct system is obscured by the concrete cover. In order to identify the location of the duct system and subsequently the tendons various NDT methods have been investigated. The effectiveness of the NDT method applied for identifying the location of the strands can be affected by the type of duct system used, i.e. metal or plastic, therefore it is important to know the materials used in each particular bridge before selecting a method for use. A number NDT methods have been investigated for the identification of steel or plastic post-tensioned duct location including: ground penetrating radar (Cheilakou et al., 2012; Maierhofer, 2003), radiography (Pimentel et al., 2010), and ultrasonic imaging (Azizinamini and Gull, 2012).

4.3. Nondestructive Testing Techniques and Applications

The following section identifies nondestructive evaluation techniques that can be applied to detect damage in grouted post-tensioned systems. A summary of applications, limitations, current uses and author's recommendations for use of the method are provided. Select NDT methods that are either currently used in post-tensioned system inspection or were identified as methods that could be potentially integrated in to future PT construction are investigated in more detail.

4.3.1. Summary of Nondestructive Testing Methods

Readily available nondestructive testing methods applied to post-tensioned systems were investigated based on the most current published literature. The current applications, methodology, limitations and the author's recommendations were explored for the following methods: Acoustic Emission, Electrically Isolated Tendons, Ground Penetrating Radar, Half-Cell Potential, Impact Echo, Infrared Thermography, Magnetic Flux Leakage, Radiography, Time Domain Reflectometry, Ultrasonic Testing and Visual Inspection. Based on the information gathered from the literature review it was identified that the accuracy and applicability of many of the techniques are affected by the duct type (metal or plastic), duct location (internal or external), and the surrounding components (i.e. reinforcing bars) within the post-tensioned system. A summary of the NDT methods are presented in Table 33. Based on the review of the available literature, NDT methods that are either currently used in post-tensioned system inspection or were identified as methods that could be potentially integrated into future PT construction were selected and outlined in more detail in the following subsections.

Table 33: Summary of NDT Methods

Method	Application in PT Systems	Limitations	Current Uses in PT Bridge Inspections	Recommendations
Acoustic Emission	<ul style="list-style-type: none"> Mainly used for the detection of wire fracture occurrence through continuous monitoring 	<ul style="list-style-type: none"> Cannot detect existing damage Produces large amounts of data that can be difficult to interpret Fractures in grouted tendons are more difficult to detect than in ungrouted or partially grouted specimens 	<ul style="list-style-type: none"> Not used for monitoring of grouted tendons 	<ul style="list-style-type: none"> The ability to accurately detect a break in a fully grouted PT tendon has not been adequately demonstrated and therefore is not currently recommended for long term monitoring
Electrically Isolated Tendons	<ul style="list-style-type: none"> Detection of breaches in the corrosion protection system Provides enhanced levels of corrosion protection of the tendon Allows for quality control and long term monitoring 	<ul style="list-style-type: none"> Requires plastic duct and special isolation hardware for anchorages If electrical isolation is not achieved during construction future NDE monitoring cannot be performed 	<ul style="list-style-type: none"> Not used in the US PT systems Applications exist in Switzerland (required for most PT systems) and Italy for quality control and long term monitoring of the PT corrosion protection systems 	<ul style="list-style-type: none"> The method appears to be viable for detection of a breach in the corrosion protection system of the duct during service life This approach appears to be viable and should be investigated further for the US market

Table 33: Summary of NDT Methods

Method	Application in PT Systems	Limitations	Current Uses in PT Bridge Inspections	Recommendations
Ground Penetrating Radar	<ul style="list-style-type: none"> • External detection of metallic duct location • Potential use in detecting grout voids in plastic ducts • Potential use in external detection of plastic ducts 	<ul style="list-style-type: none"> • Difficult to identify duct/tendon in areas with high reinforcement congestion • Cannot inspect conditions within metal ducts • Accuracy is reduced with increase in embedment depth 	<ul style="list-style-type: none"> • Widely used to locate metal ducts during inspections 	<ul style="list-style-type: none"> • This method provides a well-established tool for location of metallic ducts and reinforcement • GPR has also shown promise for locating plastic ducts in laboratory testing • This method provides the possibility for identification of voids in plastic ducts. This approach should be investigated further
Half-Cell Potential	<ul style="list-style-type: none"> • Detection of regions of high potential, indicative of active corrosion of tendons. 	<ul style="list-style-type: none"> • Ineffective for plastic or steel duct tendon systems when applied externally due to the masking effect of the ducts 	<ul style="list-style-type: none"> • External applications not typically used for the inspection of PT tendons 	<ul style="list-style-type: none"> • Due to the shielding provided by the duct this method is not viable for external assessment of corrosion • Half-cell probes internally embedded into the tendons are commercially available and should be investigated as a viable method

Table 33: Summary of NDT Methods

Method	Application in PT Systems	Limitations	Current Uses in PT Bridge Inspections	Recommendations
Impact Echo	<ul style="list-style-type: none"> • Detection of Grout Voids • Strand Location 	<ul style="list-style-type: none"> • Difficult to use in areas with congested rebar • Not well suited for inspecting large areas unless automated systems are used 	<ul style="list-style-type: none"> • Not typically used for tendon inspection 	<ul style="list-style-type: none"> • This method has the potential to be used as a quality control tool to ensure proper grouting of the tendon in known problem areas and is currently best suited for metal ducts • It is not currently recommended as a tool for strand location
Infrared Thermography	<ul style="list-style-type: none"> • Grout Void Detection • Strand Location 	<ul style="list-style-type: none"> • Ineffective for steel duct systems • Depth and thickness measurements require experimental or numerical calibration data. 	<ul style="list-style-type: none"> • Not typically used for tendon inspection 	<ul style="list-style-type: none"> • Based on the current technology and lack of successful applications in PT systems this method is not currently viable for grout void or strand location assessment
Magnetic Flux Leakage	<ul style="list-style-type: none"> • Strand Corrosion • Wire Fracture 	<ul style="list-style-type: none"> • More difficult to use when the duct is embedded in concrete • Presence of rebar can affect the accuracy • Ducts can create a masking effect 	<ul style="list-style-type: none"> • Primarily used for external ducts • Field readings for internal ducts have been found to be less accurate 	<ul style="list-style-type: none"> • This method is viable for the assessment of external tendons • Due to the ability for this method to detect corrosion of the strand it should be further investigated for applicability to internal tendons

Table 33: Summary of NDT Methods

Method	Application in PT Systems	Limitations	Current Uses in PT Bridge Inspections	Recommendations
Radiography	<ul style="list-style-type: none"> • Strand Corrosion • Grout Voids • Strand Location 	<ul style="list-style-type: none"> • Requires access to both sides of the specimen • Gamma ray devices use radioactive materials • X-ray and Gamma ray require safety precautions during transmission 	<ul style="list-style-type: none"> • Not typically used for tendon inspection 	<ul style="list-style-type: none"> • May be suited for detection strand corrosion and grout voids. If verified, it would be suited for the inspection of tendon anchorage regions and strand couplers where complex geometries and multi-layer material interfaces present problems for other NDE methods • Portable high intensity X-ray machines have improved the efficiency and imaging capabilities of radiography

Table 33: Summary of NDT Methods

Method	Application in PT Systems	Limitations	Current Uses in PT Bridge Inspections	Recommendations
Time Domain Reflectometry	<ul style="list-style-type: none"> • Grout Voids • Strand Corrosion 	<ul style="list-style-type: none"> • Method is sensitive to the size of the defect • Best results are obtained with internal sensors which need to be integrated into the duct • Content in voids can affect the accuracy • Pulse generator required can be expensive • No commercially available system for PT inspection 	<ul style="list-style-type: none"> • Not typically used or currently installed in PT bridge systems 	<ul style="list-style-type: none"> • This method appears promising and should be investigated further for internal integration in PT systems • The ability to detect both corrosion and grout voids while providing information on the location of the defect should be verified • Ability to detect moisture levels in grout should be explored further

Table 33: Summary of NDT Methods

Method	Application in PT Systems	Limitations	Current Uses in PT Bridge Inspections	Recommendations
Ultrasonic Testing	<ul style="list-style-type: none"> • Strand Corrosion • Grout Voids • PT Tendon Location 	<ul style="list-style-type: none"> • Ends of PT tendons need to be accessible for GWT • Signal interpretation difficult for complex geometries 	<ul style="list-style-type: none"> • Not commonly used for tendon inspection • GWT has been used for condition assessment of steel strand and prestress monitoring • Ultrasonic imaging has been used for grout void detection in PT tendons 	<ul style="list-style-type: none"> • GWT is a viable method for identifying strand breaks • Phase modified SAFT is a reliable method for detecting grout voids in PT tendons, but methods cannot handle complex geometries such as the tendon anchorage regions • This approach appears to be viable and should be investigated further for the US market
Visual Inspection	<ul style="list-style-type: none"> • Strand Corrosion • Grout Voids 	<ul style="list-style-type: none"> • Access to the interior of the duct requires invasive drilling • Each access point to the tendon only allows for a small amount of the tendon to be inspected • Location of the tendon must be known 	<ul style="list-style-type: none"> • Currently one of the most typically used methods • Borescopes are widely used to inspect internal conditions of tendons 	<ul style="list-style-type: none"> • This method provides accurate information on the condition of the tendon. Due to the fact that this method requires invasive drilling and allows only a small portion of the tendon to be inspected it is best suited as a tool to verify localized damage identified by other methods

4.3.2. Electrically Isolated Tendons

4.3.2.1. Methodology and Application

Electrically isolated tendons (EIT) are an integrated technology that allows for quality control monitoring during construction as well as long term monitoring of the tendons. EIT systems can be specified for internal grouted tendons for various applications including protection against stray current, long term monitoring of the tendon and preventing fretting between the normal reinforcement and prestressing strand (Elsener and Buchler, 2011). EIT systems have been implemented in Switzerland and Italy in many post-tensioned bridges including the Piaceza Viaduct and Marchiazza Viaduct in Italy and P.S. du Milieu and the Wiesebrucke Basel & Glattal Viaduct in Switzerland.

EIT utilizes an enhanced tendon/anchorage system that electrically isolates the tendon from the non-prestressed reinforcement network, which allows for monitoring to take place as well as provides enhanced corrosion protection of the tendons. In order to achieve this isolation of the tendons from the normal rebar network a mechanically resistant isolation plate is placed between the steel anchor head with wedges that block the strand and the cast iron bearing plate (Della Vedova and Elsener, 2006). As part of the enhanced anchorage system an access box is also installed near the anchorage of the system to collect electrical terminals from the tendons and normal reinforcing as well as provide an access point for inspections. A schematic of a typical electrically isolated tendon anchorage can be found in Della Vedova and Elsener (2006).

For the application of long term monitoring the EIT system is intended to identify breaches in the corrosion protection system of the tendon throughout the service life of the structure by monitoring for the ingress of water into the corrosion protection system. Monitoring of the tendon is performed by analyzing AC

impedance measurements taken between the steel strand in the duct and the normal (non-prestressed) reinforcement network in the concrete. Therefore, the measuring system includes the grout within the duct, the duct itself (including any defects) and the concrete surrounding the duct (Elsener and Buchler, 2011). A portable LCR meter is connected to the strand and reinforcement network via the installed access box and ohmic resistance (R), capacitance (C), loss factor (D) measurements are taken and recorded. The measuring system and connections are schematically shown in Figure 64.

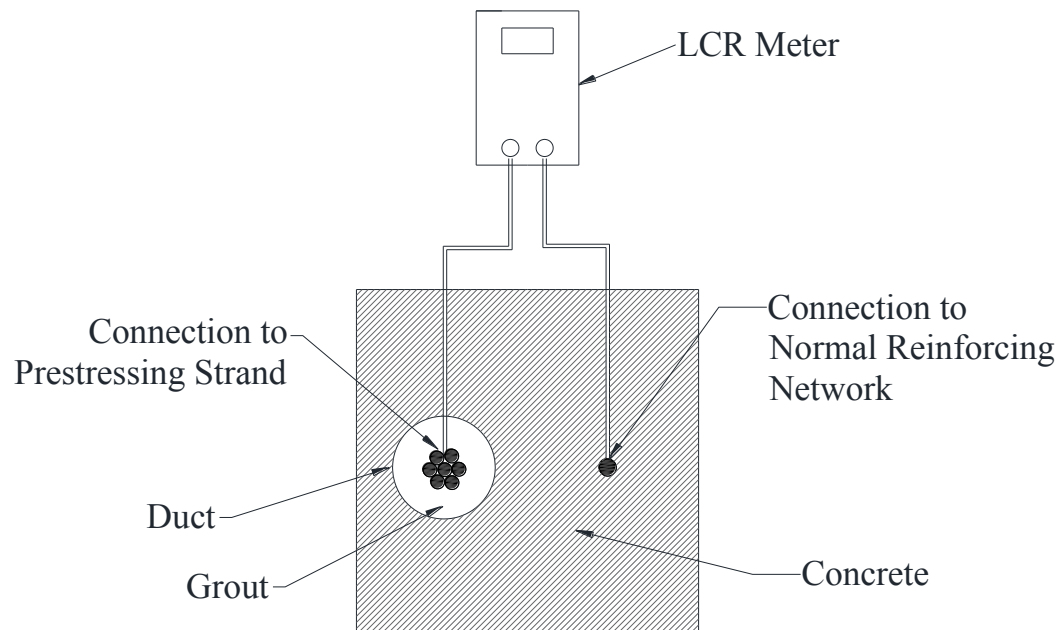


Figure 64: Electrically Isolated Tendon Measuring Principles Schematic

Implementation of the EIT system also provides many benefits outside of long term monitoring capabilities. The components utilized in the EIT system provide the highest level of protection for post-tensioned bridge system, referred to as protection level 3 (fib, 2005). The increased level of protection helps reduce the systems susceptibility to corrosion throughout the life span of the structure. The measurement principles and methods outlined for long term monitoring are also

applied during the construction process as a quality control tool. The measurements obtained during this stage can be used to assess the leak tightness of the system and identify any flaws in the tendons at an early stage. Currently, the EIT system is more widely used and established for quality control measurements in the field. For quality control, acceptance criteria for resistance measurements have been established and published in the Swiss guideline "Measures to Ensure Durability of Post-Tensioning Tendons in Structures" (ASTRA, 2007). The published acceptance criteria cover the various applications for which EIT can be specified; preventing fretting between the normal reinforcement and prestressing strand, use for the purpose of long term monitoring and for protection against stray current.

Unlike quality control monitoring for which threshold measurements values have been established for long term monitoring of the tendons resistance measurements are analyzed over time to provide indications of the condition of the corrosion protection system. Theoretically, the hydration of the grout and concrete surrounding the tendons will result in a continuous increase in electrical resistance with time. An increase in the moisture level of the grout or concrete will cause a decrease in the measured resistance, resulting in a deviation from the expected increasing trend line. A sequence of decreasing resistance measurements is indicative of water ingress into the corrosion protection system. Monitoring of the tendon throughout the lifespan of the structure can provide early warning that the corrosion protection system has been breached before detrimental corrosion has time to manifest.

The use of electrically isolated tendons for monitoring purposes have been tested in laboratory experiments (Elsener and Buchler, 2011; Elsener, 2008; Elsener 2004a) and implemented in a number of post-tensioned bridges in Switzerland and Italy (Elsener, 2008; Della Vedova and Elsener, 2006; Elsener 2004b; Della Vedova

and Evangelista, 2004a; Della Vedova, Elsener and Evangelista, 2004b) where data measurements have been collected and published. Electrical impedance measurements taken with EIT systems have been shown to be an efficient measure for quality control and the potential for long term monitoring along with enhanced tendon protection provides an additional benefit of implementing electrically isolated tendons in new construction. Although not used yet in the U.S. market this systems appears to be ready for field implementation, although further study of long term monitoring capabilities is recommended.

4.3.2.2. Method Limitations

Current limitations of the electrically isolated were also investigated. One limitation that arises with respect to NDT using electrically isolated tendons is that fact that this type of evaluation cannot be used on existing systems with conventional non-isolated tendon/anchorage detailing. When implementing electrically isolated tendon systems into new construction extreme care must be taken during the construction phase to insure that electrical isolation of the tendon is achieved. If a short circuit is present during construction then obtaining future measurements may not possible, making the monitoring system ineffective. Currently the acceptance criteria for the EIT system is strict but can be achieved if there is adequate planning and detailing in the design stage assuring there is room for the tendon between normal rebar, careful workmanship during the construction phase and the control over the ducts for leaks at joints, couplers, welding or defects is taken (Elsener, 2005).

Another limitation of the EIT system is that although it can potentially identify breeches in the corrosion protection system the method cannot currently identify the location of defect along length of the tendon. Being able to determine the location of the damage along the length of the tendon would be an area worth

investigating for improvement of the EIT system. The information gained by being able to determine defect location would make this a more complete monitoring system by allowing the area of damage to quickly be investigated with respect to durability and allow for repairs to be made. Some recent efforts have been made to determine if applying the magnetic flux method can be used as a complimentary monitoring technique with the EIT system (Elsener and Buchler, 2011) to identify the location of corrosion. It does not appear that MFL method for this application is currently viable for use in the field. It should also be noted that although EIT systems have been implemented in Europe there have been no known cases to date where damage has been identified based on the systems long term monitoring capabilities. This may be attributed to the fact that these systems have not been in place long enough (15-20 years) where corrosion of the tendons is expected, but this should continue to be investigated over time to establish the capability for long term monitoring.

4.3.3. Ground Penetrating Radar

4.3.3.1. Methodology and Applications

Ground penetrating radar (GPR) is an externally applied NDT technique that is typically used in PT systems to identify duct location, but has been investigated for applications of strand corrosion detection (Jones et al., 2010) and to assess grout conditions in plastic ducts (Zhou, Wang & Zhang, 2012). GPR is best suited for identifying the location of embedded metallic ducts and has more recently been studied for plastic duct applications (Cheilakou et al, 2012). GPR is an established NDT method with commercially available equipment.

The ground penetrating radar technique is based on the propagation of high frequency electromagnetic waves through a material. The wave propagation is affected by the presence of different material layers. When the waves encounter

material layers with different dielectric properties part of the wave is reflected back. Some examples of material layers with different dielectric properties within concrete systems which will cause a wave reflection include; reinforcing bars, metal or plastic ducts, voids in the concrete and the end of a specimen. Since the wave propagation velocity and the intensity of the pulse reflections are related to the dielectric properties of the material, the propagation time can be used to determine the depth at which the reflection occurred. Using these principles, the location of components such as metallic PT ducts embedded in concrete can be determined. It should be noted that metal interfaces produce a 100% reflection of the wave (Maierhofer, 2003) therefore identifying metallic ducts in areas with congested rebar or identifying grout voids within metallic ducts is not currently viable. Figure 65 shows the principle of GPR reflections in post tensioned systems with both metallic and plastic ducts.

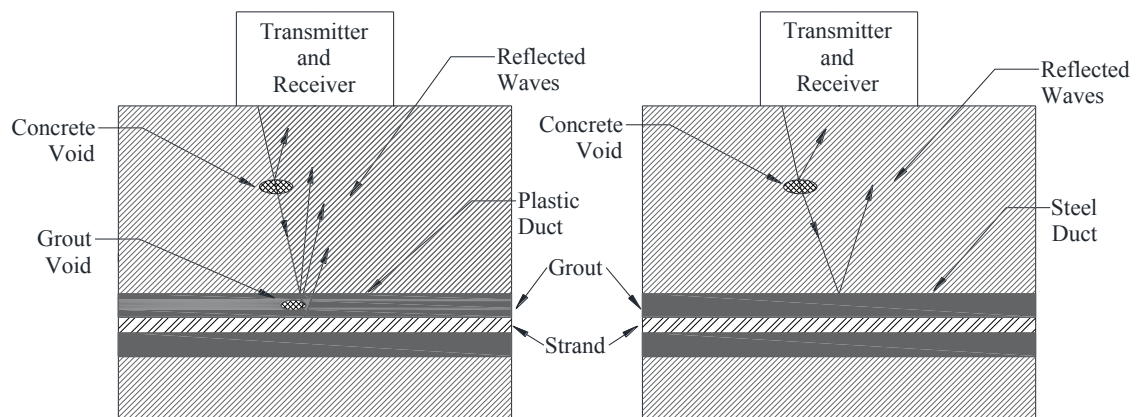


Figure 65: Schematic of GPR Process in PT Systems

The ability of the GPR method to determine the location of both tendon ducts and reinforcing bars has been validated in a number of different publications and has been applied successfully in the field (Bala, Garg and Jain, 2011; Kohl and Streicher, 2006; Gehrig, Morris and Bryant, 2004; Maierhofer et al., 2004; Maierhofer, 2003; Derobert, Aubagnac and Abraham, 2002). As mentioned previously GPR has been

investigated for other uses outside the common application of identifying embedded metallic features. Laboratory experiments have explored the capability of this method to locate embedded plastic ducts. A research effort by Cheilakou et al, 2012 which focused on the inspection of different concrete blocks with embedded steel reinforcement bars and plastic ducts, found that the location of the plastic ducts were detectable. GPR also has been explored for identifying grout condition and voids within plastic post-tensioned ducts in various research studies (Zhou, Wang and Zhang, 2012; Pollock et al, 2008; Maierhofer et al, 2004; Derobert, Aubagnac and Abraham, 2002) and found to shown promise for void detection. In addition, GPR has been investigated as a potential method to identify corrosion. Laboratory experiments were conducted (Jones et al, 2010) to investigate the ability of the GPR method to identify strand corrosion in prestressed beams and it was concluded that this method was not yet viable for detection of non-visible strand corrosion. Based on the currently available technology GPR appears currently viable for identifying embedded metallic components but further development is needed for other applications.

4.3.3.2. Limitations

One of the main issues affecting the accuracy and implementation of ground penetrating radar is the fact that metal interfaces produce a 100% reflection of the wave. This means that identifying duct location in areas with larger amounts of reinforcing (typically where bars are spaced less than 7 cm apart (Mairerhofer, 2003)) is not possible. An additional result of the complete reflection of the wave at metal interfaces is that this method cannot be used to inspect grout condition within metal ducts because it is physically infeasible to test inside a metal duct with the type of waves used in GPR (Derobert, Aubagnac and Abraham, 2002).

GPR scans can also be difficult to interpret and the estimation of depth of reflectors (bars or voids) depends on an assumed velocity of wave propagation (Ciolko and Tabatabai, 1999). The accuracy of the ground penetrating radar method is also currently limited by penetration depth, depth resolution and horizontal resolution. The effect of these parameters on the accuracy as presented by Maierhofer, 2003 is briefly summarized. Penetration depth depends on the damping of the electromagnetic waves, which is dependent on the absorption in the material, loss due to the effective angle of the antenna and loss due to scattering and reflection. Typically the depth of penetration decreases as the frequency of the antenna increases. The depth of resolution is affected by the duration of the electromagnetic impulses and therefore on the bandwidth of the antenna used. Antennas with higher frequencies result in increased depth resolution. The horizontal resolution, which is the distance between two adjacent reflections centers, depends on the damping of the electromagnetic waves in the material, the antenna aperture and the frequency (Maierhofer, 2003).

Ground penetrating radar is also affected by electric properties of the system being evaluated. The GPR method requires that the permittivity of the material be known. The permittivity of the materials, however, is influenced by outside parameters such as; material temperature, moisture content, salt content, pore structure and pulse frequency. Consequently, in order to have accurate results using GPR, calibration measurements of the material need to be taken, which in many cases may require taking core samples of the specimen

The application of ground penetrating radar as a method for detecting strand corrosion and grout condition within plastic tendon ducts still has many limitations. In the case of prestressing strand corrosion GPR was found to only be able to accurately detect heavy pitting and wire loss (Jones et al., 2010). This limits the

ability to detect corrosion at early stages and requires significant levels of corrosion to be present in the field. When investigating grout condition this method has not yet proven to be consistently accurate. Testing of GPR on plastic ducts with simulated voids has shown that voids in the tendon duct were detectable if the width (larger dimension) of the void was oriented facing the emitted microwaves, while voids with the thickness (smallest dimension) oriented facing the microwaves tended to be masked by the presence of the tendon (Pollock et al., 2008). In addition there is little published literature currently available on GPRs sensitivity to other grout conditions issues such as soft, non-setting and chalky grout or water intrusion. Further investigation and technological improvements to allow for increased sensitivity to corrosion levels and grout voids in plastic ducts should be explored for this method before it is recommended for use in the field for these applications.

4.3.4. Half Cell Potential

4.3.4.1. Methodology and Applications

Half-cell potential method is traditionally an externally applied NDT technique used to detect active corrosion of prestressing steel or normal reinforcing in concrete systems. For post-tensioned systems applications of externally applied half-cell techniques have been found to be ineffective for detecting corrosion of the strands due to the effect of both plastic and metallic ducts on the half-cell measurements (Iyer, Sinha and Schokker, 2005; Elsener et al, 2003). As an alternative, half-cell probes can be internally embedded into the duct system, thus avoiding many of the issues that arise with external application. Half-cell probes made for the specific application of internal embedment are currently commercially available.

The half-cell potential technique is a well-established method for corrosion evaluation of mild steel reinforcement in concrete structures and has been

standardized as ASTM C876: "Standard Test Method for Half-Cell Potentials of Uncoated Reinforcing Steel in Concrete." The evaluation of steel corrosion in concrete systems using the half-cell potential method is based on the measurement of voltage differentials between the external reference electrode (half-cell) and the embedded steel. ASTM C876 provides threshold values for uncoated reinforcing steel which relates voltage readings to probability of corrosion. According to Naito, Jones and Hodgson (2010) these half-cell potential values were established for normal reinforcement and are not definitive for prestressing steels, for large concrete covers, or for concrete with certain constituents. It is recommended for prestressing steel that a half-cell potential map of the specimen be developed and that corrosion activity be identified by looking at large relative changes in potential over the surface. An example of a half-cell potential map created for a prestressed beam can be found in Figure 66.

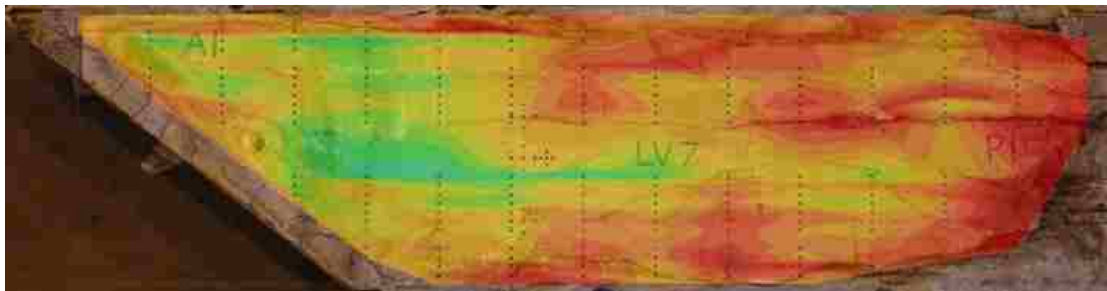


Figure 66: Half-cell potential map (Naito, Jones and Hodgson, 2010)

A typical half-cell potential system utilizes a reference electrode (externally applied or internally embedded) most commonly composed of copper rod in a copper sulfate solution (CSE), a silver rod in a silver chloride solution (SCE), or mercury/mercury chloride and a voltmeter. In order to take voltage readings a connection must be made between the voltmeter and the reinforcement and another between the electrode and the voltmeter (Figure 67).

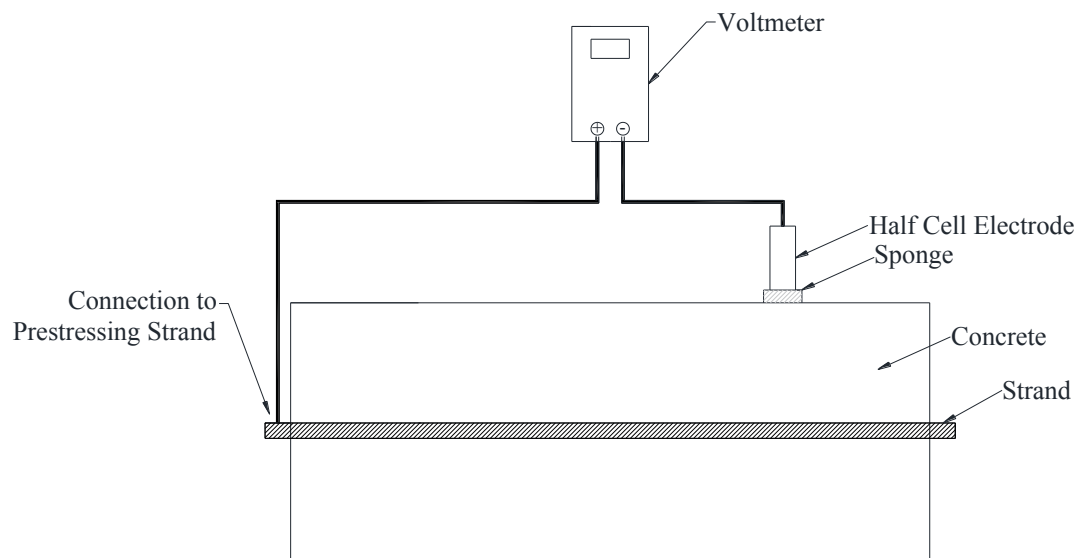


Figure 67: External Half-Cell Electrode Application

For external application of the electrode ASTM C876 provides a procedure for conducting test measurements. These test measurements can then be presented in one of two methods; equipotential contour map (Figure 66) which provide graphical delineation of areas where corrosion activity may be occurring or cumulative frequency distribution which provides an indication of the magnitude of the affected area within the concrete member.

Internal half-cell probes offer a potential solution to obtaining useful voltage differential measurements while avoiding the masking effect of the ducts observed with external applications. The probes can be embedded into the duct by attach the probes to the prestressing strand. One restriction compared to the external half-cell application is that using embedded probes provides only localized monitoring capabilities. It is recommended that the probes be placed at areas known to be prone to corrosion activity such as tendon high points and near the anchorage system. This localized monitoring can be used a complimentary method with other techniques such as EIT, which can detect damage but cannot identify damage

location. Validation of the use of the internal half-cell probes in PT ducts is needed before these systems should be put in place in future construction.

The use of the half-cell potential method with external reference electrodes has been investigated in many applications for corrosion detection in post-tensioned and prestressed applications (Mangual et al., 2012; Naito, Jones and Hodgson, 2010; Salas et al., 2004; DMJM Harris, 2003; Powers, Sagues and Virmani, 1999). Although internal half-cell probes that can be embedded within the duct system are commercially available there is currently a lack of available published literature validating the use in PT duct systems.

4.3.4.2. Limitations

There are many issues that arise when applying the half-cell potential method externally to post-tensioned systems. Half-cell potential is a powerful tool for the application of detecting corrosion in normal reinforcement, but in the case of PT strand it is only successful under very favorable conditions (Iyer, Schokker and Sinha, 2002). In a summary of available NDE methods for PT systems by Azizinamini and Gull (2012a), it is stated that this method is probably not applicable to internal or external PT ducts at this time and it is recommended that robust sensors and sensing systems that can be applied within the duct be developed.

The major limitation that affects the ability of this method to produce accurate results when the electrode is applied externally on the concrete surface is the presence of the duct systems utilized in grouted post-tensioned systems. Traditional half-cell measurements are based on the electrical and electrolytic continuity between rebar or PT strands in the concrete, reference electrode on the concrete surface and voltmeter (Elsener et al., 2003). In the case of metal ducts it was found that the duct shields the strands from the concrete surface and with plastic ducts this method cannot be used due to the fact that the plastic duct creates an

electrical barrier (Iyer, Sinha and Schokker, 2005; Elsnder et al., 2003). Additionally, when attempting to take measurements in specimens with metallic ducts these readings can be confused between corrosion of the strand, mild reinforcement, or duct depending on the electrical connectivity between these components (Iyer, Sinha and Schokker, 2005). On the other hand in a report by DMJM Harris (2003), in which half-cell testing was used to measure corrosion activity at the surface of PT tendons embedded in grout inside metallic ducts, concluded that this method can be used to measure corrosion activity. The application of this method to PT tendons with metallic ducts still needs to be further explored and verified, but it appears that there are many potential negative effects caused by the duct system.

Another limitation of this method for PT systems is that an electrical connection to the rebar or prestressing strand is required. This requires access to the prestressing strand or reinforcement which may not always be easily accessible in existing structures and may require invasive drilling. In addition, care must be taken when making the electrical connection during inspection. A bad electrical contact to the reinforcement from the voltmeter and between the individual bars/strand of reinforcement can cause errors in the measurements (Iyer, Sinha and Schokker, 2005). Also when applying this method the effect of outside factors such as moisture content of the specimen, which can have a significant effect on the voltage potential measurements and can vary by location along the same specimen and from inspection dates, must be understood.

4.3.5. Magnetic Flux Leakage

4.3.5.1. Methodology and Applications

Magnetic flux leakage is an established magnetic based external NDT method that is used to assess the condition of reinforcement in concrete structures. This method

can be used to detect location of reinforcing bars and for the detection of corrosion and loss of steel cross section in cables (Ciolko and Tabatabai, 1999). In post-tensioned systems this method can be applied to detect wire strand fracture and defects in the prestressing strand, such as thinning and pitting caused by corrosion, for both internal ducts and external ducts (Azizinamini and Gull, 2012). Magnetic flux leakage can be implemented using two different methods; the active and the residual method both of which can be applied to near surface tendons.

The magnetic flux leakage method is based on the principle that steel is a ferromagnetic material through which magnetic flux lines can develop. The steel components have a high magnetic permeability in comparison to the concrete or grout surrounding them. Therefore, when a magnetic field comes near the steel material in concrete, the magnetic flux lines pass through the steel bar or strand due to the fact that the steel offers a path of least resistance. When defects, typically induced by corrosion or fracture of the strand, are present the path through which the magnetic flux lines pass can become blocked causing the remaining steel to become magnetically saturated. As a result of this steel saturation, flux can be forced to flow through the air (Figure 68) and these changes in the components of the flux can be detected by sensors and analyzed to identify and locate defects.

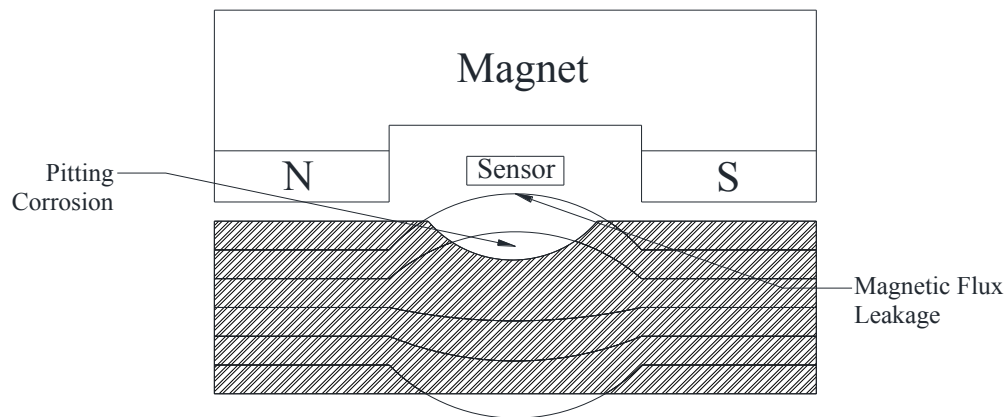


Figure 68: Magnetic flux leakage due to defect of the strand

The MFL devices can be made as hand held devices or beam-rider devices depending on the inspection needs of the system under investigation. As the magnetic flux leakage device is passed over the specimen under investigation relative magnetic field and travel time data is collected. Defects in the prestressing strands strand generally caused by corrosion result in erratic readings in the measured flux which can be detected by visually by graphing the relative magnetic field amplitude versus the traveled time or using data analysis software.

The magnetic flux leakage method has shown promise for its ability to detect corrosion and wire fracture of prestressing strands in both prestressed (Jones et al., 2010; DaSilva et al., 2009; Ghorbanpoor et al., 2000) and post-tensioned systems (Azizinamini and Gull, 2012; Mietz and Fisher, 2007; DMJM Harris, 2003). The use of magnetic flux leakage for post-tensioned systems has been performed in both laboratory and field applications and been investigated for both internal and external tendons. This method is currently most effectively applied to external tendons with plastic ducts systems, but with some improvements has the potential to be a useful tool for corrosion detection in internal tendons as well. Recent efforts (Elsener and Buchler, 2011) have been made to utilize MFL as a tool to locate defects in EIT systems by measuring the magnetic flux of the AC current to identify areas where the current is leaving the tendon indicative of areas of low resistance. This method has not been used for metal ducts and may not work well in this application due to shielding of the strands by the duct.

4.3.5.1. Limitations

One of the major limitations of the magnetic flux leakage method when applied to PT systems is that it is less effective for inspection of internal PT tendons due to the presence of other reinforcement and increased embedment depth. Currently MFL is only typically used in the field for inspection of external PT tendons. In field

evaluations the following challenges are encountered: the masking effect of the duct, disruption of the MFL signal due to the presence of additional layers of reinforcement and limited access to areas such as the anchorage zone (Azizinamini and Gull, 2012a). Another limitation of this method is that the anchorage region is difficult to inspect with MFL. In many cases the tendons at these locations can be embedded in thick layers of concrete making it difficult to achieve complete magnetic flux saturations without increasing the strength of the magnetics used. Additionally the trumpet regions present inspection issues due to high congestion of reinforcement steel (spiral and stirrups) and the end anchor plates which make the signal difficult to interpret (DMJM Harris, 2003). Finally, the results produced by this method can be difficult to interpret and may require some expertise in order to obtain accurate results (Azizinamini and Gull, 2012a).

4.3.6. Time Domain Reflectometry

4.3.6.1. Methodology and Applications

Time domain reflectometry (TDR) is a NDT technique that can be integrated or applied externally for post-tensioned tendon inspection. TDR is an electrical measurement technique that was originally established and widely used to determine the location and nature of defects in electrical transmission lines. An extension of this method has been applied to PT strands within ducts as a means to identify defects, corrosion of the strand (Hunsperger et al., 2003; Liu et al., 2002) and/or grout voids (Li et al., 2005; Chajes et al., 2003; Okanla et al., 1997), along the length of the duct.

The time domain reflectometry method involves sending high frequency electrical pulses through a transmission line and monitoring for partial pulse reflections caused by impedance discontinuities along the length of a cable. In the case that no defects are present the pulse will theoretically be absorbed at termination of the

cable therefore resulting in no partial pulse reflections. A typical TDR system for PT systems (Figure 69) consists of a transmission line, a pulse generator used to create the high frequency step pulse and an oscilloscope used to observe any partial pulse reflections. Handheld TDR meters are used for power transmission line inspection, however due to magnitude of the pulse required in PT system inspection separate pulse generator and oscilloscope components are utilized. The application of the TDR method for void detection and corrosion identification require a slightly different methodology regarding the application of the transmission line which will be briefly explained here but can be found in more detail in Chajes et al. (2003) and Liu et al. (2002). In general when using TDR for corrosion identification the steel prestressing strand along with an additional sensor wire is used to establish a two-conductor transmission line however when identifying grout voids a separate twin conductor transmission line (i.e. television cable or two-wire lamp chord) is integrated into the system. illustrates TDR integration into a duct system for grout void detection.

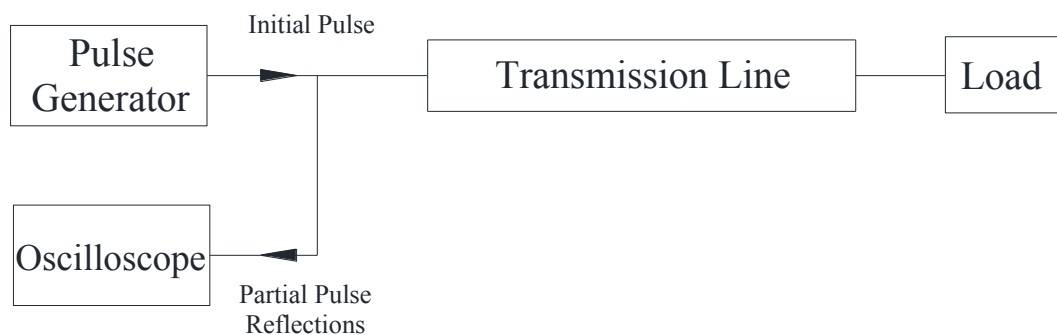


Figure 69: Block diagram for TDR application in PT systems (modified from Lui et al. 2002)

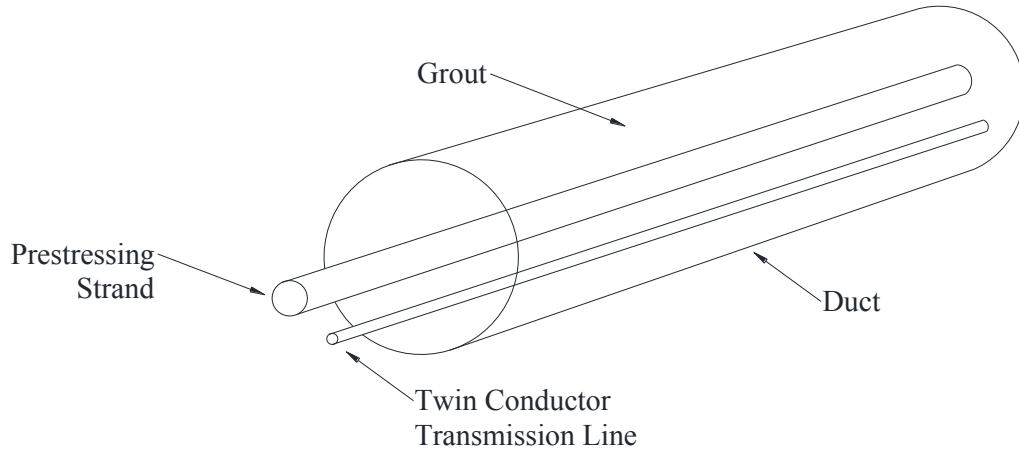


Figure 70: Time domain reflectometry application for grout void detection

When applying the time domain reflectometry method to post-tensioned ducts the presence of physical defects along the prestressing strand or in the grout surrounding the tendon will cause changes in the electromagnetic properties of the transmission line. These changes in electromagnetic properties can be detected by the TDR method resulting in the ability to identify locations of corrosion and grout voids along the ducts. Corrosion detection, particularly pitting corrosion, is based on the theory that the loss of cross sectional area of the strand causes a change in the localized impedance resulting in a pulse reflection at the location of pitting. The amplitude of the reflection wave can provide information on the severity of the damage to the strand. In the case of grout void detection the identification is based on the theory that the presence of a void in the grout will significantly change the dielectric constant of the medium through which the transmission line passes, affecting the characteristic impedance of the line. In general the change in the dielectric constant of the grout is due to the presence of air or water in the voids, both of which have different dielectric properties than the grout. When the transmission line is located near a void the change in impedance will generate a reflection in the signal wave which is then recorded as a signal bump by the

oscilloscope. In addition to identification of damage, TDR can be used to determine the location of damage by utilizing the transit time of the reflection wave.

For applications in post-tensioned concrete structures TDR has been used successfully in laboratory experiments to identify grout voids within ducts (Li et al. 2005; Chajes et al. 2003; Okanla et al.1997) and to identify strand corrosion along grouted tendons (Hunsperger et al. 2003; Liu et al. 2002). This method has been found to have the potential to not only identify damage but to also determine the location and relative size of a defect in the strand or grout (Liu et al. 2002). However, these studies have all been conducted on small scale specimens and have not been verified in full scale systems or field applications. In addition, the sensitivity of the method to proximity of defect and defect size needs to be better understood before field integration can be recommended.

4.3.6.2. Limitations

When utilizing time domain reflectometry one limitation that arises is the sensitivity of the defect to the proximity of the sensor wire. In the case of detecting strand corrosion the measurement sensitivity is related to the distance between the cable and sensor wire. The characteristic impedance depends on this distance, therefore the closer the two conductors the more sensitive the measurement will be (Liu et al. 2002). For the application of detecting grout voids the sensitivity is dependent on the location of the defect with respect to the transmission line. Voids far away from the strand/wire transmission line might be more difficult to detect because of their negligible effect on the line impedance (Chajes et al. 2003).

The sensitivity of the method to defect size is also a concern when using TDR. In the case of grout voids the reflection magnitude is related to void size, the larger the grout void the larger the reflection magnitude (Chajes et al. 2003).

Experimental results for strand corrosion identification have indicated the same

relationship between defect size and reflection magnitude; the magnitude of the reflection depends on the severity of the damage (Liu et al. 2002). This indicates that there is a lower limit to the size of defect that can be identified using this method, therefore small grout voids or surface corrosion may be difficult or impossible to detect.

Another limitation is that there is a lack of testing and verification of this method in field applications. The lack of field application may be due to the following issues summarized here and presented by Hunsperger et al. (2003) in more depth. Existing structures do not have detailing features designed for up to date TDR implementation. External detection cannot avoid the presence of concrete layers which cause strong attenuation to the signals, obstructing TDR measurements. Large pulse generators must be used in order to enhance the visibility of damage sites in the field. Further research is needed to find more practical sensor geometries of transmission lines that can meet the requirements of field practice (Hunsperger et al. 2003). Another concern with regards to field application is the implementation of the sensor wire for corrosion detection in the field. The wire should remain parallel to the strand for monitoring purposes but in many field applications the post-tensioning wire is draped at various locations along its length. This may make it difficult to receive consistent measurements along a strand.

Weather, temperature and moisture content also effects the readings obtained using this method, so these factors should be noted and taken into consideration during the inspection (Li et al. 2005). In addition the sensitivity of the measurements tends to decrease when external sensors are used (Liu et al. 2002). The accuracy and applicability of this method using internal or external sensors should be explored further and verified in the field or in testing mock up that more

similarly mimic field conditions, such as grouted tendons embedded in concrete with in the presence of a rebar network.

4.4. Experimental Testing Program for Promising Non-Destructive Testing Techniques

4.4.1. NDE Testing Recommendations

Of the many available Non-Destructive Evaluation (NDE) technologies that have been applied to monitor the condition of PT tendons, integrated technologies offer a distinct advantage over externally applied methods in that they can more readily provide data throughout the life span of the structure. Many of the traditional monitoring issues such as access and resolution, due to the high level of complexity of PT systems, are avoided by directly integrating NDE technologies into the construction details. Although the integration of NDE methods into PT systems shows great promise further research is needed to verify the capabilities of these systems when applied in long term monitoring applications. A proposed testing regime for two NDE methods; electrically isolated tendons and internal half-cell potential probes are proposed. The overall goal of the plan is to establish and verify the long term monitoring capabilities of these NDE technologies and to also establish that they can be used in parallel with each other to identify both the onset and the location of tendon corrosion. Establishing that these technologies can be successfully used in conjunction with each other is important as there is currently no commercially available stand-alone method that is capable of identifying the initiation of strand corrosion and the location at which the corrosion occurs.

It should be noted that these are not the only methods that can be applied to PT construction, but based on the current state of development of the technologies appear to be the most promising. As technologies advance other methods that did not seem appropriate at the time of this report may become applicable and provide effective ways of monitoring PT tendons over the lifespan of the structure. The NDE

field is constantly advancing and therefore owners should continue to explore new technologies based on their monitoring needs.

4.4.1.1. Electrically Isolated Tendons

As previously discussed, the electrically isolated tendon (EIT) system is an enhanced tendon/anchorage system that can be used in grouted post-tensioned systems. One of the main advantages of this post-tensioned system compared to traditional tendon/anchorage systems is that the EIT system provides enhanced corrosion protection of the tendons and allows for both quality control during construction and monitoring during the service life of the system. The EIT system has been implemented in a number of post-tensioned bridge systems in Switzerland and Italy. To date in most field applications EIT systems have been used primarily as a quality control tool during construction. The Swiss guideline "Measures to Ensure Durability of Post-Tensioning Tendons in Structures" (ASTRA, 2007) has established limiting resistance values as acceptance criteria for quality control applications.

One issue with the monitoring capabilities of the EIT system is that there is currently limited published data on the long term accuracy in detecting damage. Most of the work and effort has been focused on using the EIT measurements as a tool for quality control. For this reason it is recommended that the EIT system should be investigated for its ability to detect breaches in the corrosion protection system throughout the lifespan of a structure. Verifying that the EIT system can provide both quality control and long term identification of damage will increase the appeal of the system in the U.S. market. The system should be able to detect water ingress into the corrosion protection system over time. In addition the testing program should also establish guidance on when measurements should be taken in order to detect damage. This should include a study on the time duration between field

measurements and how weather related conditions can affect the impedance measurements.

Another limitation of the EIT system is that it cannot currently identify the location of the defect along length of the tendon. In order to provide a comprehensive monitoring system that can detect defects in the system and the location at which the damage occurs, EIT can be paired with a complementary NDE system. Some recent efforts have been made by Elsener and Buchler (2011) to pair EIT with the magnetic flux leakage method. Currently this application of magnetic flux leakage is not ready for effective field application. A proposed complimentary NDE method that should be explored is the utilization of commercially available internal half-cell probes.

4.4.1.2. Internal Half-Cell Potential

The half-cell potential method is a well-established and widely used method for external corrosion evaluation of mild steel reinforcing in concrete structures. This method has been standardized as ASTM C876: "Standard Test Method for Half-Cell Potentials of Uncoated Reinforcing Steel in Concrete." Although this method has proven successful for corrosion detection of standard reinforcing many issues can arise when applying this method to post tensioning tendons. The major limitation that affects the ability of this method to produce accurate results when used to detect corrosion of strands located within post-tensioning ducts is the duct system itself. Essentially the presence of the duct, whether it be plastic or metal, interferes with the traditional method of applying the half-cell method externally and does not allow for meaningful readings to be taken.

In order to overcome the shielding effect of the duct an internal half-cell probe system is recommended. To verify the effectiveness the use of half-cell probes should be investigated through experimental testing. Using internal half-cell probes

that can be attached directly to the tendon and placed inside the duct should theoretically eliminate the masking effect of the duct on the half-cell readings. This means that half-cell readings can be taken throughout the lifespan of the structure and used to identify active corrosion of the prestressing strand.

Internal half-cell probes are commercially available but are not currently used for the application of post-tensioning tendons. The ability to detect active corrosion while embedded in a grouted post-tensioning duct would need to be verified through an experimental testing program. As part of this experimental program the observed voltage differentials and corresponding corrosion levels should be compared to the threshold values provided in ASTM C876 to see if any modifications need to be made for the application of grouted tendons. Another important aspect of the internal half-cell probes monitoring capabilities that should be investigated is the area over which the probe can detect damage. In traditional applications of the half-cell method the probe is applied externally and moved along the length of the specimen providing measurements at each location. In the case of an embedded probe the readings can only be taken at the particular location at which it is installed. The range over which damage can be detected by a stationary half-cell probe thus becomes important. If the range is too small then there may be little to no cost benefit of implementing this technology. However if the range is deemed adequate enough to be used in known problem locations, such as tendons high points and the anchorage area then this NDE technology can provide useful localized long term monitoring and early damage detection information to owners.

Internal half-cell may be able to provide relatively low cost long term monitoring at set locations within the bridge system. Although this technology cannot be used as a standalone monitoring technique it will provide better damage assessment when paired with a more comprehensive monitoring technique that is able to assess

tendon condition over the entire length of the specimen. Internal half-cell probes can be used as a complementary technique to help identify the location of damage with a technique like EIT that may be able to detect damage but not identify the location along the length of the tendon.

4.4.2. Testing Methods

The proposed testing plan consists of two phases. The first phase is focused on verification of the capabilities of internally embedded half-cell probes to identify corrosion of a post-tensioning tendon. As part of this investigation a sensitivity study will be conducted to assess the required relative location of the probe to the corrosion site. Based on the results of the first phase of testing a decision on including half-cell probes in phase two testing plan can be made.

Phase two of testing is focused on assessing the ability of the EIT system to identify chloride laden water intrusion. Based on the success of the first phase half-cell probes may be integrated into the test specimen at the time of construction. The ability of the two NDE technologies to be utilized in conjunction with each other to identify a breach in the corrosion protection system and to locate the site of corrosion along the length of the strand will be investigated. The overall goal is to determine if these two technologies can be implemented in the field as a comprehensive monitoring system.

4.4.2.1. Phase 1 – Half-Cell Potential Testing

The goal of phase one testing is to demonstrate that current commercially available half-cell probes are capable of identifying voltage potential changes when strand corrosion is induced in fully grouted PT systems. As part of this effort voltage potential readings for the embedded half-cell probes should be compared to established threshold values that correlate the voltage potential readings with

corrosion. It is predicted that adjustments to the established ASTM threshold voltage potential values may be required for the application of internal half-cell in PT ducts. A sensitivity study should be conducted to investigate the range for which the internal half-cell can detect corrosion. The results of this study will establish a threshold relative location of the probe to the damage site in order for corrosion of the strand to be detected. The results of the small scale testing will determine if internal half-cell probes should be further explored in the full scale test specimen as a means for localized corrosion monitoring.

In order to verify the ability of internal half-cell probes for integration into PT systems an experimental testing program needs to be conducted. For preliminary testing small scale mock ups will be utilized (Figure 71). The mock ups will consist of a post-tensioning tendon cast into a grout block, approximately 5 feet (1.5 m) in length. The block will be made of grout as opposed to concrete so that the properties of the material surrounding the half-cell probe will be the same as those found in field applications. The half-cell probes will be attached to the tendon at known locations prior to grouting. Each test specimen will have half-cell probes attached along the tendon length. Installing multiple half-cell probes will provide both localized voltage potential readings and allow for average readings for the specimen as a whole.

It is intended that a minimum of three test specimens will be constructed. One specimen will be utilized as a control specimen. At least one other specimen will be used to verify the probes ability to identify corrosion and study the effect of the installation orientation of the probe on the tendon. The installation orientation refers to the location on the circumference of the tendon the probe is attached. In this specimen up to four half-cell probes will be placed around the circumference of the post tensioning strand, as shown in the "accuracy specimen" in Figure 71. At least

one additional specimen will be used to verify the damage identification ability of the probes as well as to study the effect of corrosion location to the probe in regards to tendon length. This specimen will have up to four half-cell probes placed at predetermined locations along the length on the tendon, as shown in the "sensitivity specimen" in Figure 71.

Once the small scale PT test specimens are constructed they will be monitored for 28 days before corrosion is induced. Corrosion of the strand can then be initiated and half-cell measurements taken in order to verify the ability of the internal probe to detect voltage differentials. Inducing corrosion of the strand can be done using two approaches. The first approach involves ponding chloride laden water on the specimen and allowing the water to naturally infiltrate the system. Over time this infiltration will result in corrosion of the strand. The second approach would be to apply established electrical methods to more rapidly induce corrosion of the tendons.

The locations at which corrosion will be induced along the length of the tendon will vary depending on the specimen. In the case of the control specimen no corrosion will be initiated until the testing of the other specimens is completed. The specimens in which probe location along the circumference of the tendon will be investigated can either have the entire specimen submerged in a chloride solution or have it ponded at the locations of the half-cell probes (shown in Figure 71). Corrosion of the strand will be allowed to naturally occur over time. In the specimens where the effect of corrosion location in respect to probe location along the length of the tendon is investigated corrosion will need to be induced at known locations along the tendon length (see Figure 71). To do this the chloride solution will only be applied at specific locations through either ponding or creating a defect in the grout that will more rapidly allow the solution to come into contact with the strand. By

only inducing corrosion at set locations the probes can be used to identify the difference in potential readings based on relative proximity to the corrosion site.

After initiating the corrosion process of the strand, voltage potential readings will be taken and monitored over time. In addition to taking the voltage potential readings with the internal half-cell probes, traditional external half-cell readings will also be taken along the length of the specimen. Readings of the external half-cell and internal probes will be taken at the same time for all specimens, including the time before which corrosion of the specimens is initiated. Multiple rewetting cycles of the specimen may be needed before corrosion can be detected using the half-cell probes. Once the half-cell potential readings have reached predetermined threshold values indicating corrosion and all testing is completed the strand will be removed from the specimens. Destructive evaluation will be used to correlate the actual strand corrosion with the half-cell probe readings.

One additional aspect of the internal half-cell that needs to be considered for field applications is how to route the wiring. For the testing program the cabling can be run through the specimen duct due to the short length. In the field the ducts can have significant lengths. This may present a practical issue with implementation that will need to be addressed during a full scale mock up testing.

4.4.2.2. Phase 1 Test Procedures

The goal of phase one testing is to assess the accuracy and sensitivity of half-cell potential probes in identifying strand corrosion. A minimum of three specimens illustrated in Figure 71 will be fabricated. The specimens will be fabricated for the same batch of grout. The grout used will be standard post-tensioning grout. Grade 270, ½ in. diameter, low relaxation seven wire strand, will be embedded into the grout. Potential variations of additional test specimens include: variation in grout type, strand diameter and cover of strands.

The specimens will be monitored for 28 days before inducing corrosion. The half-cell potential versus time will be plotted. Over the same time half-cell potential readings using external half-cell in accordance with ASTM will be taken and compared with the internal half-cell data. The specimen will then be subject to localized chloride exposure through ponding or other method to induce localized corrosion. The half-cell potential will be monitored daily through internal probes and external half-cell. When the internal probe readings exceed corrosion thresholds, the external half-cell readings will be taken for comparison and the test will be stopped. The specimen will then be destructively assessed to determine level of internal corrosion. The presence of corrosion should be verified relative to readings and the destructive evaluation. The duration of testing may need to be varied based on initial results.

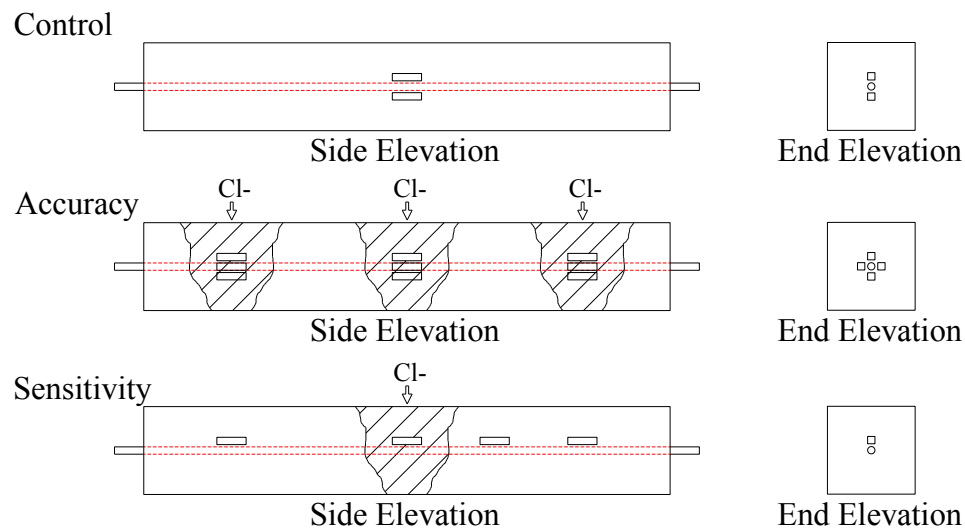


Figure 71: Half-cell testing layout

4.4.2.3. Phase 2 - Combined Assessment

The second phase of testing examines the performance of the EIT system and half-cell probes. The specimen will consist of an electrically isolated tendon system cast into a concrete block. External reinforcement will be included in the block to provide a connection for impedance readings between the two reinforcing networks. The

post-tensioning components used in the test specimen must be specially designed to provide the electrical isolation of the system. VSL produces a commercially available EIT system for which all required components can be obtained. It is envisioned that the specimens will be at least 30 feet in length to replicate the long spans of PT ducts that are typically found in the field. The duct and tendon will be run straight from anchorage to anchorage. As previously mentioned if phase one testing is successful then half-cell probes will also be included in this phase of testing. A minimum of three half-cell probes will be attached to each tendon and placed at predetermined locations along the length of the strand. The installation of the probes along the strand will be completed prior to grouting operations. The proposed test specimen can be seen in Figure 72.

A minimum of three specimens will be required in this phase of the testing program. One will act as a control specimen which will represent the no damage condition along the tendon length. The remaining specimens will have defects manually created after fabrication. The goal of intentionally creating defects is to study the effect of such a defect on the impedance measurements and to allow for chloride induced water intrusion into the duct system. Theoretically, the defect and water intrusion will result in a deviation in the upward trending resistivity measurements and provide an indication that there has been a breach in the corrosion protection system.

In order to verify the ability for the EIT system to identify breaches in the corrosion protection system defects must be created in the system. These defects can be created in a number of different ways. One option is to drill small holes into the specimen after fabrication creating a void space leading into the duct. This would allow for the chloride induced water to more rapidly infiltrate the corrosion protection system during testing. The ultimate goal of inducing damage is to allow

the chloride solution to infiltrate into the duct system at known locations, resulting over time in localized corrosion of the strand.

As previously mentioned one of the main objectives of this testing program is to establish that the EIT system can be used for long term monitoring of the tendons. After the test specimens have been fabricated impedance measurements will be taken and compared with established acceptance criteria threshold values (ASTRA, 2007). Regardless of whether the measured values exceed the acceptance criteria experimental testing will continue. It is expected that if defects are created in the specimen prior to fabrication that the specimens may not meet the established acceptance criteria. Daily measurements will then be taken in order to establish a sufficient increasing trend in the resistivity readings. Once the trend line has been established the sensitivity to defect size (breaching) and water intrusion can be examined. Defects in the system can be achieved by manually breaching the duct with a drill hole. The resistivity can be measured after each breach to identify sensitivity of resistivity to breach size. It may be necessary to fill the drill holes with mortar to complete the circuit on the breached system. Size and quantity of breaching can be examined by subsequently increasing the number and/or size of the damage induced. After the sensitivity to breaching in a standard system is examined the study can be repeated for the case where the concrete materials outside of the duct are saturated with chlorides at the breach locations. This will allow water to infiltrate the duct and over time initiate corrosion of the strand. The EIT system should be able to detect the water ingress through a deviation in the increasing trend line of resistivity.

It is recommended that the sensitivity of the EIT measurements to size of breach and water infiltration be established at one location before multiple locations of damage are introduced. For this testing program damage will first be introduced at

the midspan location. After the sensitivity study is completed for this location, damage may be introduced at additional sites (see Figure 72). It is not expected that damage be introduced at all locations indicated in Figure 72, but creating at least two to three damage sites is recommended as it has not been established that the EIT system can indicate if there are multiple damage sites based on the resistivity readings.

In the field EIT monitoring is not continuous, meaning readings are manually taken at intervals determined by the bridge owner. Currently there are no requirements for how often readings must be taken for long term monitoring applications. For this reason part of the experimental study will be focused on investigating how the resistivity measurements are effected by the time at which the reading is taken compared to the time at which wetting of the specimen occurred. Essentially the focus of this investigation is to determine if EIT can detect water ingress in a system where that water transmission has slowed due to atmospheric conditions. In addition to allowing chloride induced water to infiltrate at the defect site, the chloride solution will be ponded at locations along the test specimen where there is no defect in the duct and therefore no possibility of water infiltrating the duct system. Measurements will again be taken with the intention of determining if a rain event can initiate false positives. This will help develop guidance on taking measurements in relationship to weather related events such as rain or snow storms.

The EIT system is limited in that it can only detect that a water ingress into the duct has occurred but cannot provide the bridge owner with information on the location of the damage. This information is vital as further exploratory action cannot easily be performed without knowing an approximate location of the damage along the tendon length. For this reason the integration of internal half-cell probes along with

the EIT system will be investigated during this phase. The half-cell probes will be installed at strategic locations along the length of the tendon (see Figure 72). At minimum one of the probes will be located at a defect site to ensure that corrosion will initiate at a half-cell monitoring location. The other probes will be located at known distances from the damage site. The potential readings of the three probes will be evaluated individually and as an average. Half-cell measurements will be taken at the same time interval at which EIT measurements are taken.

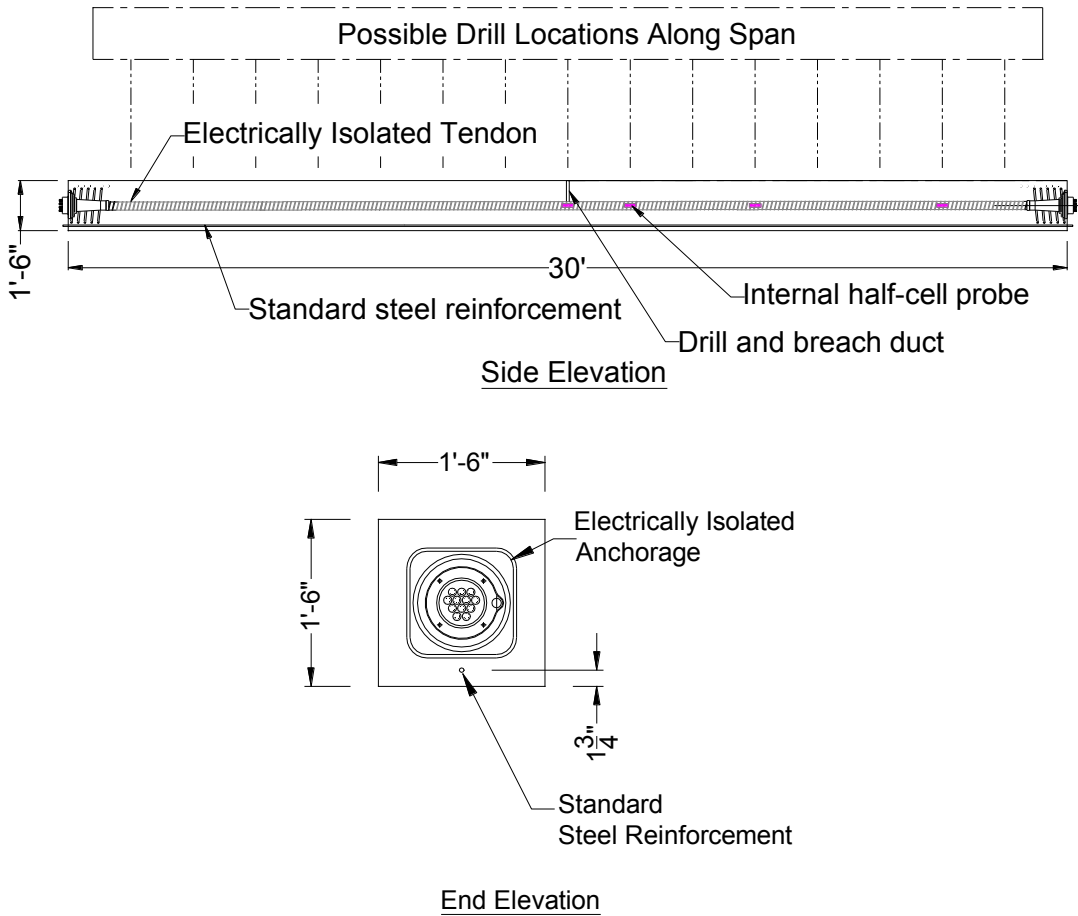


Figure 72: EIT test layout

4.4.2.4. Phase 2 Test Procedures

The goal of phase two testing is to assess the accuracy and sensitivity of the EIT method in identifying damage to the PT system, as well as to assess the potential

for the EIT and internal half-cell probes to be used together as a more comprehensive monitoring system. A minimum of three specimens illustrated in Figure 72 will be fabricated. All specimens will be fabricated from the same batch of concrete. The concrete will be normal weight concrete, type 1 cement with no supplementary cements. A minimum of 4000 psi compressive strength concrete will be required. Standard post-tensioning grout will be used in the PT tendons. Grade 270, ½ in. diameter, low relaxation seven wire strand and grade 60 ASTM A706 reinforcement will be used. Potential variations of additional test specimens include: variation in grout type, strand diameter and concrete type.

Each duct will be monitored for a minimum of 28 days or until an increasing trend line has been established. The resistance versus time graphs will be plotted. Internal half-cell potential measurements will be taken over the same time. The specimen will then be subjected to varying degrees of damage. A small diameter hole will be drilled into the duct. The impact on the resistivity will be evaluated. Continue drilling larger holes until a clear trend is observed. For damaged regions, introduce chloride intrusion and examine the impact of resistivity. For the undamaged region check the sensitivity to external moisture. Subject the specimen to additional damage locations and repeat the sensitivity study to defect size and chloride induced water ingress. The results should provide a summary of resistivity as a function of damage.

4.5. Future Work

The state of the art review of currently available nondestructive evaluation techniques has led to a better understand of monitoring options for fully grouted post-tensioned systems. From this review promising techniques were identified and a proposed testing plan to verify the monitoring capabilities of select NDE methods was developed. The next step would be to implement the testing plan developed for the electrically isolated tendon system and internal half-cell potential probes. The data generated during this experimental test program is critical in determining if these systems can effectively be implemented in the field for long term monitoring. Not only will the experimental program verify the systems damage detection capabilities but it will also provide insight on the sensitivity of the methods to tendon corrosion. In addition the combination of the EIT and internal half-cell method to be used as a comprehensive monitoring system will be studied. The ability to pair these two methods would provide bridge owners with a monitoring system that can both identify damage and the location at which the damage occurs. This would help ease owner concerns with utilizing post-tensioned construction in the future.

4.6. Conclusions and Contributions

This section summarizes the conclusions of this research effort and contributions made to the field of structural engineering. This research project involved identifying damage detection needs of fully grouted post-tensioned systems and investigating currently available nondestructive evaluation techniques that can be applied to detect grout voids, strand corrosion, strand location and determine remaining prestress in post-tensioning systems. Based on this investigation promising non-destructive evaluation techniques for use in fully grouted post-tensioned systems were identified. It was determined that NDE methods that can be integrated directly into the bridge system during construction and used for long term monitoring of the post-tensioning strand were the most applicable for the damage detection needs of the system. As a result the electrically isolated tendon system and internal half-cell probe monitoring system were selected for an experimental testing program. A proposed testing plan to validate and study the sensitivity of these NDE systems for long term monitoring of tendon condition was developed. As part of the testing plan the implementation of these two methods as complimentary methods for both identifying damage and the location at which it occurs is proposed.

Outlined below are the major contributions of this research effort:

- A state of the art review of non-destructive evaluation methods that can be applied to damage detection of post-tensioning tendons in fully grouted PT systems was conducted. NDT methods investigated in the state of the art review include those that can be used to detect: detect grout voids, identify strand corrosion, identify strand location and determine remaining prestress in post-tensioning systems. As part of this research effort an ATLSS report was published (Cercone et al. 2014) that summarizes the method detection

capabilities and limitations of the investigated NDE techniques as applied specifically to fully grouted PT systems based on the information provided in the published literature.

- As a result of the state of the art review of currently available NDT methods for damage detection of post-tensioning tendons in fully grouted PT systems it was determined that NDT methods which can be directly integrated in to future PT system construction show the most promise for long term monitoring of the post-tensioning tendons. Two NDE methods, the electrically isolated tendon system and internal half-cell probes, that can be directly integrated into the PT construction were selected as the most currently viable methods for this application. An experimental testing plan to validate the damage detection capabilities and perform sensitivity studies to the presence of damage for the electrically isolated tendon system and internally embedded half-cell probes was developed.

5. CONCLUSIONS

The work presented in this dissertation covered a breath of topics within the field of structural engineering including: site assessment procedures for structures subjected to tsunami generated debris, the development of an innovative composite bridge system and shear connection and non-destructive evaluation of fully grouted post-tensioned bridge systems. Collectively, the original research contributions in each of three topics resulted in improvements to this overall design process. The advancements to the design process include: assessment of demands on structural systems, developing new detailing of structural components, overall design changes to allow for improved inspection techniques and the development construction and fabrication methods for a prototype system. This section provides a summary of the collective contributions to the overall design process of structural systems.

The research conducted on tsunami generated debris has resulted in advancement in assessing load demands on structural systems. Before a structural system can be designed the demands on the system must first be quantified. Prior to this research effort there was little guidance available on applying impact loads for structural design in tsunami prone regions. The work performed in this study resulted in a debris characterization procedure that allows design engineers to classify debris into three main groups: small, moderate and large debris. The debris groupings are based on potential impact loads that can be generated by the debris item, which allows engineers to understand potential impact loads of uncommon debris types for which mass and stiffness characteristics are not provided by ASCE 7. The development of the debris impact hazard region allows design engineers to determine, based on the location of a structure, if design against impact of large debris is necessary. This design guidance is important as it would not be economically feasible to design all structures in tsunami prone regions to withstand the extreme levels of demand that can be generated by large debris items. Finally,

the improved approximations of the water velocity and inundation depth using the proposed extended energy grade line method are critical because these flow characteristics are utilized in computing the impact force demand applied to the structural system. Using the modified EGL method helps prevent design engineers from significantly under predicting these values compared to the results of the site-specific numerical model which is considered to be the most accurate of the available approximations.

The result of the research conducted on composite bridges systems is advancement in the detailing, connection design and construction of composite systems. Once the demands on a structural system are known the system must then be designed to withstand these loads. In the case of the newly developed FlexBeam system and shear connection the shear capacity of the connection was not known. In order to determine the capacity of the FlexBeam connection, experimental shear testing focused on assessing the contribution of key connection detail parameters to the overall shear capacity of the connector was conducted. The experimental data generated provided insight on how the connector detail parameters investigated affected the shear capacity of the connection and to understanding the mechanisms contributing to the overall shear capacity of the system. As a result of the experimental data and destructive evaluation of the test specimens a design equation was developed to approximate the capacity of a FlexBeam connection based on the connector details selected by the design engineer.

After a structural system is designed the next step is to fabricate and construct the system. Fabrication methods were established for precast FlexBeam components which are aimed at reducing cost and assuring critical dimensions of the system, such as embedment of the WT into the deck, are maintained for all precast components. Due to the fact that the WT section as well as the individually precast

composite segments can be unstable at long lengths, a laterally torsional buckling analysis of the sections was performed. AISC design equations can directly be applied to the WT section; however, for the composite section design equations are not available so as part of this effort the available AISC equations were modified based on concrete limit states for construction loading and applied to the individual FlexBeam components.

The research conducted on nondestructive evaluation techniques resulted in the identification of nondestructive evaluation methods that could be directly integrated into PT systems for long term monitoring. This study impacts the overall system design of post-tensioned bridges. After a structural system is constructed and put into use the system must be maintained throughout the lifespan of the structure. For many systems maintaining the structure involves identifying damage to the system over time. In the case of post-tensioned systems critical structural components such as the post-tensioning strands cannot visually be inspected and therefore require the application of nondestructive monitoring technologies to identify damage. Very few applications of NDE techniques for tendon condition assessment are typically used for field inspection of these system. As part of this research effort a state of the art review of available NDE techniques that can be applied to fully grouted post-tensioned systems was conducted. From this review of currently available technology, promising NDE methods for integration in PT systems were selected. The successful integration of these methods during construction will require some modifications to the way in which PT systems are detailed and designed in the future. In addition to identifying these promising methods a testing plan for two promising NDE methods, the electrically isolated tendon system and internal half-cell potential method, was developed. This testing plan has not yet been implemented but outlines the design of a test specimen and testing procedures that will be utilized to verify the long term monitoring capabilities

of the system as well as perform a sensitivity study on the level of damage which can be detected.

The research conducted on these three topics in structural engineering collectively resulted in the advancement of the current state of design practice. The overall design process includes consideration of many aspects of structural engineering from determining the design loads to be placed on a system, designing the overall system and detailing connections, to withstand the demand and developing fabrication and construction methods. The specific contributions to the field of structural engineering and the current state of design practice resulting from this research effort include advancements in assessing structural demands in tsunami prone regions, shear connection detailing and fabrication/erection for composite systems, and post-tensioning component detailing and overall system design to accommodate inspection techniques.

REFERENCES

AASHTO. (2012). "LRFD bridge design specifications." Washington, DC: American Association of State Highway and Transportation Officials.

AASHTO (2009). "Vessel collision design of highway bridges." American Association of State Highway and Transportation Officials, 217 pp.

Aghi, P.P., Naito, C., and Sause, R. (2015). "PA FlexBeam preliminary analysis." ATLSS Report No. 15-01, Lehigh University, Bethlehem, PA, January 2015.

Ahn, J.H., Lee, C.G., Won, J.H. & Kim S.H. (2010). "Shear resistance of the perfobond-rib shear connector depending on concrete strength and rib arrangement." Journal of Constructional Steel Research, 66(10), 1295-1307.

American Institute of Steel Construction (2005). "Manual of Steel Construction". 13th Edition. Chicago: AISC.

Armason, H., C. Petroff and H. Yeh (2009). "Tsunami bore impingement on a vertical column." Journal of Disaster Research, 4(6): 391-403.

Asakura, R., K. Iwase and T. Ikeya (2002). "The tsunami wave force acting on land structures." 28th International Conference on Coastal Engineering, Cardiff, Wales pp. 1191 -1202.

Asakura, R., K. Iwase, T. Ikeya, M. Takao, K. Kaneto, N. Fujii and M. Omori (2000). "An experimental study on wave force acting on on-shore structures due to overflowing tsunamis." Proc. of Coastal Engineering, 47: 911-915 (in Japanese).

ASCE (2010). "Minimum design loads for buildings and other structures."

American Society of Civil Engineers, 608 pp.

ASCE (2016). "Minimum design loads for buildings and other structures."

American Society of Civil Engineers, Chapter 6: Tsunami Loads and Effects (in preparation to be published in 2016).

ASTRA (2007). "Swiss guideline measures to ensure durability of post-tensioning tendons in structures." Available on www.astra.admin.ch.

ASTM A706 / A706M-14 (2014). "Standard specification for deformed and plain low-alloy steel bars for concrete reinforcement." ASTM International, West Conshohocken, PA, 2014, www.astm.org.

ASTM A992 / A992M-11 (2011). "Standard specification for structural steel shapes." ASTM International, West Conshohocken, PA, 2011, www.astm.org.

Azizinamini, A. and J. Gull (2012a). "FDOT protocol for condition assessment of steel strands in post-tensioned segmental concrete bridges: volume II." Florida Department of Transportation.

Azizinamini, A. and J. Gull (2012b). "Improved inspection techniques for steel prestressing/post-tensioning strand: volume I." Florida Department of Transportation.

Bala, D., R. Garg, et al. (2011). "Rebar detection using GPR: An emerging non-destructive QC approach." International Journal of Engineering Research and Applications, 1(4): 2111-2117.

Bartoli, I., S. Salamone, et al. (2009). "Health monitoring to detect failure of prestressing (PS) cables in segmental box-girder bridges." San Diego, CA, Department of Structural Engineering, University of California, San Diego. 09-0938.

Beard, M. D., M. J. S. Lowe, et al. (2003). "Ultrasonic guided waves for inspection of grouted tendons and bolts." *Journal of Materials in Civil Engineering*, **15**(3): 212-218.

Beitelman, T. (2000). "Tensile test results of post tensioning cables from the midbay bridge." Structures Research Center, Florida Department of Transportation.

Brown, K. and J. St Leger (2003). "Use of the Megascan imaging process in inspection systems for post-tensioned bridges and other major structures." *Proc. NDT-CE 2003*.

Candido-Martiins, J.P.S., Costa-Neves, L.F., & da S. Vellasco, P.C.G. (2010). "Experimental evaluation of the structural response of Perfobond shear connectors." *Engineering Structures*, 32, 1976-1985.

Carden, L., Chock, G., Yu, G., and Robertson, I. (2015). "The new ASCE tsunami design standard applied to mitigate Tohoku Tsunami building structural failure mechanisms." *Handbook of Coastal Disaster Mitigation for Engineers and Planners*, Butterworth, Heinemann, 461-490.

Cercone, C., Naito, C., Corven, J., Pessiki, S., Keller, W. & Pakzad, S. (2014). "Design and Detailing Post Tensioned Bridges to Accommodate Non-Destructive Evaluation: Subtask 11.1 Literature Review." Bethlehem, PA: ATLSS Report No. 14-01.

Chajes, M., R. Hunsperger, et al. (2003). "Time domain reflectometry for void detection in grouted posttensioned bridges." Transportation Research Record: Journal of the Transportation Research Board, 1845(1): 148-152.

Cheilakou, E., P. Theodorakeas, et al. (2012). "Application of Ground Penetrating Radar (GPR) as a Diagnostic Technique in Concrete Bridges Inspection." http://www.ndt.net/article/defektoskopie2012/papers/107_p.pdf.

Ciolko, A. T. and H. Tabatabai (1999). "Nondestructive methods for condition evaluation of prestressing steel strands in concrete bridges." Washington, D.C., NCHRP. NCHRP Web Document 23 (Project 10-53).

Corven Engineering (2001). "Mid Bay Bridge post-tensioning evaluation: final report." Florida Department of Transportation.

Cross, R.H. (1967). "Tsunami surge forces." Journal of Waterways and Harbors Division, ASCE 93(WW4):201-230.

Cullington, D., D. MacNeil, et al. (2001). "Continuous acoustic monitoring of grouted post-tensioned concrete bridges." NDT & E International, 34(2): 95-105.

DaSilva, M., S. Javidi, et al. (2009). "Nondestructive method to detect corrosion of steel elements in concrete." Final Report NDOR Research Project No. P597. National Bridge Research Organization (NBRO).

Della Vedova, M. and B. Elsener (2006). "Enhanced Durability, Quality Control and Monitoring of Electrically isolated tendons." Proc. 2nd International fib congress.

Della Vedova, M., B. Elsener, et al. (2004a). "Corrosion protection and monitoring of electrically isolated post-tensioning tendons." Proc. Third European Conference on Structural Control.

Della Vedova, M., L. Evangelista. (2004b). "Protection against corrosion and monitoring of posttensioned tendons in prestressed concrete railway bridges in Italy." First Workshop of COST 534: NDT assessment and new systems in prestressed concrete structures.

Dérobot, X., C. Aubagnac, et al. (2002). "Comparison of NDT techniques on a post-tensioned beam before its autopsy." NDT & E International, 35(8): 541-548.

DMJM Harris. (2003). "Test and assessment of NDT methods for post-tensioning systems in segmental balanced cantilever concrete bridges." Tallahassee, FL, Florida Department of Transportation. 03-0215.

EERI (2011). "Learning from Earthquakes – The March 11, 2011, Great East Japan (Tohoku) Earthquake and Tsunami." Societal Dimensions, Earthquake Engineering Research Institute, 15 pp.

Elsener, B. and Buchler, M. (2011). "Quality control and monitoring of electrically isolated post-tensioning tendons in bridges." Swiss Association of Road and Transportation Experts (VSS).

Elsener, B. (2008). "Monitoring of electrically isolated post-tensioning tendons." Tailor Made Concrete Structures–Walraven & Stoelhorst, Taylor & Francis Group, London, 231-236.

Elsener, B. (2004a). "Electrical isolation as enhanced protection for posttensioning tendons in concrete structures (PL3)." First Workshop of COST 534: NDT assessment and new systems in prestressed concrete structures.

Elsener, B. (2004b). "Experience with electrically isolated tendons in Switzerland." First Workshop of COST 534: NDT assessment and new systems in prestressed concrete structures.

Elsener, B., C. Andrade, et al. (2003). "Half-cell potential measurements— Potential mapping on reinforced concrete structures." *Materials and Structures*, 36(7): 461-471.

ESRI (2015). "ArcGIS." <http://www.arcgis.com/features/>. (March 30, 2015).

FEMA (2012). "Guidelines for design of structures for vertical evacuation from tsunamis." Second edition, Federal Emergency Management Agency, 194 pp.

Fritz, H.M., J.C. Borrero, C.E. Synolakis and J. Yoo (2006). "2004 Indian Ocean tsunami flow velocity measurements from survivor video." *Geophysical Research Letters*, 33(24), L24605.

Fujima, K., F. Achmad, Y. Shigihara and N. Mizutani (2009). "Estimation of tsunami force acting on rectangular structures." *Journal of Disaster Research* 4(6): 404-409.

Gehrig, M. D., Morris, Derek. V., Bryant, John. T. (2004). "Ground Penetrating Radar for Concrete Evaluation Studies."
http://www.foundationperformance.org/pastpresentations/gehrig_paper_march2004.pdf

Ghorbanpoor, A., R. Borchelt, et al. (2000). "Magnetic-based NDE of prestressed and post-tensioned concrete members – The MFL system." Final Report No. FHWA-RD-00-026, Federal Highway Administration, Washington, DC.

Google (2015). "Google Earth." <http://www.google.com/earth/>. (March 30, 2015).

Haraguchi, T. (2012). "Inundation area maps" Retrieved August 24, 2012, from <http://www.jsagi-map.org/tsunami/tsunami.kmz>.

Hunsperger, R. G., J. Li, et al. (2003). "Detecting corrosion in existing structures using time domain reflectometry." Research Report DCT 154. Delaware Center for Transportation, Newark, Del.

Im, S. B., S. Hurlebaus, et al. (2010). "Inspection of Voids in External Tendons of Posttensioned Bridges." Transportation Research Record: Journal of the Transportation Research Board, 2172(1): 115-122.

Iyer, S. R., S. K. Sinha, et al. (2005). "Ultrasonic C-Scan imaging of post-tensioned concrete bridge structures for detection of corrosion and voids." Computer-Aided Civil and Infrastructure Engineering, 20(2): 79-94.

Jones, L., S. Pessiki, et al. (2010). "Inspection methods & techniques to determine non visible corrosion of prestressing strands in concrete bridge components task 2- Assessment of candidate NDT methods." Bethlehem, PA: ATLSS Report No. 09-09.

Klaiber, F. W., & Wipf, T. J. (2000). "An alternate shear connector for composite action." In Mid-Continent Transportation Symposium Proceedings, pp. 115-120.

Krause, M., B. Milmann, et al. (2008). "Ultrasonic imaging methods for investigation of post-tensioned concrete structures: a study of interfaces at artificial grouting faults and its verification." Journal of Nondestructive Evaluation 27(1): 67-82.

Kohl, C. and D. Streicher (2006). "Results of reconstructed and fused NDT-data measured in the laboratory and on-site at bridges." *Cement and Concrete Composites*, 28(4): 402-413.

Li, J., L. Akl, et al. (2005). "Time-Domain Reflectometry to detect voids in posttensioning ducts." *Transportation Research Record: Journal of the Transportation Research Board*, 11(1): 243-252.

Liu, W., R. G. Hunsperger, et al. (2002). "Corrosion detection of steel cables using time domain reflectometry." *Journal of Materials in Civil Engineering*, 14(3): 217-223.

Maierhofer, C., M. Krause, et al. (2004). "Complementary application of radar, impact-echo, and ultrasonics for testing concrete structures and metallic tendon ducts." *Transportation Research Record: Journal of the Transportation Research Board*, 1892(1): 170-177.

Maierhofer, C. (2003). "Nondestructive evaluation of concrete infrastructure with ground penetrating radar." *Journal of Materials in Civil Engineering*, 15(3): 287-297.

Mangual, J., M. ElBatanouny, et al. (2012). "Corrosion damage quantification of prestressing strands using acoustic emission." *Journal of Materials in Civil Engineering*, 1326-1334.

Mariscotti, M., F. Jalinoos, et al. (2008). "Gamma-Ray imaging for void and corrosion assessment." *Concrete international*, 31(11): 48-53.

MathWorks (2015). "MATLAB the language of technical computing."
<http://www.mathworks.com>. (March 30, 2015).

Mietz, J. and J. Fischer (2007). "Evaluation of NDT methods for detection of prestressing steel damage at post-tensioned concrete structures." *Materials and Corrosion*, 58(10): 789-794.

Naito, C., L. Jones, et al. (2010). "Inspection methods and techniques to determine nonvisible corrosion of prestressing strands in concrete bridge components task 3 - Forensic evaluation and rating methodology." Bethlehem, PA: Pennsylvania Department of Transportation.

Naito, C., D. Cox, Q.S.K. Yu and H. Brooker (2012). "Fuel storage container performance during the 2011 Tohoku Japan Tsunami." *Journal of Performance of Constructed Facilities*, pp. 373-380.

Naito, C., Cercone, C., Riggs, H.R., and Cox, D. (2014). "Procedure for site assessment of the potential for tsunami debris impact." *Journal of Waterway, Port, Coastal and Ocean Engineering*, 140(2): 223-232.

Naito, C., Riggs, H.R., Wei, Y. & Cercone, C. (accepted 2016). "Shipping Container Impact Assessment." *Journal of Waterway, Port, Coastal, and Ocean Engineering*.

NOAA (2015). "National centers for environmental information (NCEI)." <http://www.ncei.noaa.gov/>. (September 4, 2015).

OCADI (2009). "Technical standards and commentaries for port and harbor facilities in Japan T.O.C.A.D.I.o. Japan." 998 pp.

Oguejiofor, E. C., & Hosain, M. U. (1992). "Behaviour of perfobond rib shear connectors in composite beams: full-size tests." *Canadian Journal of Civil Engineering*, 19(2), 224-235.

Oguejiofor, E. C., & Hosain, M. U. (1993). "A parametric study of perfobond rib shear connectors." *Canadian Journal of Civil Engineering*, 21(4), 614-625.

Oguejiofor EC, Hosain MU. (1997). "Numerical analysis of push-out specimens with perfobond rib connectors." *Computers & Structures*, 62(4), 617-24.

Ohtsu, M. and T. Watanabe (2002). "Stack imaging of spectral amplitudes based on impact-echo for flaw detection." *NDT & E International*, 35(3): 189-196.

Okanla, E., P. Gaydecki, et al. (1997). "Detecting faults in posttensioning ducts by electrical time-domain reflectometry." *Journal of Structural Engineering*, 123(5): 567-574.

Paczkowski, K., H.R. Riggs, C.J. Naito and A. Lehmann (2012). "A one-dimensional model for impact forces resulting from high mass, low velocity debris." *Structural Engineering and Structural Mechanics*, 42(6): 831-847.

PennDOT. (2012). "Pennsylvania Department of Transportation Design Manual Part 4." Publication 15M.

Pielstick, B. (2002). "Grouting of segmental posttensioned bridges in America." *Transportation Research Record*, No. 1813, pp. 235-241.

Pimentel, M., J. Figueiras, et al. (2010). "Gamma-Ray inspection of post tensioning cables in a concrete bridge."

http://www.thasa.com/ANTECEDENTES/Edimburgo_2010.pdf.

Pollock, D. G., K. J. Dupuis, et al. (2008). "Detection of voids in prestressed concrete bridges using thermal imaging and ground-penetrating radar." *Research Report for Federal Highway Administration (FHWA) Project DTFH61-05-C-00008*.

Popovics, S. (1973). "A numerical approach to the complete stress-strain curve of concrete." *Cement and Concrete Research*, 3(5), 583-599.

Powers, R.(1999). "Corrosion Evaluation of Post-Tensioned Tendons on the Niles Channel Bridge." Florida Department of Transportation, Gainesville, FL.

Ramsden, J.E. (1996). "Forces on a vertical wall due to long waves, bores and dry bed surges." *Journal of Waterway, Port, Coastal and Ocean Engineering* 122(3): 134-141.

Ramsden, J.E. and F. Raichlen (1990). "Forces on a vertical wall incident bores." *Journal of Waterway, Port, Coastal and Ocean Engineering* 116(5): 592-613.

Riggs, H.R., Cox, D.T., Naito, C.J., Kobayashi, M.H., Piran Aghl, P., Ko, H.T.-S., Khowitar, E. (2013). "Water-driven debris impact forces on structures: experimental and theoretical program." *Proceedings of the ASME 2013 32nd International Conference on Ocean, Offshore Mechanics and Arctic Engineering, OMEA2013, June, 2013, Nantes, France.*

Riggs, H.R., Naito, C.J., Cercone, C., and Wei, Y. (2015). 'ASCE 7 structural load provisions for impact by tsunami-driven shipping containers." *Coastal structures and solutions to coastal disasters joint conference, Boston, MA, ASCE, 11pp.*

Roberts, W. S., & Heywood, R. J. (1995). "Development and testing of a new shear connector for steel concrete composite bridges". In *Transportation Research Board Conference Proceedings (No. 7).*

Robertson, I. N., K. Paczkowski, H.R. Riggs and A. Mohamed (2013). "Experimental investigation of tsunami bore forces on vertical walls". *Journal of Offshore Mechanics and Arctic Engineering* 135(2): 021601-1 – 8.

Salamone, S., M. J. Veletzos, et al. (2012). "Detection of initial yield and onset of failure in bonded posttensioned concrete beams." *Journal of Bridge Engineering*, 17(6): 966-974.

Salas, R. M., J. West, et al. (2004). "Conclusions, recommendations and design guidelines for corrosion protection of post-tensioned bridges." Report FHWA/TX-04/0-1405-9, Texas Department of Transportation, Texas, February, 2004.

Seidl, G., Viefhues, E., Berthelley, J., Mangerig, I., et al. (2009). "Preco-Beam - Prefabricated Enduring Composite Beams based on Innovative Shear Transmission." Report RFSR-CT-2006-00030, Research Programme of the Research Fund for Coal and Steel.

Shi, F., Kirby, J.T., Tehranirad, B., and Harris J.C. (2011). "FUNWAVE-TVD, documentation and users' manual." University of Delaware, Newark, DE.

Takahasi, S. (2011). Personal communication, Port and Airport Research Institute.

Titov, V.V and Gonzalez, F.I. (1997). "Implementation and testing of the method of splitting tsunami (MOST) model." NOAA Technical Memorandum ERL PMEL-112 (PB98-122773), NOAA/Pacific Marine Environmental Laboratory, Seattle, WA.

Titov, V.V. and Synolakis, C.E. (1998). "Numerical modeling of tidal wave runup." *Journal of Waterway, Port, Coastal and Ocean Engineering*, 124(4), 157-171.

Titov, V.V., Moore, C. W., Greenslade, D.J.M., Pattiaratchi, C., Badal, R., Synolakis, C.E., and Kanoglu, U. (2011). "A new tool for inundation modeling: community modeling interface for tsunamis (ComMIT)." *Pure and Applied Geophysics*, 168(11): 2121-2131.

- Ushijima Y., Hosaka T., Mitsuki K., Watanabe H., Tachibana Y., & Hiragi H. (2001). "An experimental study on shear characteristics of perfobond strip and its rational strength equations." Proceedings of the international symposium on connections between steel and concrete. Stuttgart: University of Stuttgart, 1066-75.
- Veldanda, M. R., & Hosain, M. U. (1992). "Behaviour of perfobond rib shear connectors: push-out tests." Canadian Journal of Civil Engineering, 19(1), 1-10.
- Verissimo, G.S. (2007). "Development of a shear connector plate gear for composite structures of steel and concrete and study their behavior." Ph.D. thesis. Universidade Federal de Minas Gerais Belo Horizonte. [In Portuguese].
- Zellner, W. 1987. "Recent designs of composite bridges and a new type of shear connectors." Proceedings of the ASCEAABSE Engineering Foundation Conference on Composite Construction, Henniker, N.H. pp. 240-252.
- Wei, Y. (2015). Personal communication, National Oceanic and Atmospheric Administration.
- Weibe, D.M. (2013). "Tsunami inundation: estimating damage and predicting flow properties." MS thesis, Oregon State University, Corvallis, Oregon, USA, 102 pp.
- Yeh, H. (2006). "Maximum fluid forces in the tsunami runup zone." Journal of Waterway, Port, Coastal and Ocean Engineering 132(6): 496-500.
- Yeh, H. (2007). "Design tsunami forces for onshore structures." Journal of Disaster Research 2(6):1-6.

Zhou, X., Z. Wang, et al. (2012). "Detection of Voids in Grouted Tendon Ducts of Post-Tensioned Concrete Structures using Three Different Methods." CICE Conference Proceedings.

VITA

Christina Cercone was born on November 3, 1987 in Westchester, New York to parents Patrick and Angie Cercone. Raised in Yonkers, New York, Christina received her high school education from The Ursuline School in 2005.

Education

Lehigh University, Bethlehem, P.A.
Ph.D. in Structural Engineering May 2016
Advisor: Professor Clay Naito, Ph.D., P.E, PCI Blast Committee Chair

Manhattan College, Riverdale, N.Y.
M.S. in Structural Engineering May 2011

Manhattan College, Riverdale, N.Y.
B.S. in Civil Engineering, *Summa Cum Laude* May 2009
Minor: Mathematics

Honors and Awards

P.C. Rossin Doctoral Fellow, *Lehigh University* 2013
Gibson Fellowship, *Lehigh University* 2011
Presidential Scholarship, *Manhattan College* 2005–2009
John F. Hoban Medal for Civil Engineering, *Manhattan College* 2009
SEaONY Scholarship, *Structural Engineers Association of New York* 2008
ACEC NY Scholarship, *ACEC* 2008
Tau Beta Pi, Engineering Honors Society 2008
Chi Epsilon, Civil Engineering Honors Society 2008
Dean's List, *Manhattan College* 2005–2009

Publications

Cercone, C., Naito, C. Sause, R. (2016). "PA FlexBeam Shear Strength Evaluation and Construction Methods." ATLSS Report No. 16-01, Lehigh University, Bethlehem, PA, February 2016.

Naito, C. Riggs, H.R., Wei, Y., Cercone, C. (Accepted 2016). "Shipping Container Impact Assessment for Tsunamis." *Journal of Waterway, Port, Coastal and Ocean Engineering*.

Cercone, C., Natio, C. Corven, J., Pessiki, S., Keller, W., Pakzad, S. (2015). "Design and Detailing Post-Tensioned Bridges to accommodate Non-Destructive Evaluation." ATLSS Report No. 14-01.

Riggs, H.R., Naito, C., Cercone, C. Wei, Y. (2015). "ASCE 7 Structural Load Provisions for Impact by Tsunami-Driven Shipping Containers." *2015 Coastal Structures & Solutions to Coastal Disasters Joint Conference*. ASCE COPRI. Boston, MA.

Naito, C. Cercone, C. Riggs, H.R., Cox, D. (2014). "Procedure for Site Assessment of the Potential for Tsunami Debris Impact." *Journal of Waterway, Port, Coastal and Ocean Engineering*, 140(2):223-232.

Cercone, C. & Naito, C. (2013). "Corrosion of Bridges: What You Need to Know About Corrosion of Reinforcement in Concrete Bridges." Pennsylvania Department of Transportation Local Technical Assistance Program- Moving Forward Newsletter Fall 2013.